Moisture transport in porous building materials

Document status and date:
Published: 01/01/1995

Document Version:
Publisher's PDF, also known as Version of Record (includes final page, issue and volume numbers)

Please check the document version of this publication:

• A submitted manuscript is the version of the article upon submission and before peer-review. There can be important differences between the submitted version and the official published version of record. People interested in the research are advised to contact the author for the final version of the publication, or visit the DOI to the publisher's website.
• The final author version and the galley proof are versions of the publication after peer review.
• The final published version features the final layout of the paper including the volume, issue and page numbers.

Link to publication

Download date: 17. Nov. 2023

Moisture transport in porous building materials

Moisture transport

in

porous building materials

Dit proefschrift is goedgekeurd door de promotoren:

prof.ir. J.A. Wisse
prof.dr.ir. K. Kopinga

en de copromotor:

dr.ir. M.H. de Wit

aan mijn ouders

CONTENTS

1 | INTRODUCTION

In the past decades durability of materials, service life of building constructions, and life-cycle costs have been important topics in building research. The durability of a material and/or construction may be regarded as its resistance against deterioration caused by attacks from its environment. This deterioration may exhibit itself in various forms, e.g., in the case of masonry by decolouring of the surface (visual damage), cracking, chipping, or desintegration of brick and/or mortar (visual and mechanical damage).

Based on a probabilistic approach, the durability may be predicted [BEK92]. If sufficient data are available, such a method will predict the decrease of condition with time (e.g., [CUR93]). Based on such predictions, service life and life-cycle costs can be determined and management decisions can be made with respect to maintenance, restoration or renovation. However, these predictions are based on existing materials and constructions. Therefore no prediction can be made for new types of materials and constructions or different environmental conditions (e.g., other climate, contaminated rain, and pollution).

Looking at the various deterioration mechanisms, however, it is clear that moisture plays a dominant role. It enters by, e.g., driving (contaminated) rain, condensation, run off from roof and facade and/or capillary rise of ground water. In addition water may enter by failure of water services and flooding. Water will transport contaminants such as soluble salts. If wet, the material can become susceptible to freezing damage. It may also act as a substrate for the growth of bacteria, fungi, or algae with possible physical and chemical damages, but also possible health risks. A large fraction of the absorbed water will leave a material again because of drying. While a material is drying salt crystallisation may occur at the surface, causing defacing (efflorescence), or just under the surface, where it may cause structural damages, e.g., delamination, surface chipping, or desintegration.

Often it is tried to determine durability by means of accelerated aging tests in the laboratory. In these tests cyclic conditions are applied in which a specific degradation mechanism is dominant, e.g., freeze-thaw test. However, it is not always possible to relate the accelerated

1

test to natural deterioration as found in outdoor-exposure; a material that performs well in the accelerated aging test may perform poorly in practice and vice versa. Often the exact degradation processes are not clear or not well understood. As a consequence, there are different aging tests which aim to test durability in relation to the same degradation mechanism, e.g., freeze-thaw tests: NEN 2872, DIN 52252, ASTM C67. Another problem is that the combination of two durable materials, e.g., brick and mortar combined to masonry, may perform poorly. This is caused by the interaction between these materials, i.e., moisture will migrate from brick to mortar and vice versa. In figure 1.1 a schematic diagram of possible approaches to durability research is given.
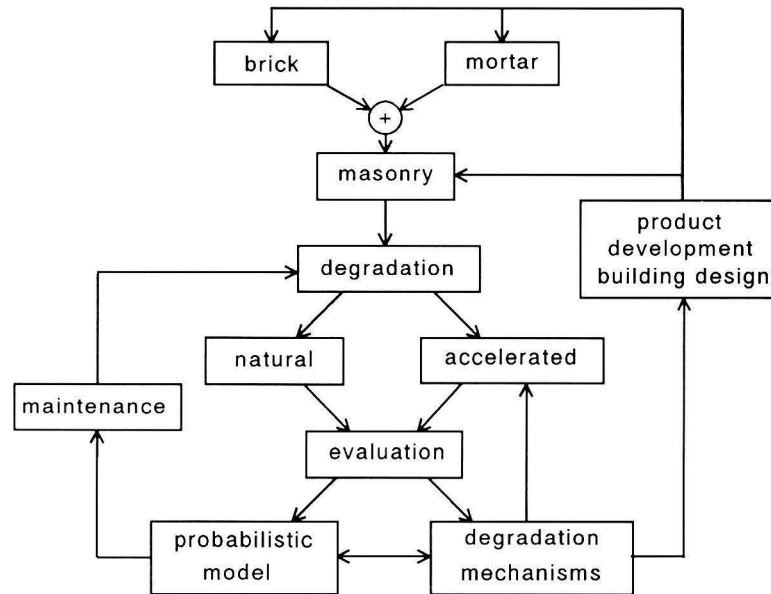

Figure 1.1: Schematic diagram of possible approaches to durability research of masonry

From the discussion above it may be clear that a good knowledge of the various degradation processes associated with durability cannot be obtained when the moisture transport is not sufficiently understood. Such a knowledge is needed to develop better accelerated tests. Apart

from this, it can give information for prevention and restoration. More insight into moisture transport may also give rise to adjusted technology and building design. Moreover, it can give information for the justification of probabilistic models.

The scope of this thesis is to study the moisture transport in porous building materials, as a first step towards understanding of the associated deterioration mechanisms. This study concentrates on isothermal moisture transport. Since in the Netherlands more than 90% of the exterior walls of dwellings consists of unplastered masonry, special attention is given to moisture transport in bricks, mortar, and their combination in masonry.

The moisture transport in saturated porous media was first described by Darcy [DAR56] in 1856. More or less complete studies concerning moisture transport in non-saturated porous media started after 1950. Among the classical studies are those of Philip and de Vries [PHI57, VRI58], Luikov [LUI66], and Berger and Pei [BER73]. Later Whitaker [WHI77] and Bear [BEA90] provided a more fundamental basis for the equations governing moisture and heat transport in porous media on basis of volume-averaging techniques. The objective of chapter 2 is to give a brief survey of the theory of isothermal moisture transport in porous media. The most relevant assumptions and limitations will be given, as well as the resulting diffusion model. In this model all mechanisms for transport are combined into a single moisture diffusivity, which is dependent on the actual moisture content.

For the present study, it was decided to determine the moisture diffusivity directly from moisture profiles as measured during various transport processes, i.e., drying and absorption. It has been shown that Nuclear Magnetic Resonance (NMR) and scanning neutron radiography offer powerful techniques to measure these moisture profiles in a non-destructive way [GUM79, GRO89]. Of these techniques NMR offers the best sensitivity, since it selectively probes the hydrogen atoms. However, complications occur if the materials under investigation contain large amounts of paramagnetic ions, as is the case for most building materials. Therefore an NMR apparatus was designed that was especifically suited to study the moisture transport in these types of material. In addition measurements were performed using neutron scanning radiography, in order to verify results found by NMR. Both instruments will be discussed in chapter 3.

Chapter 4 discusses the applications of, in particular, the NMR instrument for measuring the

moisture profiles during water absorption and drying of various building materials, i.e., soft mud machine moulded fired-clay brick, mortar, sand-lime brick, and gypsum plaster. Based on the measured profiles, the moisture diffusivity of the materials under investigation is determined as a function of the moisture content, both for water absorption and drying. A new method is presented to determine the moisture diffusivity for drying at low moisture contents, where the moisture transport is dominated by vapour transport.

In masonry brick and mortar are bonded, and these will therefore interact. The results of preliminary studies of the moisture transport across the brick/mortar interface are presented in chapter 5.

Finally, chapter 6 includes the main conclusions and suggestions for future research.

2 | MOISTURE TRANSPORT IN POROUS MEDIA

2.1 INTRODUCTION

A porous material consists of a solid-matrix and void-spaces, which are both interconnected. In principle, the equations for the various transport phenomena could be written at the microscopic level, i.e., the pore scale (fired-clay brick has a typical pore size of the order of 1 μm). The equations for the various transport phenomena can, however, generally not be solved on a microscopic level, since the geometry of the porous medium and the distribution of the phases is not observable and/or too complex to describe. Apart from this, a microscopic modeling of the moisture transport as such has hardly any practical relevance: a description of the moisture transport at a macroscopic level is needed. By volume averaging of the various transport equations at the microscopic level, the governing equations at the macroscopic level can be obtained. A full description of the volume averaging techniques is beyond the scope of this thesis and can be found in various references, e.g., [WHI77], [SLA81], and [BEA90]. The quantities derived at the macroscopic level are continuous and measurable. The macroscopic coefficients in the governing equations will be material coefficients, which are related to geometrical properties of the material (Note that these 'material coefficients' are also dependent on the physical properties of water).

In this chapter only the most relevant assumptions will be given, together with the diffusion model adopted for describing the isothermal moisture transport. This diffusion model is a mathematical description of the moisture transport on the macroscopic level, in which all mechanisms for mass transport are combined into a single moisture diffusivity which is dependent on the actual moisture content.

In order to define average quantities at the macroscopic level, a characteristic volume is needed. This volume has to contain so many pores that it will give statistically meaningful averages. Bear [BEA90] introduces the so-called Representative Elementary Volume

(REV). From a statistical approach he derives a lower limit for the characteristic length of a cubic REV for porosity (for fired-clay brick the lower limit is of the order of 0.05 mm for a maximum error of 2%). On the other hand, the REV for porosity should be smaller than the length scale corresponding to the macroscopic porosity gradient.
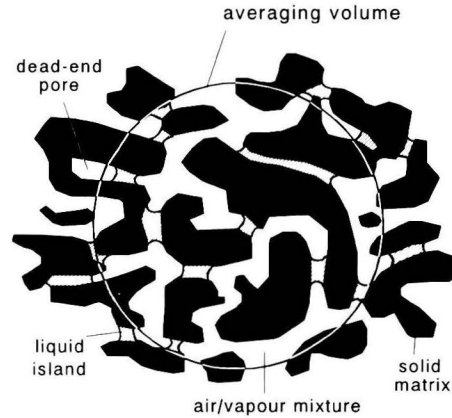
Figure 2.1 Schematic two dimensional representation of a non-saturated porous material. (Note that in this two dimensional representation only the void-spaces are interconnected)

If a REV can be identified, the porosity, n, of the porous medium is given by:

$$n = \frac{V_{r,m} + V_{r,d}}{V_r} \tag{2.1}$$

where $V_{r,m}$ is the volume of the multiple interconnected pores and $V_{r,d}$ is the volume of the dead-end pores within the volume V_r of the REV. (Isolated pores are not considered).

As the transport will predominantly take place via the interconnected pores, an effective porosity, n_{eff}, can be defined:

$$n_{eff} = \frac{V_{r,m}}{V_r} \tag{2.2}$$

For the discussion of the moisture transport in this chapter the assumption will be made that there are no dead-end pores present in the porous medium, i.e., $n = n_{eff}$.

6

With respect to moisture transport the following components can be identified:

- liquid water

- water vapour

- adsorbed water at pore walls, also called bound water

- air

The volumetric content, θ_α , of the component α is given by:

$$\theta_\alpha = \frac{V_{r,\alpha}}{V_r} \tag{2.3}$$

where $V_{r,\alpha}$ is the volume of the component α within the volume V_r of the REV.

Note that the volumetric vapour content, θ_v , represents the volume of liquid water present within a volume as vapour and

$$\sum_{(\alpha)} \theta_\alpha = n \tag{2.4}$$

2.2 SATURATED POROUS MEDIUM

For the transport in a porous medium saturated with liquid water ($\theta_l = n$) the following simplifying assumptions will be made:

(A1)   the solid matrix is rigid, macroscopically isotropic and homogeneous ($\nabla n = 0$), and inert.

(A2)   water is a Newtonian fluid (linear viscous fluid) and its mass density is constant.

(A3)   the flow is microscopically isochoric.

(A4)   the gravitational effect on the transport is negligible.

(A5)   the 'no-slip' condition at the water/solid matrix is valid.

(A6)   the friction force, due to momentum transfer at the solid-water interface, is much larger than both the inertial force of the water and its internal viscous friction due to flow.

The water transport on the microscopic level can be described by the Navier-Stokes equation. By volume averaging of the various quantities in this equation, taking into account

7

the interactions with the solid-matrix, the macroscopic volumetric flux of liquid water can be obtained:

$$\mathbf{q}_l = -\frac{k_l}{\mu_l}\nabla p \qquad (2.5)$$

In this equation k_l is the permeability, μ_l the dynamic viscosity of liquid water and p the macroscopic pressure. The permeability k_l is the only parameter related to parameters describing the microscopic geometrical configuration of the void space and has to be determined experimentally. Equation 2.5 is called Darcy's law and was first proposed on basis of experiments [DAR56].

2.3 NON-SATURATED POROUS MEDIUM

In addition to the assumptions made for a saturated medium, the following simplifying assumptions will be made for the description of the moisture transport in a non-saturated porous medium:

(A7)   There are two immiscible fluids present; a wetting fluid (water) and a non-wetting fluid (gas). This gas consist of a binary ideal gas mixture of water vapour and air.

(A8)   the water is pure, i.e., the influence of salts and other contaminants is negligible.

(A9)   a local thermodynamic equilibrium between water and vapour exists throughout the porous medium.

(A10) macroscopically the air is at atmospheric pressure throughout the porous medium or the pressure gradient can be neglected.

As a consequence of the interfacial tension a curved interface between a two immiscible fluids may give rise to a discontinuity in fluid pressure. The pressure difference between air and water is called the capillary pressure. Assuming a constant interfacial tension, $\gamma_{w,a}$, the capillary pressure at the microscopic level, p'_c, is given by the Laplace formula:

$$p'_c = -\gamma_{w,a}\left(\frac{1}{r'} + \frac{1}{r''}\right) \qquad (2.6)$$

where r' and r'' are the two principal radii of the curvature of the microscopic liquid

water/air surface. For most inorganic porous building materials the capillary pressure for water is negative, and hence water absorbs in these materials.

The macroscopic capillary pressure is the difference of the average pressures of air and water. Because the pores all have different dimensions and shapes, the water will distribute itself within the pores at each macroscopic pressure until an equilibrium condition is established. As a result the macroscopic capillary pressure is a function of the liquid water content:

$$p_c(\theta_l) = p_w - p_a \qquad (2.7)$$

where θ_l is the liquid water content, p_a the macroscopic pressure of the air, and p_w the macroscopic pressure of the water in the porous medium. The relation between the macroscopic capillary pressure and the moisture content is called the capillary pressure curve, retention curve, or sorption curve. This curve has to be determined experimentally. In figure 2.2 a schematic diagram of a capillary pressure curve is given.
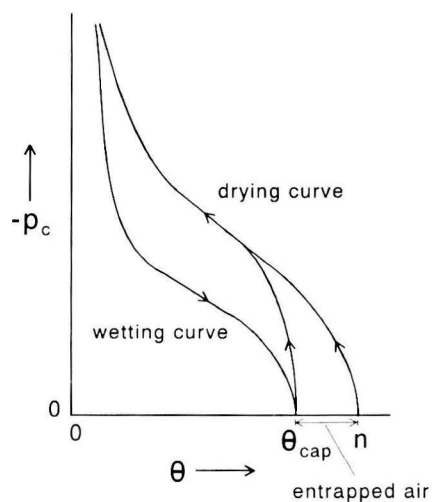
Figure 2.2 Schematic diagram of a capillary pressure curve for a porous material. (Only the main curves for drying and wetting are given. Each point on these curves represents an equilibrium situation with no liquid transport).

As can be seen from figure 2.2, the capillary pressure depends on the history of drying and wetting of the medium. This hysteresis in the capillary pressure curve is attributed to a number of causes. The three main effects are the so-called ink-bottle effect, the rain-drop effect and air entrapment. The ink-bottle effect results from the shape of the pores with changing wide and narrow passages. In such a non-uniform capillary there is a bi-stability of the interface. Wetting an initially dry or drying an initially wet capillary gives rise to two different stable configurations of the liquid (see Fig. 2.3a). These two configurations differ in moisture content. In a porous medium which contains a wide range of pores with different dimensions and shapes many stable configurations are possible, all contributing to the hysteresis. Another effect, the raindrop effect, represents the different contact-angle for an advancing and a receding water front at a solid-liquid interface, as is indicated by the shape of a raindrop (see Fig. 2.3b). This effect may be due to contamination of either the fluid or the surface, possible variability of the minerals that compose the surface, and surface roughness [ADA67].

wetting   drying   b) rain-drop effect
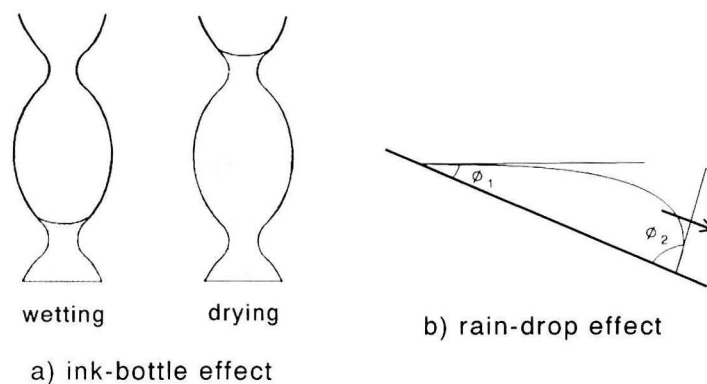
a) ink-bottle effect

Figure 2.3 Schematic representation of two effects contributing to hysteresis. a) The ink-bottle effect results from the non-uniform width of the pores. Wetting an initially dry or drying an initially wet capillary, gives rise to two different stable configurations. b) The raindrop effect represents the different contact-angle for an advancing and a receding water front at the solid-liquid interface.

A third effect is air entrapment in a porous medium after draining or rewetting (see Fig. 2.2). As a result the moisture content will only raise, under atmospheric conditions, to the so-called capillary moisture content, θ_{cap}. The entrapped air is generally assumed to be present in the dead-end pores, and hence $\theta_{cap} \approx n_{eff}$.

Analytic expressions are available to describe the effect of hysteresis in the capillary pressure curve. These are generally based on the so-called independent domain model, e.g., [MUA73, MUA74].

For the description of the moisture transport in this thesis the following assumption will be made:

(A11) the capillary pressure, $p_c(\theta_l)$, is a single-valued function.

As a consequence, each theoretical model will only describe either wetting or drying.

2.3.1 LIQUID TRANSPORT

In analogy to a saturated porous medium, the liquid water transport in a non-saturated medium can microscopically be described by the Navier-Stokes equation. In the volume averaging of the various quantities in this equation, extra liquid/air interfaces have to be taken into account. For the macroscopic volumetric flux of liquid water in the non-saturated case the following expression is found:

$$\mathbf{q}_l = -\frac{k_l(\theta_l)}{\mu_l} \nabla p_c(\theta_l) \tag{2.8}$$

where $k_l(\theta_l)$ is the effective permeability for liquid water, which is dependent on the moisture content and is related to parameters describing the microscopic geometrical configuration of the pores occupied by liquid water. Liquid water is now transported because of inhomogeneities in capillary action. Since the macroscopic air pressure gradient is neglected (assumption A10), the liquid transport by e.g., wind pressure is not taken into account.

Equation 2.8 can be rewritten as:

$$\mathbf{q}_1 = -K \nabla \Psi \qquad (2.9)$$

where

$$K = \frac{g \rho_1 k_1(\theta_1)}{\mu_1} \qquad (2.10)$$

is the hydraulic conductivity and

$$\Psi = \frac{p_c(\theta_1)}{g \rho_1} \qquad (2.11)$$

is the suction. In these equation g reflects the gravity and ρ_1 is the mass density of the liquid water.

Under isothermal conditions the suction only varies with the moisture content, and equation 2.9 can be rewritten as:

$$\mathbf{q}_1 = -D_{\theta,1} \nabla \theta_1 \qquad (2.12)$$

where

$$D_{\theta,1} = K \left(\frac{\partial \Psi}{\partial \theta_1} \right)_T \qquad (2.13)$$

is called the isothermal liquid diffusivity.

The macroscopic conservation of mass for liquid water expressed in volumetric quantities can be written as:

$$\frac{\partial \theta_1}{\partial t} = -\nabla . \mathbf{q}_1 - E_{1-v} \qquad (2.14)$$

where $E_{1 \to v}$ is the rate of evaporation.

Combining equation 2.12 and 2.14, the liquid moisture transport can be described by:

$$\frac{\partial \theta_1}{\partial t} = \nabla . \left(D_{\theta,1} \nabla \theta_1 \right) - E_{1-v} \qquad (2.15)$$

12

2.3.2 VAPOUR TRANSPORT

At the microscopic level the vapour transport under isothermal conditions is given by Fick's law:

$$\mathbf{q}_v = -\frac{1}{\rho_l} \frac{M}{RT} D_v \nabla p_v \qquad (2.16)$$

In this equation D_v is the diffusion coefficient of water vapour in air, M the molecular mass of water, R the gas constant, T the absolute temperature, and p_v the vapour pressure. The term M/RT results from the ideal gas law, whereas ρ_l results from the transformation of the mass flux for vapour into an equivalent volumetric liquid water flux.

By volume averaging of equation 2.16 the macroscopic volumetric flux through a porous medium with only air and vapour ($n = \theta_v + \theta_a$) is obtained [BEA87]:

$$\mathbf{q}_v = -\frac{n}{\rho_l} \frac{M}{RT} T^* D_v \nabla p_v \qquad (2.17)$$

where T^* is the tortuosity. The tortuosity is a tensor transferring the microscopic spatial derivatives into a macroscopic one. (Note that the porous medium is assumed to be isotropic (assumption A1) and hence the tortuosity in Eq. 2.17 is a scalar). In the case of vapour transport the tortuosity is often considered as accounting for the extra path length resulting from the tortuous pores.

In case of a non-saturated porous medium, the macroscopic vapour transport is given by:

$$\mathbf{q}_v = -\frac{(n-\theta_l)}{\rho_l} \frac{M}{RT} T^*(\theta_l) D_v \nabla p_v \qquad (2.18)$$

The tortuosity is now related to the void-space available for vapour diffusion ($\theta_v + \theta_a = n - \theta_l$) and is therefore a function of the liquid water content.

On the macroscopic scale the vapour pressure can be written as:

$$p_v = h p_{vs} \qquad (2.19)$$

where h is the relative humidity and p_{vs} the saturation pressure of water vapour above a

13

flat surface.

Above the curved liquid-vapour interfaces at the microscopic level the vapour pressure of water, p'_v, is different from the saturated vapour pressure, as given by Kelvin's equation:

$$p'_v = p_{vs} \exp\left(\frac{1}{\rho_l} \frac{M}{RT} \, p'_c \right) \tag{2.20}$$

Since p'_c is negative for water (see Eq. 2.6) the microscopic vapour pressure will decrease in the pores. In an analogous way, Edlefsen and Anderson [EDF43] have related the macroscopic capillary pressure to the decrease of the macroscopic vapour pressure:

$$p_v = h \, p_{vs} = p_{vs} \exp\left(\frac{Mg}{RT} \, \Psi \right) \tag{2.21}$$

This equation reveals that, under isothermal conditions, the relative humidity only varies with the suction and thereby with the moisture content θ_l. Therefore the gradient of the vapour pressure can be rewritten as:

$$\nabla p_v = p_{vs} \left(\frac{\partial h}{\partial \theta_l} \right)_T \nabla \theta_l \tag{2.22}$$

Combining equations 2.18, 2.21, 2.22, and using the ideal gas law, the vapour transport can be rewritten as:

$$\mathbf{q}_v = -D^F_{\theta,v} \nabla \theta_l \tag{2.23}$$

where

$$D^F_{\theta,v} = (n - \theta_l) \frac{Mg}{RT} \frac{\rho_v}{\rho_l} T^*(\theta_l) \, D_v \left(\frac{\partial \Psi}{\partial \theta_l} \right)_T \tag{2.24}$$

is the isothermal vapour diffusivity (by diffusion only).

In experiments it has been observed that the actual vapour flux is larger than that predicted by equation 2.23 and 2.24 on basis of Fick's law. Philip and de Vries [PHI57] developed a microscopic model to account for this enhancement. They suggested that in a porous material water islands will be formed due to capillary condensation. If over such an island a vapour gradient is present, vapour will condensate at one end of this island. At the same

time water has to evaporate at the other side to maintain equilibrium. The water will pass the island by a much faster mechanism: liquid transport. As a consequence, the diffusion coefficient will increase.
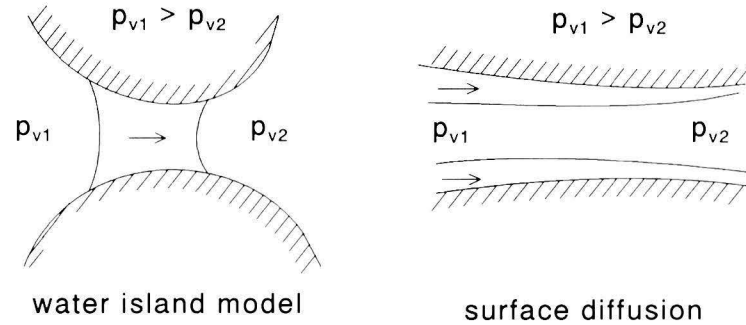
Figure 2.4 Schematic representation of two mechanisms for vapour diffusion enhancement. In the water island model, water vapour condensates at one end of a liquid island and at the same time water evaporates at the other side to maintain equilibrium. By surface diffusion water will be transported along the pore wall.

Other authors, e.g., [STA86] and [CHE89], take into account surface diffusion occurring in parallel to the vapour transport, which will act as an enhancement mechanism. By surface diffusion water adsorbed at the pore wall will be transported along the wall. Various mechanisms have been proposed, i.e., surface flow [ROW71] and surface hopping [OKA81]. In figure 2.4 a schematic representation is given of both mechanisms for vapour diffusion enhancement.

It is generally assumed that for both of these vapour enhancement mechanisms the contribution to the macroscopic vapour flux is in first order proportional to the gradient of the liquid water content. Hence the macroscopic vapour flux can be rewritten as:

$$q_v = -D_{\theta,v} \nabla \theta_l \qquad (2.25)$$

where

$$D_{\theta,v} = \left(1 + \alpha_{LI}(\theta_l) + \alpha_{SD}(\theta_l)\right) D_{\theta,v}^{F} \qquad (2.26)$$

In this equation $D_{\theta,v}$ is called the isothermal vapour diffusivity. α_{LI} and α_{SD} are correction factors for vapour diffusivity enhancement by liquid islands and surface diffusion, respectively.

The mass balance equation on the macroscopic scale for water vapour in volumetric quantities is given by:

$$\frac{\partial \theta_v}{\partial t} = -\nabla . \mathbf{q}_v - E_{v-l} \qquad (2.27)$$

where $E_{v \to l}$ is the rate of condensation $(E_{v \to l} = -E_{l \to v})$.

Combining equations 2.25 and 2.27 the vapour transport can be described by:

$$\frac{\partial \theta_v}{\partial t} = \nabla . \left(D_{\theta,v} \nabla \theta_l\right) - E_{v-l} \qquad (2.28)$$

2.3.3 MOISTURE TRANSPORT

Combining equations 2.15 and 2.28, describing the liquid and vapour transport respectively, the moisture transport can be written as:

$$\frac{\partial (\theta_v + \theta_l)}{\partial t} = \nabla . \left(D_\theta \nabla \theta_l\right) \qquad (2.29)$$

where

$$D_\theta = D_{\theta,v} + D_{\theta,l} \qquad (2.30)$$

is called the isothermal moisture diffusivity.

Assuming an equilibrium between water and vapour, the mass density of the vapour in the pores is given by:

$$\rho_v = \frac{\theta_v \rho_l}{n - \theta_l} \qquad (2.31)$$

16

Hence, the moisture content can be written as:

$$\theta = \theta_v + \theta_l = \left(\frac{\rho_v}{\rho_l}\right)n + \left(1 - \frac{\rho_v}{\rho_l}\right)\theta_l \qquad (2.32)$$

Since ρ_v is of the order of $10^{-5}\rho_l$, the right hand side of Eq. 2.32 is to a good approximation equal to θ_l for liquid water contents larger than 10^{-3}.

Hence, the moisture transport in a porous medium can be approximated by a non-linear diffusion equation:

$$\frac{\partial \theta}{\partial t} = \nabla \cdot \left(D_\theta \nabla \theta\right) \qquad (2.33)$$

2.4 BOUNDARY CONDITIONS

Two major boundary conditions can be identified: material/material and material/air.

Over a material/material boundary the macroscopic capillary pressure and hence the relative humidity (see Eq. 2.21) will be continuous:

$$\Psi_1 = \Psi_2 \quad \text{and} \quad h_1 = h_2 \qquad (2.34)$$

For each material the moisture content is a different function of the capillary pressure, so in general this condition will result in a jump of the moisture content at a boundary.

Under isothermal conditions the flux across the boundary material/air is given by:

$$\mathbf{q} \cdot \mathbf{n} = \frac{\beta}{\rho_l} p_{vs}(h_a - h_m) \qquad (2.35)$$

where n is the unit vector normal to the material/air interface, β the mass transfer coefficient, h_a the relative humidity of the air, and h_m the relative humidity of the material at the interface. The mass transfer coefficient is dependent on many parameters, such as air velocity, porosity, and surface roughness. In general, this coefficient has to be determined experimentally [ILL52].

17

2.5 SUMMARY

To a good approximation, the isothermal macroscopic moisture transport in porous media can be described by a non-linear diffusion equation (Eq. 2.33). In this diffusion model all mechanisms for moisture transport, i.e., liquid flow and vapour diffusion (with associated enhancement mechanisms) are combined into a single moisture diffusivity, which is dependent on the actual moisture content. Effects of gravity, air pressure differences, and hysteresis are not taken into account in this model. In the theory presented above no link is made between the microscopic structure (e.g., pore distribution) and the macroscopic coefficients. The diffusion model is, however, a very practical model since for each material only a single diffusion coefficient as a function of moisture content has to be known. This coefficient can be determined directly from transient moisture profiles, as will be discussed in chapter 4. In the following chapter methods to measure these profiles will be discussed.

3 | MOISTURE MEASUREMENT

3.1 INTRODUCTION

The moisture transport in porous media can be described by a non-linear diffusion equation, as was shown in the previous chapter. The diffusion coefficient is a function of the actual moisture content and has to be determined experimentally. By measuring transient moisture profiles during the various transport processes, i.e., drying and absorption, the diffusion coefficient can be determined directly, as will be shown in the next chapter. The classical way to obtain moisture profiles is the gravimetric method. The moisture profile is measured by first cutting the sample into slices. The moisture content of each slice is then determined by weighing the slices before and after drying at 105 ºC. Although this is the most direct method, it has two major disadvantages. First, it is a destructive method and therefore every profile has to be determined using different samples. The fact that one is not always able to exactly duplicate sample preparation and experimental history, obscures the interpretation of the data. Apart from this, the method is laborious and time consuming. Secondly, the method is not accurate in its spatial resolution. Slices which can be cut are of the order of 0.5 to 1 cm, depending on the type of material. The experimentally determined moisture content is the average over such a slice. Especially steep gradients, which occur, e.g., in the case of an advancing wetting front, cannot be accurately determined by this method.

An experimental method to measure transient moisture profiles should therefore preferably be non-destructive and give a high spatial resolution. Examples of these methods are gamma- or neutron attenuation [DAV63, CRA83, GRO93], and nuclear magnetic resonance [GUM79]. Of these methods nuclear magnetic resonance (NMR) offers the best sensitivity, as it selectively probes the hydrogen nuclei, unlike the attenuation methods. With NMR also a distinction can be made between free, physically bound, and chemically bound water. However, serious complications occur if the materials under investigation

contain large amounts of paramagnetic ions, as is the case for most common building materials, like brick and mortar [GUM79, FOR91]. The short transverse relaxation time, T_2, and the broad resonance linewidth of the hydrogen nuclei in these materials preclude the use of standard NMR techniques. Therefore the moisture transport was studied using an NMR apparatus, that was especially designed for these types of material. This apparatus will be discussed in section 3.2. Of the attenuation methods mentioned above, neutron scanning radiography offers the best sensitivity. This method was used to verify results obtained by NMR measurements and will be discussed in section 3.3.

3.2 NUCLEAR MAGNETIC RESONANCE

3.2.1 GENERAL CHARACTERISTICS

Almost all nuclei have a magnetic dipole moment, resulting from their spin-angular momentum. (One can think of a nucleus as a charged sphere spinning around its axis, which corresponds to a current loop, generating a magnetic moment). In a Nuclear Magnetic Resonance (NMR) experiment the magnetic moments of the nuclei are manipulated by suitably chosen electromagnetic radio frequency (RF) fields. NMR is a magnetic resonance technique, for which the resonance condition of the nuclei is given by:

$$f = \frac{\gamma}{2\pi} B_0 \qquad (3.1)$$

In this equation f is the frequency of the electromagnetic RF field, γ is gyromagnetic ratio (for ^{1}H $\gamma/2\pi$ = 42.58 MHz/T) and B_0 represents the externally applied static magnetic field. Because of this condition the method can be made sensitive to only hydrogen and therefore to water, in contrast to the attenuation methods [DIX82].

In a pulsed NMR experiment the orientation of the moments of the spins in a static magnetic field is manipulated by short electromagnetic pulses at the resonance frequency, bringing the system in an excited state. The amplitude of the resulting signal emitted by the nuclear spins, the so-called spin-echo signal [HAH50], is proportional to the number of nuclei taking part in the experiment. The spin-echo signal also gives information about the

rate at which this magnetic excitation of the spins decays. The system will return to its magnetic equilibrium by two mechanisms: interactions between the nuclei themselves, causing the so-called spin-spin relaxation, and interactions between the nuclei and their environment, causing the so-called spin-lattice relaxation.

Assuming that both mechanisms give rise to a single exponential relaxation and that spin-lattice relaxation is much slower then the spin-spin relaxation, the magnitude of the NMR spin-echo signal is given by:

$$S \propto \rho \, [1 - \exp(-TR/T_1)] \exp(-TE/T_2) \qquad (3.2)$$

In this expression ρ is the density of the hydrogen nuclei, T_1 the spin-lattice or longitudinal relaxation time, TR the repetition time of the spin-echo experiments, T_2 the spin-spin or transverse relaxation time, and TE the so-called spin-echo time.

Obviously small T_2 values lead to a decrease of the spin-echo signal, whereas, on the other hand, small T_1 values are preferred, as this parameter limits the repetition time (usually TR $\approx 4T_1$) and hence the rate at which the moisture profiles can be scanned. In porous materials T_2 will be decreased strongly with respect to that of 'pure' water, due to surface relaxation at the pore walls, which dominates at applied magnetic fields below 0.1 T, and due to diffusion of water in the field gradients resulting from the susceptibility mismatch between the pore fluid and the porous material, which dominates at higher fields [KLE90, KLE93]. Almost all studies on moisture transport in porous building materials up to now are limited to materials like limestone and sandstone [GUM79, GUI89, KLE90, OSM90, FOR91, CAR93, KLE93]. For these materials a good signal is observed for TE of the order of 2 ms or more and TR > 300 ms. These materials can therefore be imaged by more or less standard MRI (Magnetic Resonance Imaging) equipment. However, in many common porous building materials, like fired-clay brick or mortar, usually large amounts of paramagnetic ions (e.g., Fe) are present. (The red colour of fired-clay brick and the grey colour of mortar is due to Fe). This complicates the NMR measurements by two effects. First, due to the large susceptibility of the porous material, the transverse relaxation time T_2 will be drastically decreased. Secondly, the variations in local magnetic susceptibility will broaden the resonance line and thereby limit the spatial resolution.

A typical example of the variation of the intensity of the spin-echo signal obtained with straightforward $(90_x\text{-}\tau\text{-}180_{\pm x})$ Hahn pulse sequences with the spacing τ between the pulses is given in figure 3.1 for one type of fired-clay brick.
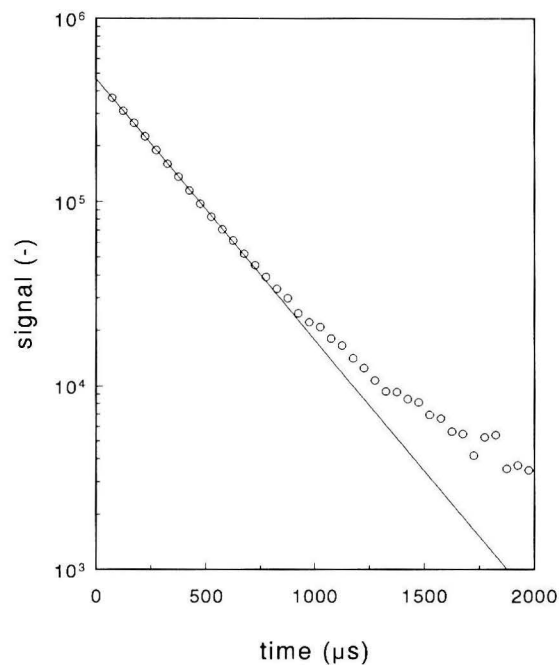
Figure 3.1 Intensity of the spin-echo signal of one type of fired-clay brick (RZ) as a function of the spacing between the RF pulses of the Hahn sequence. The straight line represent an approximation of the data for $\tau < 700$ µs by an effective relaxation time T_2.

This figure reveals that the transverse relaxation process cannot be described by a single exponent, in accordance with the results of other NMR studies on porous materials [BRO79, KLE90, KLE93]. At small values of τ, the fluid in both the small and the larger pores contributes to the spin-echo signal, giving rise to a very short effective relaxation time T_2. At the larger values of τ, on the other hand, the signal is dominated by the fluid in the larger pores, of which the relaxation time is considerably longer. A fit of a straight

line to the data in figure 3.1 yields an effective T_2 of 310 µs. The results of similar measurements on various building materials are summarized in table 3.1. In this table the values of the longitudinal relaxation time T_1 are included.

type of material	T_1 (ms)	T_2 (µs)	χ (10^{-6} emu Gs^{-1} gram^{-1})
fired-clay brick RH	230	210	2.71
RZ	190	310	2.50
GH	250	360	4.16
GZ	120	240	3.61
VE	300	180	3.43
sand-lime brick	45	850	0.53
mortar MZ	35	1000	0.13
MM	30	950	0.18
gypsum	50	4100	- 0.26
0.1 M CuSO$_4$	-[1]	4600	-[2]

[1] cannot be measured using Hahn sequences

[2] was not measured

Table 3.1 The relaxation times of hydrogen nuclei in various types of porous building materials determined from NMR, assuming a single exponential relaxation, as well as the susceptibility χ at 0.78 T. More information on the properties of these building materials can be found in appendix A.1.

To check to what extent the effective values of T_2 can be related to the amount of Fe in these materials, magnetization measurements were performed on samples of these materials in magnetic fields up to 1 T. In figure 3.2 the results are presented.
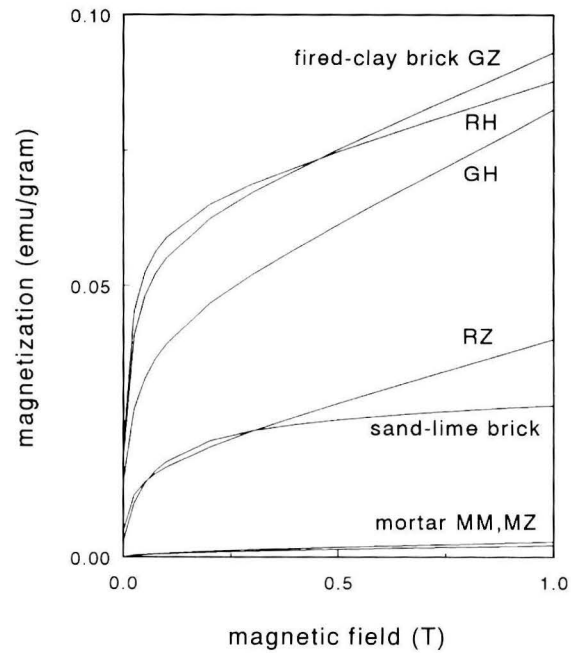
Figure 3.2 Field dependence of the magnetization of various types of building materials. The measurements were performed with a SQUID magnetometer at a sample temperature of 293 K.

The steep increase of the magnetization (M) of the various samples of brick at low magnetic fields, is caused by the presence of inclusions (mass fraction 10^{-4}) of metallic Fe, which are magnetically ordered at room temperature. The relatively slow increase of M at higher magnetic fields is caused by Fe^{2+} or Fe^{3+} ions or very small (superparamagnetic) Fe clusters. An estimate of the mass fraction of these ions or clusters yields values of 1.5 % (assuming Fe^{3+} ions only) to about 6% (assuming superparamagnetic Fe clusters only). This range overlaps the range obtained from chemical analysis of the clay from which these fired-clay bricks are manufactured (see appendix A.1). Table 3.1 also lists the experi-

24

mental values of the susceptibility $\chi = dM/dH$ of the different materials at $B = 0.78$ T, corresponding to the field at which the NMR experiments are performed. Inspection of this table reveals that, apart from minor variations within the group of fired-clay bricks, the value of T_2 tends to decrease when the susceptibility, and hence the Fe content, increases. A very crude estimate of the local field variations in the porous materials can be obtained by assuming that these variations are related to the volume susceptibility. For the various types of fired-clay brick this approach yields variations of about 0.05 to 0.08 mT.

In principle the linewidth of NMR signal can be obtained by measuring the time constant T_2^* describing the so-called free induction decay of this signal in a homogeneous magnetic field. For various kinds of fired-clay brick, values of T_2^* ranging from 20 to 30 µs were observed, corresponding to a linewidth of the order of 8 kHz, which corresponds to local field variations of 0.2 mT. The order of magnitude of these field variations agrees fairly well with the range of 0.05 to 0.08 T estimated from the susceptibility measurements.

These characteristics of porous building materials present special demands on the strategy of the measurements and the hardware performance. Since the transverse relaxation times of the hydrogen nuclei are very small, the duration of the RF pulses should preferably not exceed a few tens of microseconds. To achieve a spatial resolution in the order of 1 mm, magnetic field gradients of about 0.3 T/m (30 Gs/cm) are required. Since the primary goal of the NMR experiments is the investigation of one-dimensional moisture profiles, both static and dynamic, no attempt was made to switch the field gradients during the individual pulse sequences, i.e., within 20 µs. The spin-echo signal was excited by using straightforward Hahn sequences at a fixed strength of the magnetic field gradient.

Since the time scale of the experiments covers the region from a few seconds to a few days the measurements are fully automated. The scanning of a moisture profile and its time dependence over the sample requires a strong interaction between the settings of the RF system, magnetic field gradient, sample positioning, and sample conditioning. To achieve the necessary flexibility a fully modular RF system was developed. All relevant settings of this system can be controlled by a general purpose data-acquisition system, which will be described in the next section.

25

3.2.2 RF SECTION AND DATA-ACQUISITION

Except for a linear 100 W RF power amplifier and a HP 8657A frequency synthesizer, the entire RF section is built up from small circuit blocks, which are commercially available ([ANZ91, MIN91, SYN91]). In figure 3.3 a schematic diagram of the RF receiver section is shown.
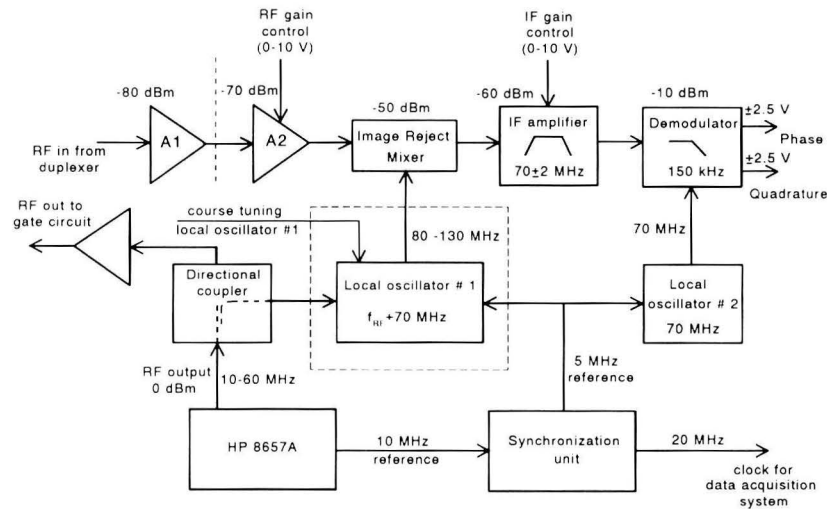
Figure 3.3 Schematic diagram of the RF receiver section. In this section the RF spin-echo signal is amplified, demodulated and filtered. The resulting phase and quadrature output signals are fed to the analog-to-digital converters of the data-acquisition system. The section also supplies a 20 MHz master clock for this system and generates the RF input signal for the gate circuit of the power transmitter. The local oscillator #1 is plotted in more detail in Fig. 3.4.

This receiver covers the RF frequency range from 10 to 60 MHz, corresponding to experiments in magnetic fields between 0.25 and 1.5 T. All relevant settings (gain, phase, local oscillator frequency) can be controlled by applying DC voltages in the range 0-10 V to the corresponding inputs. These voltages are supplied by a 12 bit, 8 channel DAC. The video

output voltages appearing at the outputs P and Q are in the range -2.5 to +2.5 V, suitable for most fast ADC's.

The spin-echo signal at the input is first amplified by A_1. For this section a circuit block type CDM23 was used, manufactured by ADE [AVA91], which has a gain of 9 dB and a noise figure F=1 dB in the frequency range of interest, and is located close to the LC circuit containing the sample (see Section 3.2.3). Next, the signal is amplified by section A_2, consisting of a 28 dB amplifier (MCL MAN-1LN), a voltage controlled attenuator (MCL PAS-1), a 18 dB amplifier (MCL MAN-2), and a 3 dB fixed attenuator. The latter attenuator is inserted to rule out instabilities due to impedance mismatch between the various sections. Section A_2 offers a gain between 0 and 40 dB, which can be controlled by a DC voltage between 0 and 10 V. Next, the signal is fed into an Image Reject Mixer (Synergy IMP 972), where it is mixed with a local oscillator signal in the frequency range 80-130 MHz. The difference signal f_{LO1}-f_{RF} is processed by an intermediate frequency (IF) amplifier with a pass band of 70±2 MHz and a gain between 10 and 55 dB, controlled by a DC voltage between 0 and 10 V. The intermediate frequency is chosen above the RF frequency range for two reasons. First, the local oscillator signal for the Image Reject Mixer covers a frequency range of less than a factor 2, and hence it can be excited by a single oscillator circuit. Second, a flat frequency response within several MHz can rather easily be achieved using conventional coupled LC circuits. The IF section consists of a pre-filter, built up from a constant impedance 70 MHz bandpass filter (MCL PIF-70), a high dynamic range 10 dB amplifier (MCL MAN-1HLN), again a MCL PIF-70 filter, and the actual tuned amplifier. This amplifier is built up from, successively, a coupled pair of LC circuits (Q=6), a high dynamic range 10 dB amplifier (MCL MAN-1HLN), a coupled pair of LC circuits, a 16 dB amplifier (MCL MAN-1AD), a voltage controlled attenuator (MCL PAS-1), a 28 dB amplifier with a noise figure below 3 dB (MCL MAN-1LN), a coupled pair of LC circuits, and a 16 dB amplifier (MCL MAN-1AD). To eliminate possible instabilities of the amplifier blocks, due to the large impedance mismatch of the LC circuits outside the pass band, the input and output of each pair of coupled LC circuits are connected via 3 dB fixed attenuators (MCL AT-3). Measurements on the IF section revealed that the frequency response was flat within 0.1 dB within the pass band

70±2 MHz. Apart from this, the recovery time from severe overload conditions (10 dBm input signals) did amount to less than 1 μs.

The output signal of the IF section is fed into a demodulator, consisting of a power splitter (MCL PSC-2-1W) and two identical stages for the in-phase and quadrature signals, respectively. Each stage contains a high dynamic range 10 dB amplifier (MCL MAN-1HLN), a double balanced mixer (DBM) (MCL SRA-1MH), and a video amplifier. The local oscillator signals for the two mixers are supplied by a 70 MHz oscillator. The output of this oscillator is connected to a 90° hybrid power splitter (Synergy DQP 256) and the resulting signals are amplified by MCL MAN1-HLN circuit blocks to a level of about 13 dBm. The video amplifiers consist of an active second order low pass Bessel filter with a -6 dB cutoff frequency of 150 kHz, incorporating an Analog Devices AD841 [ANA91] operational amplifier, followed by an output stage with a voltage gain of 40, incorporating an AD840 opamp. The circuit can drive up to ±2.5 V into a 50 Ω load.

All oscillator frequencies used in the receiver are phase-locked to the 10 MHz reference output of the HP 8657A frequency synthesizer, which acts as a master oscillator. For this purpose the reference output is connected to a phase locked loop (PLL) which contains a 40 MHz voltage controlled oscillator (VCO). From this oscillator a symmetrical 20 MHz TTL compatible output signal is derived, which is used as a clock signal for the interfaces of the data-acquisition system. By further frequency division an internal 5 MHz signal is obtained, to which the local oscillators are phase locked.

The circuit diagram of one of these oscillators (#1) is plotted schematically in figure 3.4. The VCO is a commercially available circuit block (ADE VCO 80-160) yielding an output power of approximately 12 dBm with very low phase noise. Via a fixed 5 dB attenuator (MCL AT-5) and a directional coupler (MCL PDC-20-1W) a small fraction (-25 dB) of the output power of this VCO is fed into an amplifier section (A) consisting of a fixed 5 dB attenuator, an 18 dB amplifier (MCL MAN-2), and a high dynamic range 10 dB amplifier (MCL MAN-1HLN). The resulting +10 dBm signal serves as LO signal for a double balanced mixer (DBM) (MCL SRA-1MH). A fraction of the 0 dBm RF output signal of the HP 8657A synthesizer is connected to the RF input of this DBM via a directional coupler (MCL PDC-20-1W) and an 18 dB amplifier (MCL MAN-2). The

directional couplers and subsequent amplifiers were found to provide sufficient isolation between the synthesizer and the VCO. The output signal of the DBM is led through two constant impedance filters (MCL PIF-70) with a center frequency of 70 MHz to suppress spurious signals, which may hamper correct operation of the phase detector.
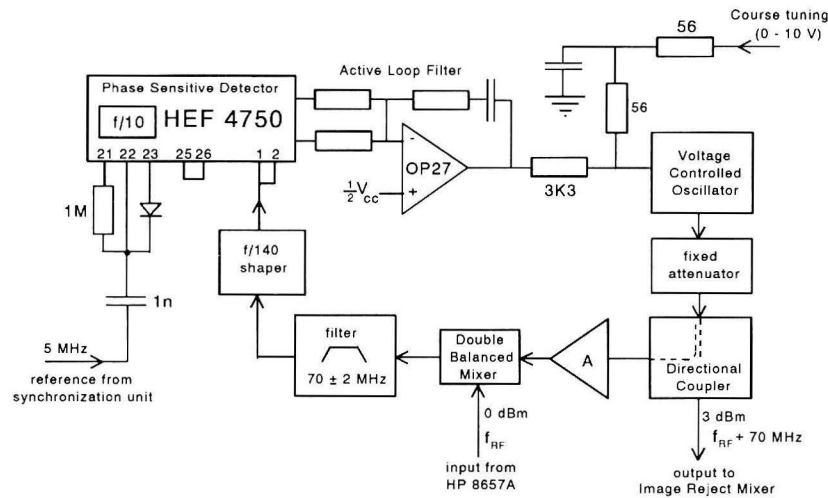
Figure 3.4 Schematic diagram of the local oscillator #1. This circuit generates a signal at a frequency exactly 70 MHz above the RF frequency of the signal used to excite the spin-echo. Synchronization of the various signals is maintained by the 5 MHz signal derived from the reference output of the HP 8657A frequency synthesizer (see. Fig. 3.3).

Next, the signal is converted into a digital signal by a pulse shaper, the frequency is divided by a factor of 140, and the resulting 500 kHz signal is connected to one of the inputs of the phase sensitive detector (PSD) (Philips HEF 4750 [PHI91]). The other input section of this PSD is connected to the 5 MHz reference signal mentioned above, of which the frequency is divided by a factor of 10 in the PSD itself. Phase comparison therefore occurs at a frequency of 500 kHz. The HEF 4750 was chosen because of its very low phase noise and low spurii. Apart from this, the gain of the phase detector of this device

in locked condition is very high (typically 1 kV/rad) and hence the noise contribution from the active loop filter (OP27) can be neglected. Because of the presence of the 70 MHz bandpass filter at the output of the DBM, the VCO has to be set to within 2 MHz from the desired frequency (f_{rf} + 70 MHz) before the PLL will operate correctly. Therefore the output of the loop filter is connected to the control input of the VCO via a 30:1 attenuator, whereas a DC voltage in the range 0 to 10 V is applied to a coarse tuning input. The phase locked loop of the local oscillator module #2 is largely identical to that of module #1, except for the amplifier section A and the DBM, which are omitted, whereas a voltage controlled phase shifter (Synergy PP-904) is placed at the output.

The phase noise introduced by these local oscillators was found to be very low: measurements in which the output of the HP synthesizer was connected to the receiver input via a 40 dB attenuator revealed a phase noise of the P,Q output voltage vector of less than 1 degree over the entire RF frequency range. By changing the RF and IF gain settings, input signals in the range -100 dBm to -20 dBm could be handled without complications. The recovery time of the complete receiver chain after a +10 dBm input signal was found to be less than 5 μs, which is much smaller than the time between the second RF pulse of the Hahn sequence used to excite the spin-echo and the start of the spin-echo signal itself (>20 μs).

The transmitter section consists of a gate circuit and a 100 W linear RF power amplifier. As input signal for the gate the 0 dBm RF output signal of the HP 8657A synthesizer is used, which is first led through a directional coupler (see Fig. 3.3), a fixed 3 dB attenuator (MCL AT-3), and a MCL MAN1-HLN 10dB amplifier. The RF gate circuits are identical to that described in CLA87, except that fixed 3 dB attenuators (MCL AT-3) have been included at the input and output to reduce the impedance mismatch and spurious harmonic contents of the output signal. One of the double balance mixers (MCL SRA-1H) in the first gate circuit is switched with either a positive or a negative current, thus providing a zero or 180^0 phase shift of the RF output signal. By using two RF gates, which are fairly well isolated from each other, an on-off ratio exceeding 100 dB was obtained.

To connect the LC probe circuit to either the transmitter or the receiver section a duplexer is used that incorporates series-parallel switches of 500V PIN diodes (MA4P506

[MAC91]). These diodes are biased with 50 mA in forward direction ($r_s \sim 0.3$ Ω) or with -60 V in reverse direction ($c_j = 0.7$ pF) by complementary pairs of fast switching transistors. The duplexer is switched about 500 ns before and after the RF gate circuit is activated, using a TTL compatible logic signal supplied by our timer interface.

The data-acquisition system, which is schematically plotted in figure 3.5, is controlled by a processor module (M68030 CPU and M68882 coprocessor) that is interconnected with a 16 Mbyte global memory module via an industry standard VME/VSB bus system. Via the VME bus the CPU communicates with a Local Area Network controller and a so-called VME/PhyBUS converter. The latter offers a transparent coupling (including DMA facilities) between the VME bus and a user defined bus (PhyBUS), which accommodates the various interfaces, that will now briefly be discussed.
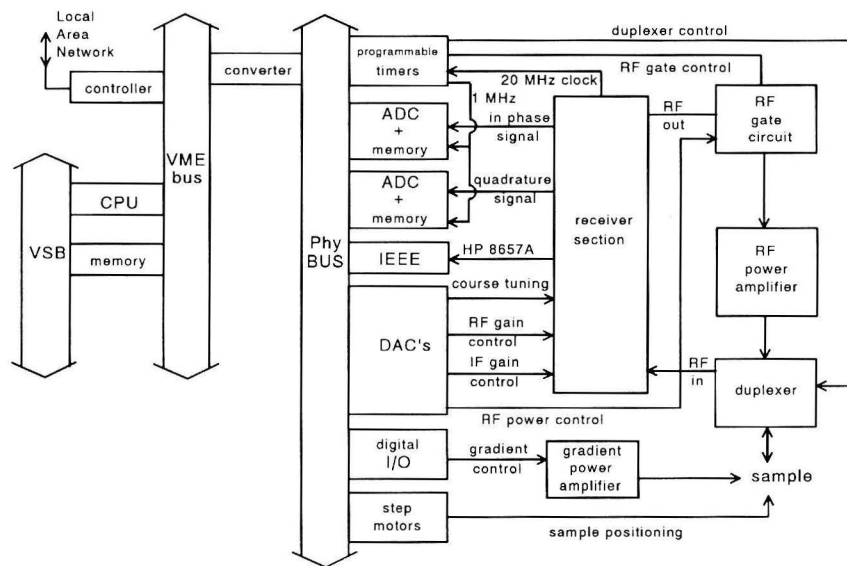

Figure 3.5 Block diagram of the data-acquisition system and the RF receiver/transmitter sections. The receiver section is shown in more detail in Fig. 3.3.

31

Via a 12 bit 8 channel DAC a voltage in the range 0 to 10 V can be applied to the RF and IF gain control inputs, the coarse tuning input of local oscillator #1 (see Fig. 3.3 and Fig. 3.4), as well as the phase control input of the receiver and the RF power control input of the transmitter driver. Two channels of the step motor interface are connected directly to the drivers of the step motors used for sample positioning. One of the channels of the logic (0-5 V) Input/Output system is used to activate a Power Mosfet circuit that switches the current through the field gradient coils. As was already mentioned in section 3.2.1, the magnetic field gradient is kept at a constant (preset) value during the individual pulse sequences. During the time intervals between adjacent sequences the current through the gradient coils is switched off to avoid excessive heating.

The industry standard IEEE interface communicates directly with the HP-IB interface of the HP 8657A synthesizer. Apart from the initialization routine, this communication is mainly used to set or change the RF frequency during the scans of the moisture profile. The timer section has several functions. First, it performs a frequency division of the 20 MHz master clock signal, providing a 1 MHz trigger signal for the ADC's connected to the P and Q output of the receiver. Second, it contains several programmable timers/preset scalers which are used to generate the 90°/180° RF pulses of the Hahn sequences, the switching signal for the multiplexer, and a gate signal for the ADC-triggers. All timing signal are synchronised to the 20 MHz clock; they can be adjusted with a resolution of 50 ns.

The P and Q signals are digitized by 12 bit ADC's at a rate of 1 MHz, which exceeds the cut-off frequency of the Bessel filters in the video output stages by more than a factor 6. The resulting digital values are stored as 16 bit numbers in successive locations of 2 Mbyte dual ported static memory modules with auto-increment address registers. The ADC is triggered only during the time interval that the spin-echo occurs, i.e., for a period of 512 μs after the second RF pulse. After a number of spin-echo signals have been collected, the contents of the memory modules are transferred to VME memory for further processing.

3.2.3 EXPERIMENTAL SET-UP

The samples used in the experiments are cylindrical rods with a diameter of 20 mm and a length varying between 20 and 200 mm. They can be inserted in a cylindrical coil with an inner diameter of 35 mm, made of 7 turns of 1 mm Cu wire. This coil forms part of a tuned LC circuit and is placed within a shielded box. Since the aim of the NMR experiments is to perform quantitative measurements of the moisture profile, the LC circuit has to be carefully matched to the characteristic impedance of the equipment (50 Ω), whereas changes in the RF losses or detuning of the circuit due to variations of the moisture content of the sample should be as small as possible. To reduce the effect of variations of the dielectric permittivity of the sample, a cylindrical Faraday shield has been placed between the coil and the sample. This shield consists of 0.5 mm insulated Cu wires running parallel to the axial direction of the coil. The wires are electrically interconnected and grounded at the lower side of the shield. A small slit in this part of the shield prevents the generation of Eddy currents and consequent RF power losses.

The coil is part of a series tuned circuit, shown in the inset of Fig. 3.6. Impedance matching is achieved by adjusting the capacitor C_p. To minimize detuning by the presence of a sample the quality factor Q of the circuit has been reduced to Q≈40 by adding a series resistor r_s. At this moment the equipment is operated at frequencies near 33 MHz, corresponding to an applied field of 0.78 T. This field was chosen as a compromise between the signal-to-noise ratio of the spin-echo signal, which increases at higher frequencies, and the line broadening due to the presence of magnetic impurities, which leads to a decrease of the resolution at higher magnetic fields. The magnet is a conventional water cooled, iron cored, electromagnet. The poles of this magnet have a diameter of 200 mm and are 50 mm apart. The magnetic field has a stability better then 5×10^{-5} T/week and a homogeneity of 4×10^{-5} T within a sphere with a diameter of 10 mm.

A magnetic field gradient is generated in the vertical direction by a set of conventional Anderson coils [AND61]. To achieve a spatial resolution in the order of 1 mm gradients up to 0.3 T/m are needed. The coils were found to provide a field gradient which was constant within 1% over 30 mm in the vertical direction. Using the LC circuit described

above, a 90° turning angle of the ^1H spins can be achieved with pulses having a duration of 15 µs, corresponding to a RF magnetic field amplitude $B_1 \simeq 0.4$ mT.
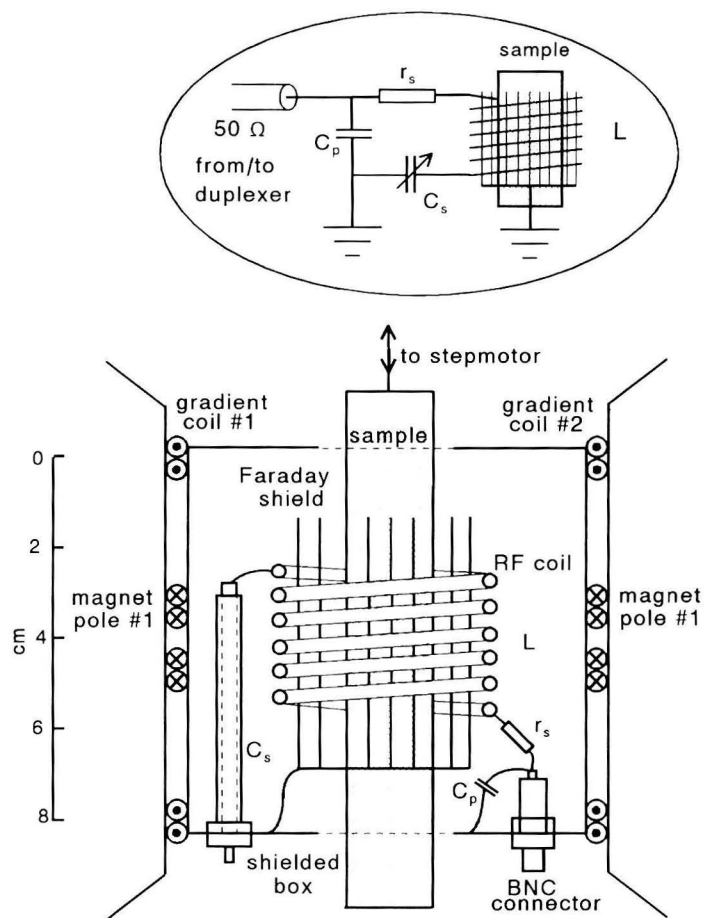

Figure 3.6 Schematic diagram of the RF probe head that accommodates the sample. The homogeneous magnetic field B_o points in the horizontal direction, whereas the two gradient coils generate a magnetic field gradient in the vertical direction. The inset shows the electronic equivalent circuit.

Because of the large field gradient, a measurement of the spin-echo signal and subsequent Fourier transformation yields a moisture distribution within a vertical region of only 2 to 3 mm. To determine the moisture profile over a larger region, the sample can be moved in the vertical direction with the help of a step motor. In some experiments, e.g., drying, where the temperature, air flow, and relative humidity have to be controlled, it is preferable to measure the moisture profile without moving the sample. This can be realized by changing the RF center frequency f_c; for a typical magnitude of the field gradient a frequency shift of 100 kHz corresponds to a shift of the selected region of 7 mm. These kinds of experiments are performed without retuning the LC circuit, since that would give rise to an unacceptable low speed of the measurements.

Figure 3.7 shows the results of such an experiment on a homogeneous reference sample, i.e., a quartz tube filled with 0.1 M solution of $CuSO_4$ in water. The Fourier transformed spin-echo signals at various RF center frequencies are denoted by curves, each reflecting the region selected at that particular value of f_c. The set of solid curves is called a reference profile. Inspection of the figure reveals that the maximum observed spin-echo intensity decreases when the frequency is shifted away from the value of f_0 corresponding to the center of the coil. This decrease, denoted by the 'envelope' of the curves (dashed curve in Fig. 3.7), is a largely geometrical effect, resulting from the finite length of the RF coil. This was checked by decreasing the magnitude of the field gradient by a factor of 2, which did hardly affect the envelope of the dotted curve (in spatial coordinates), although the corresponding frequency shifts decrease by the same factor. In this respect one has to note that the quality factor of the LC circuit ($Q \approx 40$) has only a small effect on the shape of the curves presented in Fig. 3.7, since it causes a decrease of sensitivity by 3 dB for a frequency shift of at least 400 kHz.

An actual moisture profile is determined by measuring the spin-echo signal of the sample of interest at a number of RF frequencies, that exactly match the frequencies at which the reference profile has been determined. The signal detected at each frequency f_c is Fourier transformed and the result $I(f_c, f-f_c)$ is divided by the intensity of the corresponding points of the reference profile. By doing so the geometrical effect is eliminated, as was checked by measurements on various phantom samples. The results of this point by point division

at various values of f_c are combined to obtain the overall moisture profile over about 28 mm. In this process only the data around the maximum of each curve at fixed f_c are taken, since they have the best signal to noise ratio.
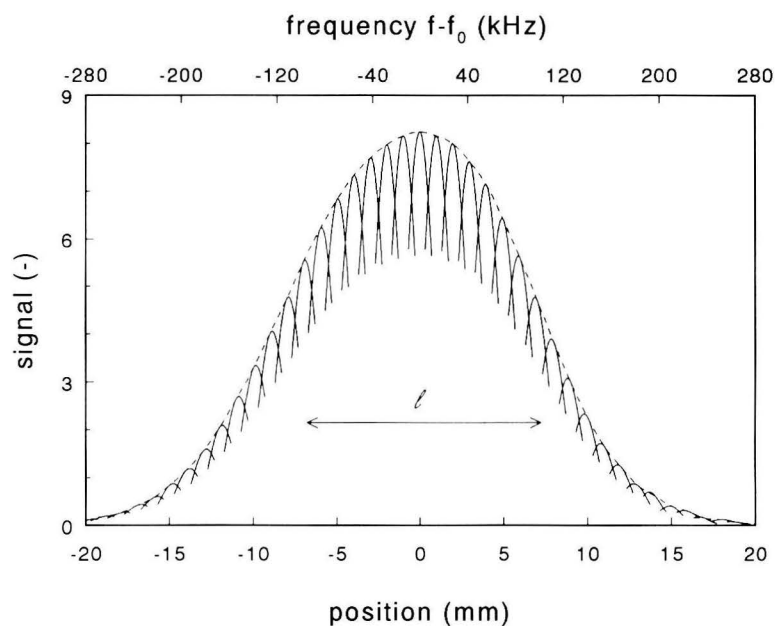
Figure 3.7 Typical reference profile obtained from a sample with a homogeneous moisture distribution. The frequency f_0 corresponds to the center of the coil. Solid curves represent the Fourier transforms $I(f_c, f\text{-}f_c)$ of the spin-echo signals detected at a series of RF center frequencies f_c. Because of the presence of a magnetic field gradient, each of these curves reflects a slice of the sample selected at that particular value of f_c. Only the parts of these curves with the largest contribution to the signal are plotted. The dashed curve (a kind of 'envelope') reflects the effect of the finite length of the RF coil, which gives rise to a decreasing sensitivity as the selected slice moves away from the centre of the coil. The horizontal arrow marked l denotes the region occupied by this coil. The total set of the solid curves is used as a reference profile.

36

Generally, measurements on saturated samples are used to calibrate the apparatus for a certain sample material, which offer the possibility to determine the corresponding moisture profiles with an absolute accuracy of a few percent. In figure 3.8 a picture is given of the NMR equipment.
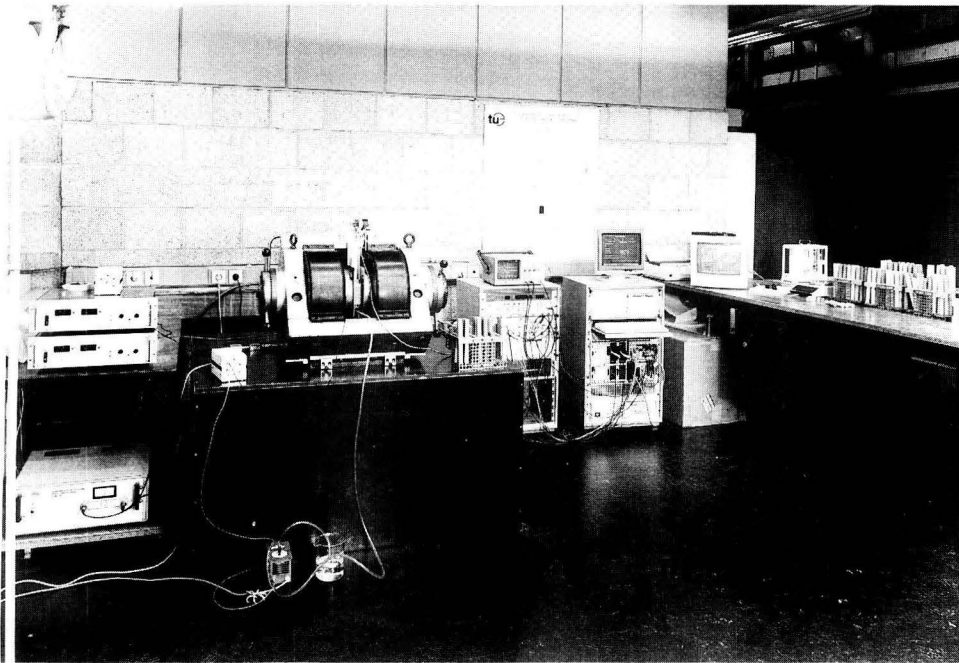
Figure 3.8 Picture of the NMR equipment.

3.2.4 TYPICAL PERFORMANCE

The one-dimensional spatial resolution of the equipment was evaluated by measurements on cylindrical samples with a flat top or bottom. The moisture profile near the flat surface of such samples was obtained following the procedure sketched in section 3.2.3, and is presented in figure 3.9 for various materials. For a phantom sample containing 0.1 M

solution of $CuSO_4$ in water the resolution amounts to about 0.8 mm, whereas for both saturated porous materials the resolution is 10 to 20 % worse. This is due to the presence of inhomogeneously distributed para- or ferromagnetic impurities in these materials, which induce local random magnetic fields and hence a significant line broadening (see section 3.2.1).
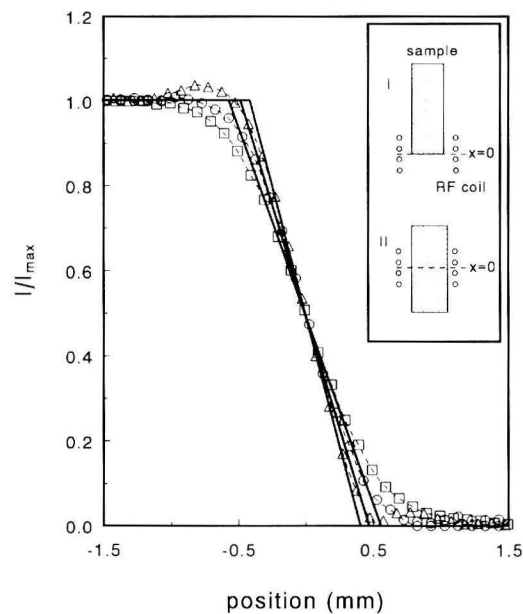
Figure 3.9 One dimensional spatial resolution for several materials: ($\triangle$) 0.1 M CuSO$_4$ solution, (O) lime-sand brick, ($\square$) fired-clay brick (VE). The inset of the figure illustrates how this resolution has been determined. First, a raw profile is measured using a cylindrical sample of which the flat top or bottom is positioned near the centre (x=0) of the RF probe head (I). Next, the reference profile of the sample is measured by positioning the homogeneous region of the sample in the probe head (II). Finally, the two profiles are divided point-by-point, yielding the plotted profiles. (Spin echo experiment: Hahn sequence; $T_{90°}=15$ μs, TE=190 μs, TR= 4T$_1$ (see table 3.1), and gradient 0.3 T/m).

Next, the absolute accuracy of the equipment was tested by measurements on various series of samples with a different moisture content. In figure 3.10 the integrated moisture profiles obtained from a series of NMR experiments on four types of building materials plotted against the corresponding masses of water, which were determined independently by the gravimetric method.
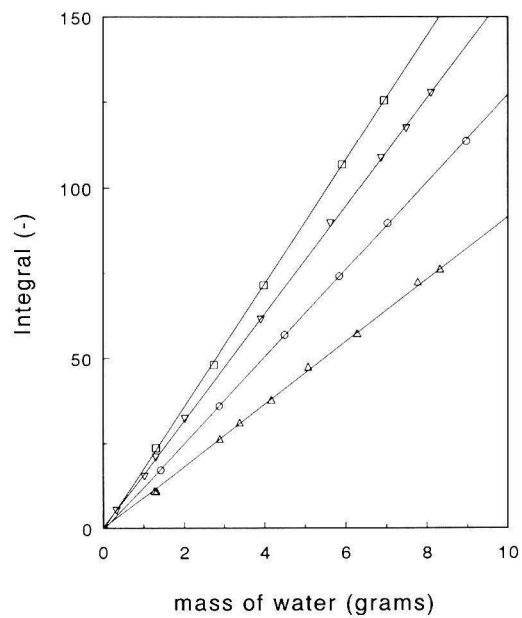
Figure 3.10 Calibration of the NMR-signal for gypsum (□), lime-sand brick (▽) and fired-clay brick, type GZ (○) and VE (△). For different values of the moisture content, the moisture profile of a sample of a certain material is determined by NMR measurements, and subsequently integrated over the entire sample. The resulting values of the integral are given along the vertical axis. The corresponding masses of water present in the sample during these measurements are determined by gravimetric method and are given along the horizontal axis. From the slope of the straight line describing the data for a certain sample an absolute calibration of the NMR signal for that material can be obtained. (Spin echo experiment; Hahn sequence: $T_{90°}=15$ μs, TE=190 μs, TR= $4T_1$ (see table 3.1), and gradient 0.3 T/m).

Since it is intended to determine the total moisture content, the distance between the pulses of the Hahn sequences was kept as short as possible, i.e., 80 μs (TE = 190μs). As can be seen from fig 3.10, in all cases a perfect linear behaviour was found. The scatter of the data is comparable to the observed signal to noise ratio (~2%). Typically, it takes about 40 s to determine the moisture content at a specific position with an absolute inaccuracy of about 1% and a one-dimensional resolution in the order of 1 mm.

The resulting calibration constants are given in table 3.2 and vary, as expected, with the value of T_2, as can be seen from comparison with table 3.1. Obviously, the NMR signal is strongly dependent on the type of material and therefore results like those presented in Fig. 3.10 and table 3.2 are used to convert observed moisture profiles into absolute values.

type of material	calibration (gram^{-1})
fired-clay brick RH	11.12
RZ	14.13
GH	15.04
GZ	12.61
VE	9.45
sand-lime brick	15.73
mortar MZ	16.62
MM	16.62
gypsum	17.27

Table 3.2 The calibration of the NMR spin-echo intensity for various types of porous building materials (see fig. 3.10). More information on the properties of these building materials can be found in appendix A.1. (Spin echo experiment; Hahn sequence: $T_{90°}$=15 μs, TE=190 μs, TR= 4T$_1$ (see table 3.1), and gradient 0.3 T/m)

3.3 SCANNING NEUTRON RADIOGRAPHY

3.3.1 GENERAL CHARACTERISTICS

When a beam of neutrons passes through a material, the neutrons will interact with the nuclei of this material (unlike γ-rays, which interact with the electrons). The attenuation of the neutron beam is determined by the cross-section for scattering and absorption [LAN88] of the nuclei present in the sample. Because of the relative large scattering cross-section of hydrogen, the intensity of the transmitted beam strongly depends on the amount of water. Unlike NMR techniques, no distinction can be made between water that is chemically bound or physically bound.

The intensity I of a neutron beam after passing a sample of thickness d is:

$$I = I_0\, e^{-d\sum_i \mu_i} \tag{3.3}$$

where I_0 is the initial intensity of the neutron beam, μ_i the macroscopic attenuation coefficient of component i. For a rigid material with a volumetric moisture content θ and thickness d equation (3.3) reduces to:

$$I = I_0\, e^{-d(\mu_{mat} + \theta \mu_w)} \tag{3.4}$$

The macroscopic attenuation coefficients μ_w and μ_{mat} in this equation are determined independently by measuring the transmission for pure water and dry material, respectively. The moisture content can then be calculated by measuring the transmission I through a sample of given thickness d.

3.3.2. EXPERIMENTAL SET-UP

The neutron radiography experiments were performed at the 2MW reactor of the 'Interfacultair Reactor Instituut' (IRI) of the Delft University of Technology, the Netherlands. The experimental set-up is shown in figures 3.11 and 3.12.

41
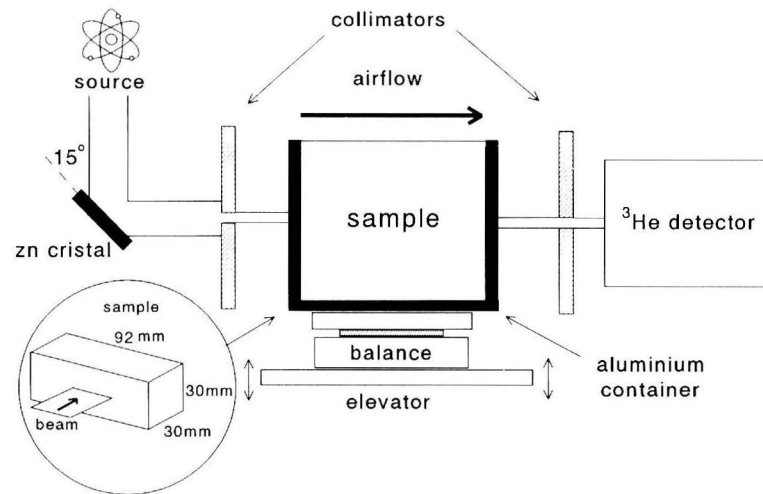
Figure 3.11 Schematic diagram of the experimental set-up for measuring the moisture profiles during drying using neutron transmission. The sample is placed on a balance in order to compare the overall weight with the one obtained from the integral of the moisture profile. In the inset the typical dimensions of the samples used in the drying experiments are given.

For the experiments a monochromatic neutron beam was used with a wavelength of 1.29 Å (corresponding to an energy of 49.3 meV) which was selected by means of (002) reflection of a zinc crystal. To obtain a high spatial resolution, a narrow neutron beam, with typical dimensions of 1 x 30 mm, was made with a collimator consisting of a combination of boron and cadmium. This beam has an intensity of 3.8×10^8 $m^{-2}s^{-1}$. After passing the sample, the neutrons are detected by a ^{3}He proportional detector. This detector has a very high detection efficiency for thermal neutrons and a low one for gamma rays. To correct for the divergence of the transmitted neutron beam and to discriminate against multiply
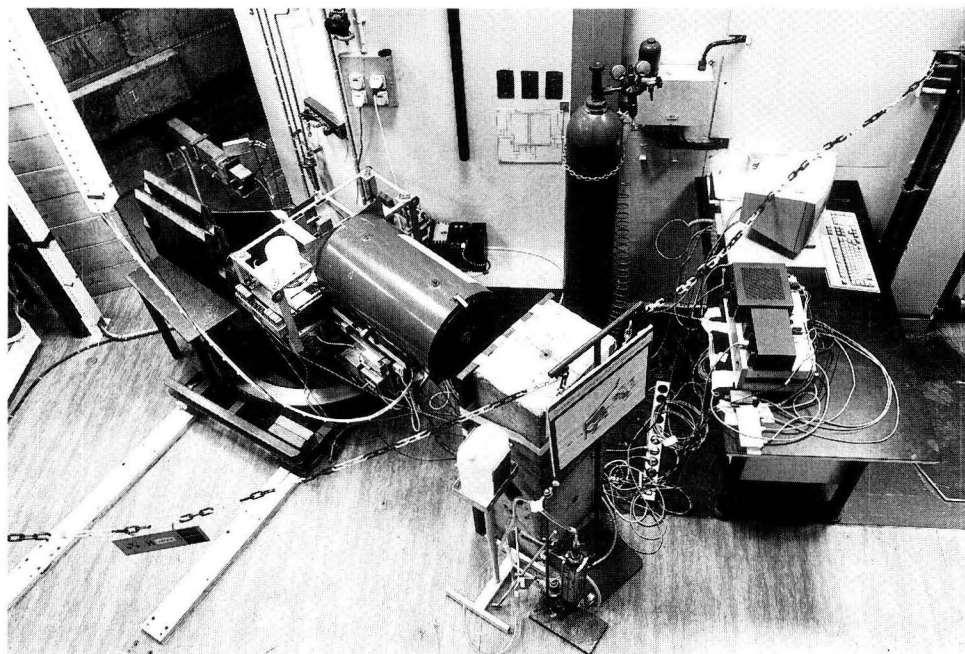
Figure 3.12 Picture of the experimental set-up at the 'Interfacultair Reactor Instituut' at Delft for measuring the moisture content by neutron transmission.

scattered neutrons a second collimator, identical to the first, was placed in front of the detector. To measure a moisture profile the sample was moved through the beam by an elevator.

3.3.3. TYPICAL PERFORMANCE

The neutron beam profile and the alignment of the collimators was checked by slowly moving a plexiglas cube (containing an abundant amount of hydrogen) into the neutron beam, thereby partially blocking it. The result is shown in figure 3.13. The straight line illustrates the uniform intensity of the beam, and the one-dimensional resolution is 0.7 mm in this case.
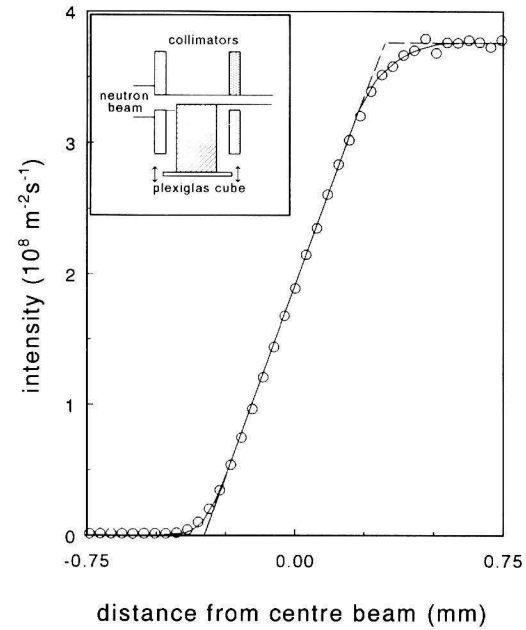
Figure 3.13 Cumulative intensity of the neutron beam as measured by slowly moving a plexiglas cube into the neutron beam and thereby partial blocking it; x=0 corresponds to the centre of the beam. The inset of the figure illustrates the experiment. In this case the effective height of the beam is 0.7 mm.

To determine the macroscopic attenuation coefficients for the various materials under investigation, the transmission was measured for samples of various thicknesses. The results of a calibration are plotted in figure 3.14, and the corresponding attenuation coefficients are given in table 3.3. These attenuation coefficients agree well with those reported for neutrons of this energy [KET92, GRO93]. The samples used in the experiments were typically 30 mm thick, 60 mm wide and had a length ranging between 20 and 200 mm. Measuring the moisture content at a specific position with an inaccuracy of about 1% took approximately 40 s.
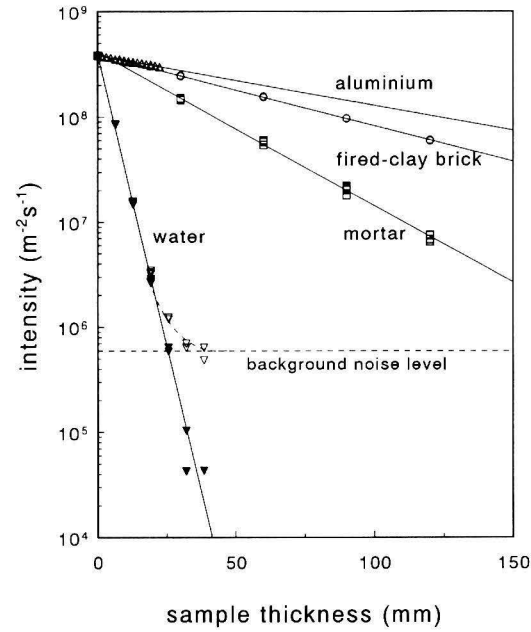
Figure 3.14 Intensity of the neutron beam measured for samples of various thicknesses. For water the intensity is given as measured (▽) and after correction for the background (▼).

type of material	μ (cm^{-1})
water	2.54
fired-clay brick VE	0.155
mortar MZ	0.33
aluminum	0.10

Table 3.3 Macroscopic attenuation coefficients for various materials as determined using neutrons with a wavelength of 1.29 Å (see Fig. 3.12). More information on the properties of these building materials can be found in appendix A.1.

45

3.4 CONCLUSIONS

It is shown that both NMR and scanning neutron radiography offer the possibility to determine quantitative and non-destructive the moisture profiles in a large variety of porous materials. With both methods it takes about 40 s to determine the moisture content at a specific position with an inaccuracy of 1% and a one-dimensional resolution in the order of 1 mm.

Unlike neutron transmission, the signal obtained by NMR is directly related to the amount of hydrogen nuclei in the selected region of the sample. The NMR equipment offers the possibility to determine the moisture profile over 28 mm without moving the sample. An additional advantage of NMR over neutron radiography is that a single spin-echo experiment gives the moisture profile over 1 to 3 mm. Therefore NMR is more efficient for measuring moisture profiles than neutron scanning radiography (i.e., during drying experiments NMR is a factor of 2 to 4 faster). Neutron scanning radiography also has the disadvantage that a nuclear reactor has to be available. Strict safety measures have to be taken and specially trained personal is necessary. Therefore neutron radiography was only used to verify results obtained by NMR.

4 | DETERMINATION OF THE MOISTURE DIFFUSIVITY

4.1 INTRODUCTION

To a good approximation the one-dimensional moisture transport in porous media under isothermal conditions can be described by a non-linear diffusion equation (see Eq. 2.33):

$$\frac{\partial \theta}{\partial t} = \frac{\partial}{\partial x}\left(D_\theta \frac{\partial \theta}{\partial x}\right)$$

(4.1)

The moisture diffusivity D_θ has to be determined experimentally for the porous medium of interest. Up to now often overall techniques, i.e., measurement of the mass as a function of time (e.g., drying curves), are used to determine this coefficient. However, in those cases a relation has to be assumed between the moisture diffusivity and the actual moisture content, which cannot be verified experimentally. These methods will therefore, in general, give an incorrect estimate of the moisture diffusivity (see, e.g., for a drying curve [KET92]).

By measuring transient moisture profiles during various transport processes the moisture diffusivity can be determined directly. In the present study the moisture profiles were measured primarily by Nuclear Magnetic Resonance (NMR). Additional measurements to verify the results obtained by NMR were performed using neutron scanning radiography (see, e.g., [PEL93, SMU94]). Both methods were discussed in chapter 3.

The moisture diffusivity was determined for water absorption and drying of several kinds of inorganic porous building material, i.e., soft-mud machine moulded fired-clay brick, mortar, sand-lime brick (also called calcium silicate brick) and gypsum plaster. More information on various properties of these materials and the preparation of the mortars can be found in appendices A.1 and A.2.

All experiments discussed in this chapter were performed at an ambient temperature of 293 ± 0.5 K.

4.2 WATER ABSORPTION

In the absorption experiments a cylindrical bar with a diameter of 20 mm and a length ranging between 80 and 180 mm of initially dry material was allowed to freely absorb water through one end. The experimental set-up for measuring the wetting profiles using NMR is given in figure 4.1.
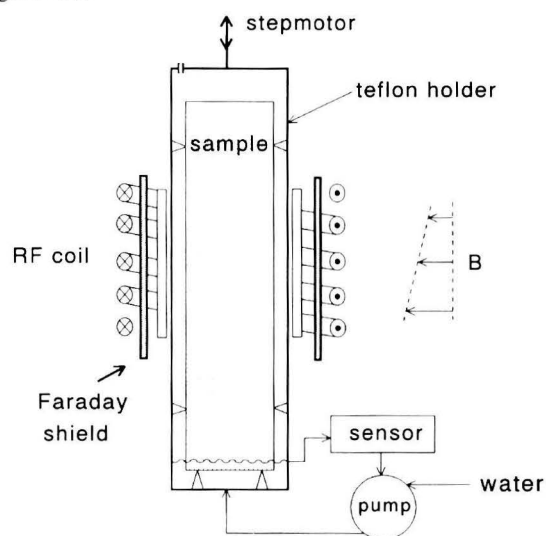
Figure 4.1 Experimental probe head for measuring moisture profiles during absorption. Using an electrical sensor and a pump the water level is maintained constant.

In this set-up the spin-echo experiments are performed at a fixed frequency, corresponding to the centre of the RF coil. Hence only the moisture distribution in a small region of the sample is measured simultaneously (here groups of 5 points). After determination of such a partial profile, the sample is moved in the vertical direction over a few mm with the help of a step motor. This is repeated until a complete wetting moisture profile has been measured. Next, this complete procedure is repeated, now yielding the second moisture profile, and so on. To enable a meaningful interpretation of the measured profiles a time stamp is added to each partial profile.

The resulting moisture profiles are given in figure 4.2 for one type of fired-clay brick (RZ). The moisture content at a specific position could be obtained with an inaccuracy of 2% in about 12 sec. Because of the presence of the electrical sensor and the water reservoir, no meaningful data could be collected for $x < 10$ mm. As can be seen from the measured moisture profiles a very steep wetting front is formed.
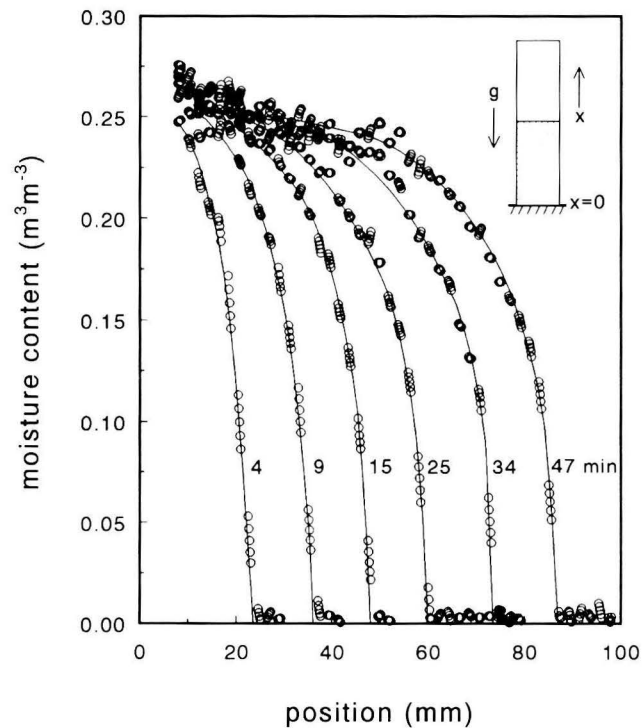
Figure 4.2 Moisture profiles measured during the absorption of water in a fired-clay brick (RZ). Each profile is composed of groups of 5 points. Each group represents the moisture profile obtained from Fourier transformation of the spin-echo signal at one position of the sample. The curves are only meant as a guide to the eye, whereas the times are only given as an indication of the elapsed time. In the inset a sketch of the experimental configuration is given.

The moisture transport during water absorption can be described by equation 4.1 with the initial and boundary conditions:

$$\begin{aligned} \theta = \theta_0 \quad &\text{for} \quad x > 0, t = 0 \\ \theta = \theta_{cap} \quad &\text{at} \quad x = 0, t > 0 \end{aligned} \tag{4.2}$$

In these conditions θ_{cap} is the capillary moisture content, which is the maximum moisture content under atmospheric conditions, and θ_0 is the initial uniform moisture content of the sample.

If the well-known Boltzmann transformation

$$\lambda = \frac{x}{\sqrt{t}} \tag{4.3}$$

is applied, the non-linear diffusion equation (4.1) describing the moisture transport reduces to the ordinary differential equation:

$$2 \frac{d}{d\lambda} \left(D_\theta \frac{d\theta}{d\lambda} \right) + \lambda \frac{d\theta}{d\lambda} = 0 \tag{4.4}$$

with boundary conditions:

$$\begin{aligned} \theta = \theta_{cap} \quad &\text{at} \quad \lambda = 0 \\ \theta = \theta_0 \quad &\text{for} \quad \lambda \to \infty \end{aligned} \tag{4.5}$$

Equation 4.4 with boundary conditions 4.5 has only one solution, so the profiles at different times are related by a simple $\sqrt{t}$ scaling. The moisture profiles for the various investigated types of building material after the Boltzmann transformation, are plotted in figure 4.3.
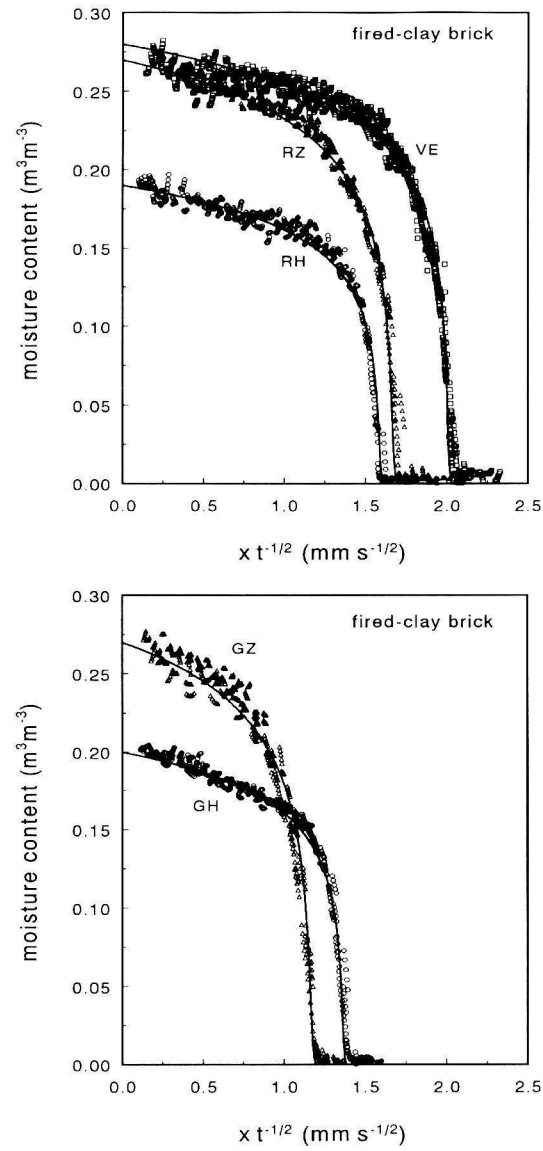
Figure 4.3 (□, △, ○) Boltzmann transformation of the measured moisture profiles for the various kinds of building material. (——) Boltzmann transformation of simulated moisture profiles based on an exponential moisture diffusivity: $D_\theta = D_0 exp(\beta\theta)$. The corresponding coefficients of the moisture diffusivity and the capillary moisture content at the boundary, x=0, are given in table 4.1.

51

Figure 4.3 (second part) (-----) Boltzmann transformation of simulated moisture profiles for gypsum based on the approximation of the diffusivity by two exponential functions (Eq. 4.9). The corresponding coefficients for this approximation are given in table 4.1.

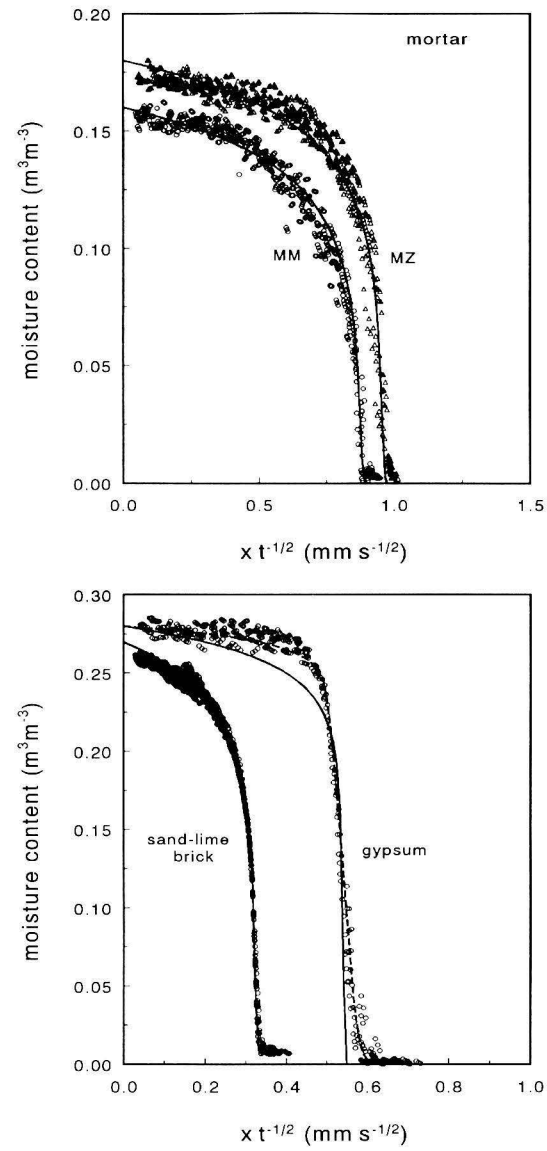For each investigated type of building material the Boltzmann transformation yields a distinct curve, on which the data from the various profiles for that particular materials collapse. This indicates that the moisture diffusivity is not dependent on the position and supports the modeling of the moisture transport during absorption in these building materials by a diffusion equation. The investigated types of building material all show a sharp wetting front. Hence the water penetration coefficient B (the position x of the wetting front divided by $\sqrt{t}$) is a well defined parameter for these materials.

In principle, the moisture diffusivity for absorption can be determined by integrating equation 4.4 with respect to λ using the boundary conditions 4.5, yielding:

$$D_\theta = -\frac{1}{2}\frac{1}{\left(\dfrac{d\theta}{d\lambda}\right)_\theta} \int\limits_{\theta_0}^{\theta} \lambda\, d\theta' \tag{4.6}$$

Using equation 4.6, D_θ can be calculated numerically from the transformed experimental moisture profiles; $\lambda = f(\theta)$. Starting at the intersection of the selected set of data with the horizontal λ-axis (λ_0, θ_0), the data are integrated numerically down to the moisture content of interest. The resulting integral is divided by the local derivative of the averaged set of data with respect to λ at that moisture content. If this procedure is repeated over the full moisture content range, the moisture diffusivity D_θ is found as function of θ. (The numerical procedure to calculate D_θ from measured profiles is given in more detail in appendix A.3). The moisture diffusivities for absorption obtained by this method for the materials given in figure 4.3 are plotted in figure 4.4. Inspection of this figure shows a considerable scatter of the data, which is most pronounced at the highest and lowest moisture contents. This scatter originates from the numerical calculation of the derivative in Eq. 4.6.
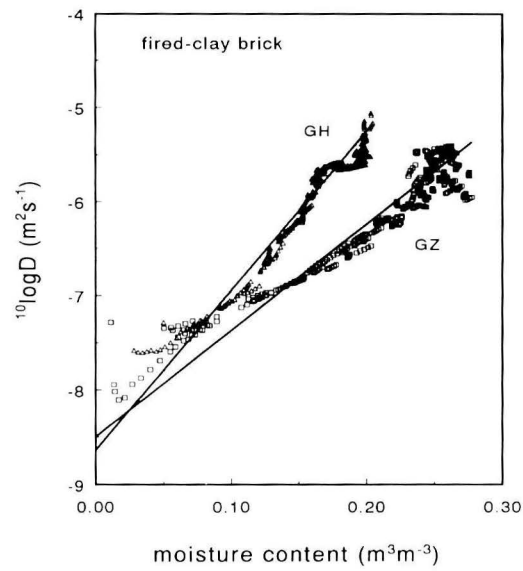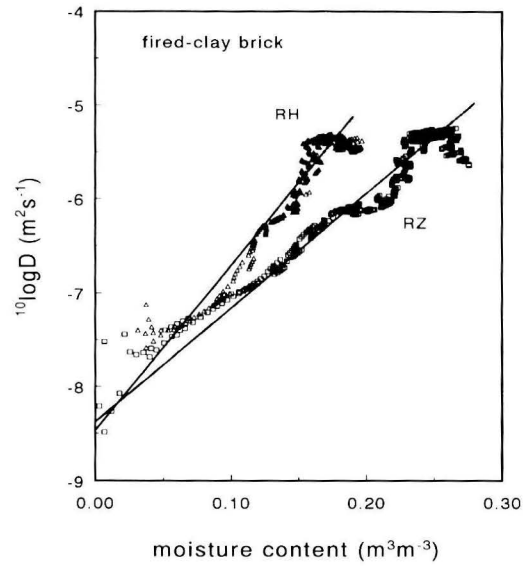
Figure 4.4 (□, △, ○) The moisture diffusivity for absorption as calculated by equation 4.6 from the curve on which the moisture profiles collapse after Boltzmann transformation. (——) Exponential behaviour of the moisture diffusivity (Eq. 4.7) determined by comparing simulated profiles and the corresponding data.
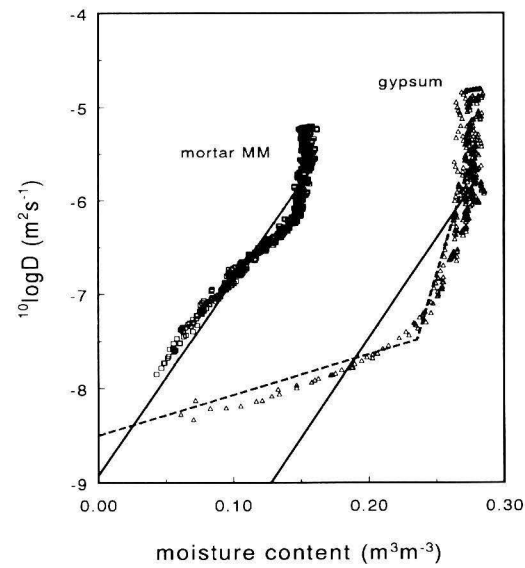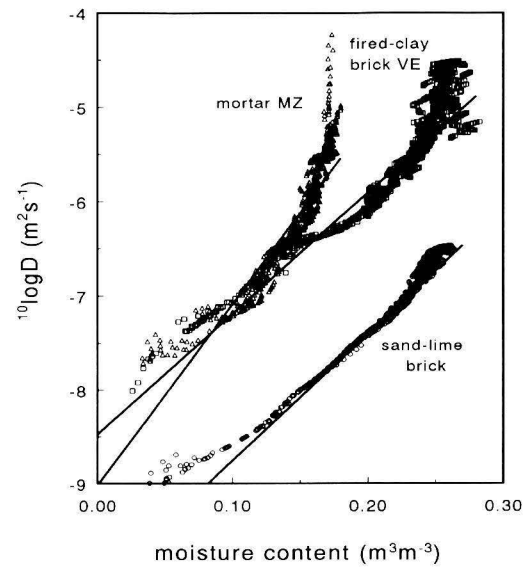
Figure 4.4 (second part) (-----) Moisture diffusivity for gypsum based on the approximation of the diffusivity by two exponential functions (Eq. 4.9) as determined by comparing the simulated profiles and the corresponding data. The corresponding coefficients for these approximations are given in table 4.1.

55

As can be seen from this figure, the overall behaviour of D_0 can be approximated by an exponential function, except for gypsum. An exponential form for the moisture diffusivity for absorption is commonly assumed for all porous materials [GAR58], i.e.,:

$$D_\theta = D_o \exp(\beta\theta) \qquad (4.7)$$

where D_o and β are constants, which depend on the material.
This equation can be rewritten in a normalized form:

$$D_\theta = D_o \exp\left[(\beta\theta_{cap})\left(\frac{\theta}{\theta_{cap}}\right)\right] \qquad (4.8)$$

In the fitting procedure of an exponential function to the various sets of data on the moisture diffusivity in figure 4.4. it is not quite clear which weighing factors should be given to the data points. In this respect one should note that the behaviour of the moisture diffusivity at low moisture contents only has a minor effect on the water absorption. Therefore the coefficients D_o and β were used as adjustable parameters in computer simulations of the Boltzmann transformed sets of experimental data. These parameters were adjusted within their respective tolerance limits given by the fitting procedure until the best agreement between experimental and simulation was obtained. The simulations were performed using standard procedures from the NAG-library [NAG91]. The results are represented by solid curves in figure 4.3. In all cases, except for gypsum, the computer simulation based on a single exponential function gives an adequate description of the observed moisture profiles. (The simulated profiles during absorption are also available in the form of movies; see appendix A.4 + disk). The resulting exponential moisture diffusivities for the various materials are plotted in figure 4.4, whereas the corresponding coefficients D_0 and β are given in table 4.1.
In table 4.1 also the coefficient $\beta\theta_{cap}$ of the normalized diffusivity is given. As can be seen from this table, $\beta\theta_{cap}$ is in the order of 7.5 for most investigated building materials.

56

type of material	D_0 (m²s⁻¹)	β (-)	θ_{cap} (m³m⁻³)	$\beta \theta_{cap}$ (m³m⁻³)
fired-clay brick VE	3.4×10^{-9}	29.5	0.28	8.3
RZ	4.2×10^{-9}	28.0	0.27	7.6
RH	3.4×10^{-9}	40.5	0.19	7.7
GZ	3.2×10^{-9}	26.0	0.27	7.0
GH	2.3×10^{-9}	39.0	0.20	7.8
mortar MZ	9.5×10^{-10}	44.5	0.18	8.0
MM	1.2×10^{-9}	47.5	0.16	7.6
sand-lime brick	7.9×10^{-11}	31.0	0.27	8.4
gypsum (I)	1.9×10^{-12}	49.0	0.28	13.7
gypsum (II) $\theta < 0.236$ $\theta > 0.236$	3.2×10^{-9} 1.65×10^{-19}	9.5 110.0	0.28	-

Table 4.1 The coefficients of the exponential function, $D_\theta = D_0 exp(\beta\theta)$, describing the moisture diffusivity for absorption, and the capillary moisture content, θ_{cap}, determined gravimetrically. For gypsum the moisture diffusivity is given on basis of an approximation by a single exponential function (I) and by two exponential functions (II) (see Eq. 4.9).

In table 4.2 a range of $\beta \theta_{cap}$ for various building materials is given, including the results found in the present study as well as values reported in the literature. In this respect, note that a direct comparison of building materials is not always possible, since the properties of the same type of building material can vary strongly from country to country, due to the manufacturing processes. Nevertheless, the coefficient $\beta \theta_{cap}$ for the various types of building material is found to be roughly the same order, except for gypsum and sand-lime brick. This suggests that for engineering applications one can take a value $\beta \theta_{cap} \approx 7.5$ for inorganic building materials.

source	fired-clay brick	mortar	sand-lime brick	gypsum
Kalimeris [KAL81]	6.3	-	-	-
Krus et al [KRU89]	-	-	6.4	-
IEA [IEA91]	5.6 - 9.2	5.8 - 7.6	6.4	6.3
present study	7 - 8.3	7.6 - 8	8.4	13.7

Table 4.2 The range of the coefficient $\beta\, \theta_{cap}$ of the normalized moisture diffusivity of various types of building materials found in the present study and in the literature.

As can be seen from figure 4.4, the moisture diffusivity for gypsum can be approximated by two exponential functions; each describing the behaviour of D_0 in a different moisture content range;

$$
\begin{aligned}
D_\theta &= D_{0,1}\exp(\beta_1\theta) & \theta \leq 0.236 \\
&= D_{0,2}\exp(\beta_2\theta) & \theta > 0.236
\end{aligned}
\tag{4.9}
$$

The coefficients resulting in the best description of the experimental data are given in table 4.1. whereas the corresponding simulated moisture profiles after Boltzmann transformation are given in figure 4.3. This simulation appears to give an adequate description of the observed moisture profiles. (The simulated profiles during absorption are also available in the form of a movie; see appendix A.4 + disk).

Up till now the moisture transport in single samples was discussed of a certain material. Absorption experiments were also performed on series of samples, on the average 10, of the same type of material. The resulting average moisture diffusivity for various types of brick and mortar are given in table 4.3. The error bounds given for θ_{cap} correspond to the observed range of the waterpenetration coefficient. Figure 4.5 shows the results of computer simulations of the Boltzmann transformed profiles for the average diffusivity.
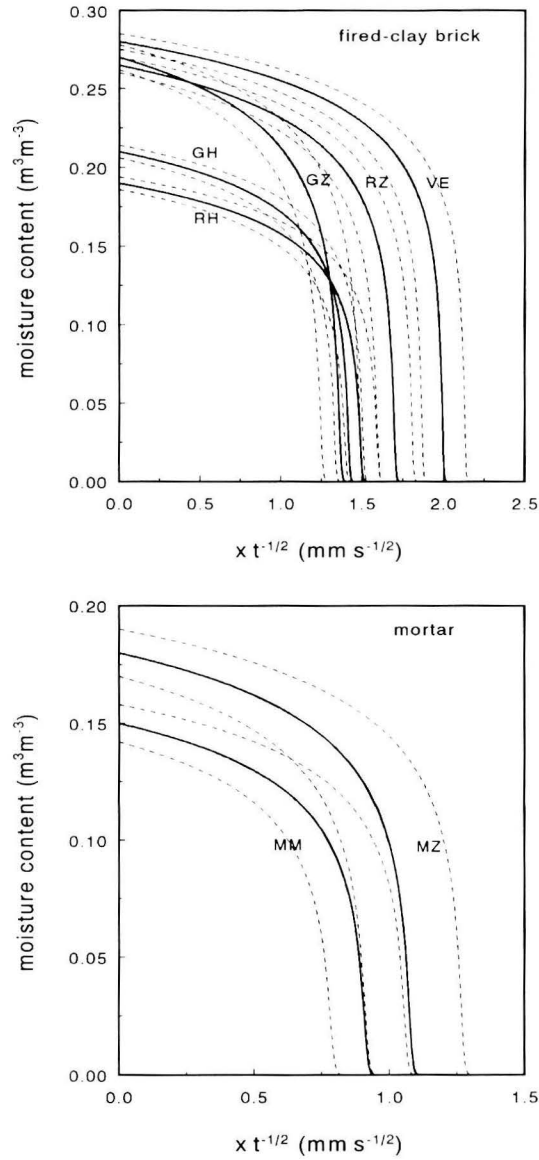
Figure 4.5 (——) Boltzmann transformation of simulated moisture profiles based on the average moisture diffusivity for fired-clay brick and mortar. (------) Boltzmann transformation of simulated moisture profiles corresponding to the maximum and minimum observed waterpenetration coefficients. The corresponding coefficients for these simulations are given in table 4.2.

59

material	D_0 (m^2s^{-1})	β (-)	θ_{cap} (m^3m^{-3})	$\theta_{cap}\,\beta$ (-)
fired-clay brick VE	2.35×10^{-9}	31.0	0.280 ± 0.005	8.7
RZ	3.15×10^{-9}	30.0	0.265 ± 0.005	7.9
RH	3.25×10^{-9}	40.0	0.190 ± 0.004	7.6
GZ	3.50×10^{-9}	27.0	0.270 ± 0.008	7.3
GH	2.55×10^{-9}	37.0	0.210 ± 0.004	7.8
mortar MZ	2.35×10^{-9}	40.0	0.18 ± 0.01	7.2
MM	2.15×10^{-9}	46.0	0.150 ± 0.008	6.9

Table 4.3 The coefficients of the exponential function, $D_\theta = D_0 exp(\beta\theta)$, describing the average moisture diffusivity for absorption of several types of material. The error bounds given for θ_{cap} reflect the observed range of the water penetration coefficient.

4.3 DRYING

The drying experiments were performed using the NMR probe head given in figure 4.6. The sample, a small cylinder with a length of 25 mm and a diameter of 20 mm, is placed in a teflon holder of which the upper side is open (teflon does hardly contain any hydrogen). Air, with a 45 ± 5 % relative humidity (RH) and a temperature of 293 ± 0.5 K, is blown over the sample, thus creating a one-dimensional drying experiment.
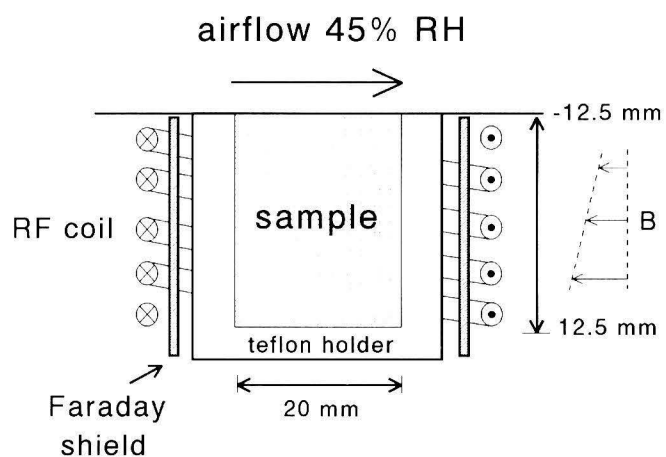
Figure 4.6 Experimental probe head for measuring moisture profiles during drying using NMR.

Using this experimental set-up spin-echo experiments are performed at various fixed frequency's. A spin-echo experiment at one fixed frequency will give the moisture profile within a region of the sample having a height of 0.5 to 1 mm. Because a well known field gradient is applied, the various frequency's can be related to the spatial position. As the

RF coil covers almost the entire sample, a complete moisture profile can be measured without moving the sample. This procedure is described in more detail in section 3.2.3. Measuring an entire moisture profile over 25 mm with an inaccuracy of 1%, a one-dimensional resolution of 1.0 mm (see chapter 3), at 175 equally spaced discrete positions (the grid for scanning) typically takes about 40 minutes. During the measurements a time stamp is added to each point of such an experimental moisture profile. The moisture profile at a specific time is obtained by interpolating subsequent experimental profiles as a function of time for each position of the grid, using least-squares fits with cubic splines.

4.3.1 EXPERIMENTAL RESULTS

Each drying experiment was performed for a period of 40 hours or longer. Examples of the resulting moisture profiles for several types of building materials are plotted in figure 4.7. Inspection of the profiles shows variations, which are substantially larger than the experimental scatter, and reproduce from profile to profile, e.g., for fired-clay brick at a position of 5 mm. The variations reflect the inhomogeneities of the sample. (These measured profiles are also available in the form of movies; see appendix A.4 + disk)

In all cases, except for mortar, a distinct receding drying front is observed after some time. The time evolution of the moisture profiles, however, is quite different for the various materials. For fired-clay brick (RZ) and gypsum a drying front is observed after approximately 6 hours, whereas it takes more than 20 hours for a drying front to develop in sand-lime brick.
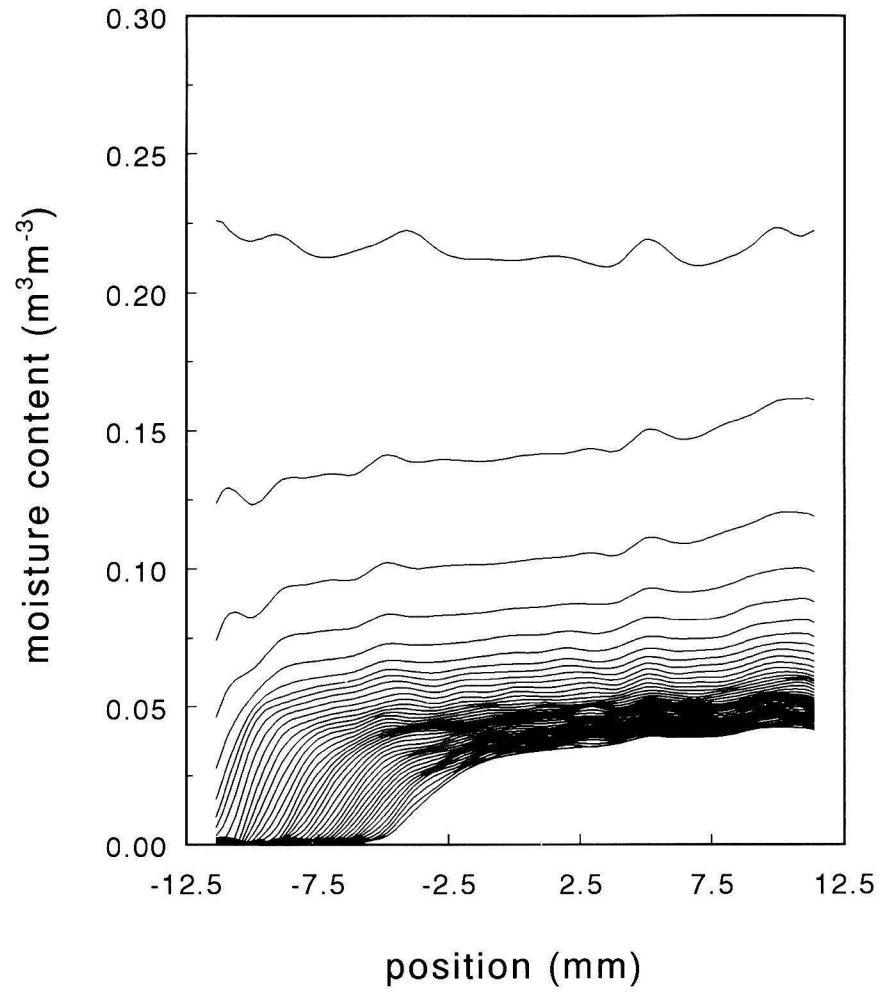
Figure 4.7a Moisture profiles measured during drying for fired-clay brick (RZ). The time between subsequent profiles is 1 hour and the profiles are given for a period of 42 hours.
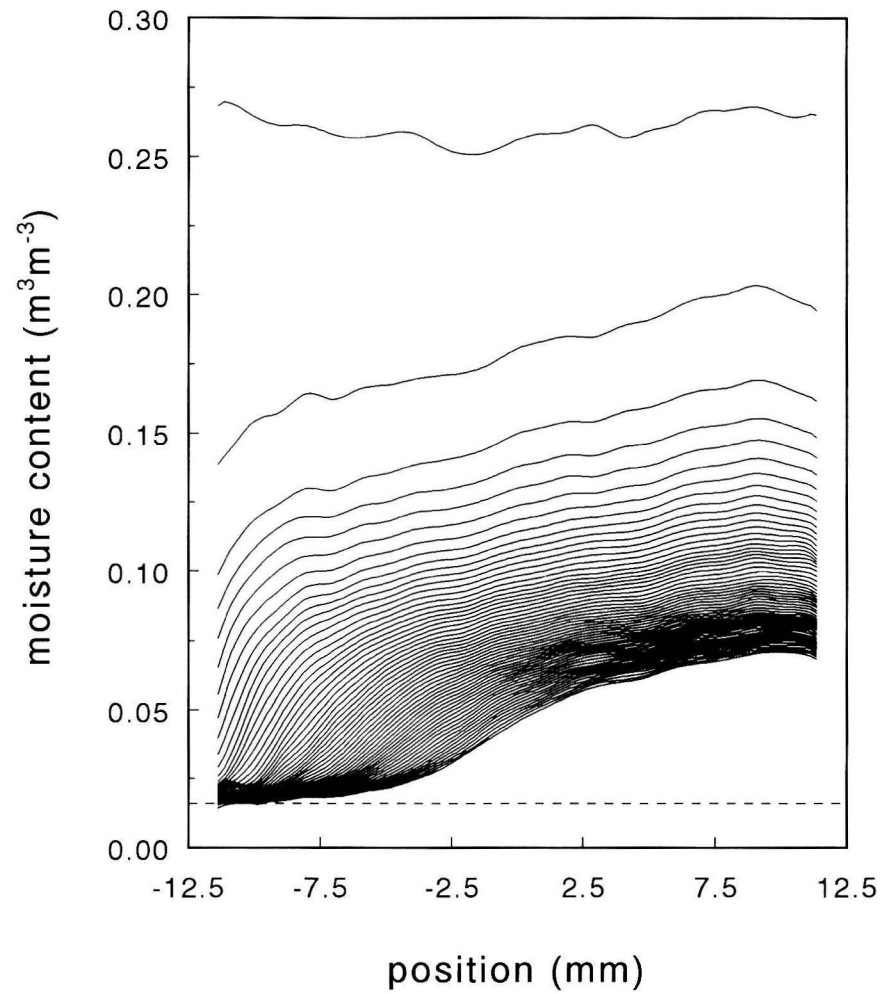
Figure 4.7b Moisture profiles measured during drying for sand-lime brick. The time between subsequent profiles is 2 hours and the profiles are given for a period of 120 hours. The dashed line indicates the residual moisture content observed at 45% relative humidity in this drying experiment.
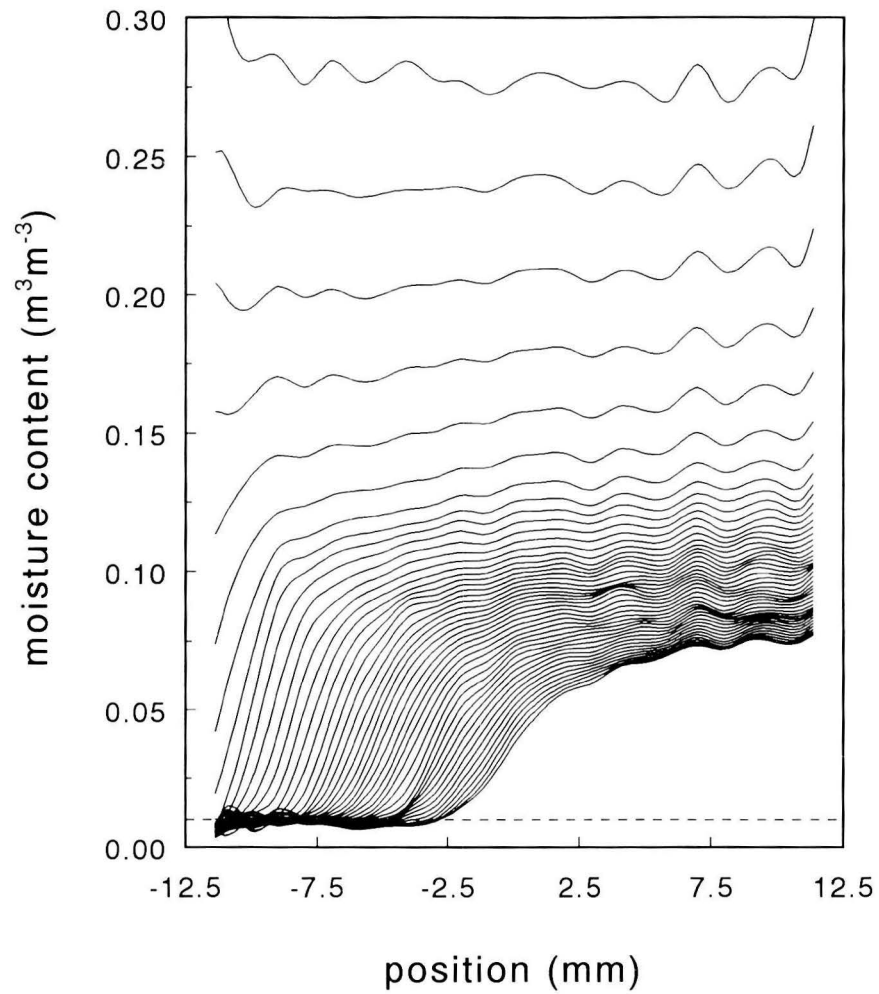
Figure 4.7c Moisture profiles measured during drying for gypsum. The time between subsequent profiles is 1 hour and the profiles are given for a period of 46 hours. The dashed line indicates the residual moisture content observed at 45% relative humidity in this drying experiment.
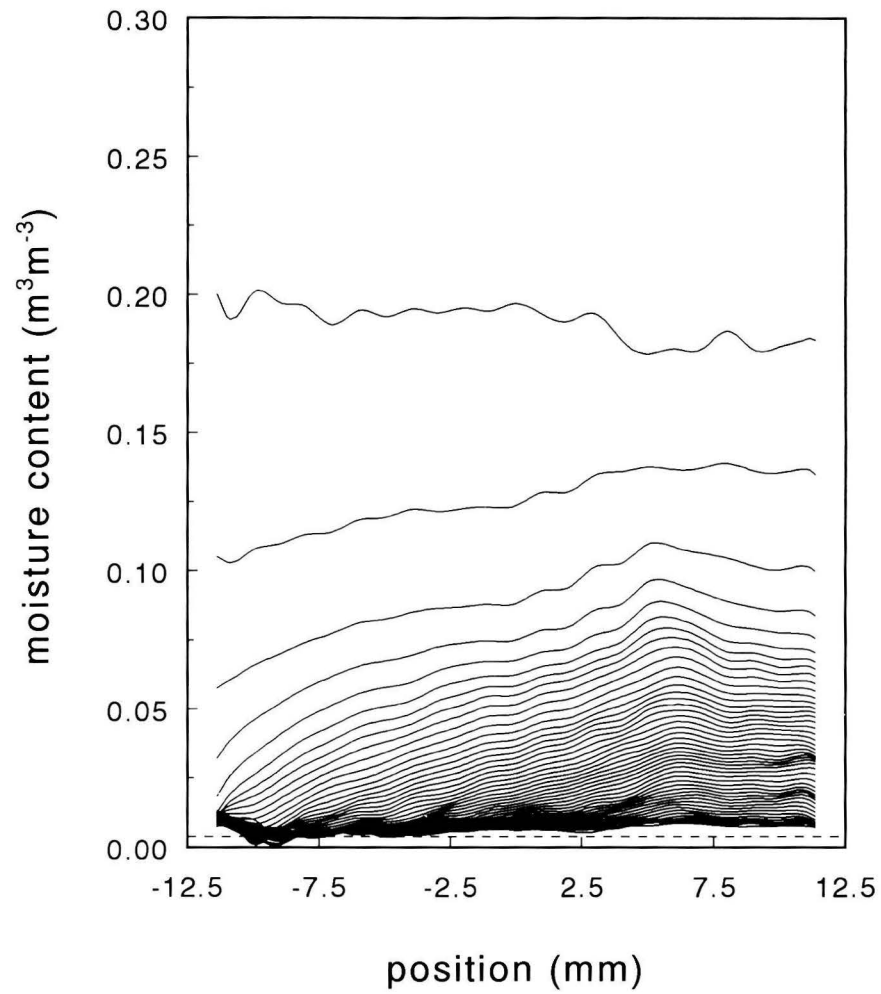
Figure 4.7d Moisture profiles measured during drying for mortar (MZ). The time between subsequent profiles is 1 hour and the profiles are given for a period of 48 hours. The dashed line indicates the residual moisture content observed at 45% relative humidity in this drying experiment.

As can be seen from figure 4.7 mortar is drying fastest and, except for a residual moisture content, it is almost completely dry after 48 hours. A residual moisture content is also observed for both gypsum and sand-lime brick. The hygroscopic curves measured for these building materials are given in figure 4.8.
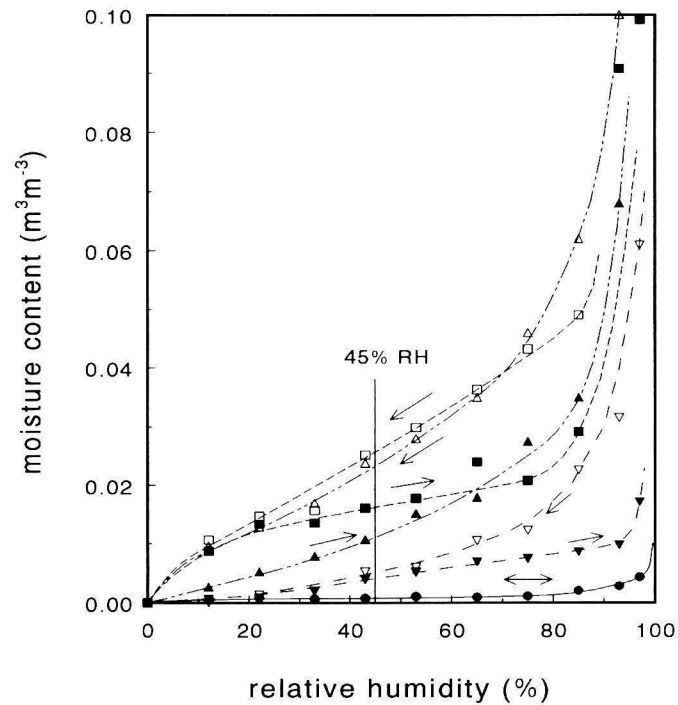
Figure 4.8 Hygroscopic curves; the main curves for absorption and desorption measured for fired-clay brick (RZ) (●), sand-lime brick (■,□), gypsum (▲,△) and mortar (MZ) (▼,▽). The vertical line indicates the relative humidity of the air (45% RH) used in the drying experiments.

These curves were measured by bringing sample in contact with air having a certain relative humidity and waiting for equilibrium. For the sorption curve an initially dry sample was used and for the desorption curve an initially wet sample. So each point on

such a curve represents an equilibrium situation where no moisture transport occurs. Different relative humidities were created by saturated salt solutions. On the average it took 3 to 4 weeks for a sample to reach equilibrium. For gypsum, sand-lime brick, and mortar a clear hysteresis is present. The residual moisture content measured for desorption at 45% RH ranges from 0.1% of the capillary moisture content for fired-clay brick, via 3% for mortar, up to 10% for sand-lime brick and gypsum. The residual moisture content that is observed for these materials in our forced drying experiment, however, is lower then the corresponding value on the desorption curve. In fact it is only slightly higher than the corresponding value on the *absorption* curve for 45% RH. This indicates that during this *forced* drying a desorption curve ending just above the main absorption curve is followed.

As soon as the drying is started, heat will be extracted and the temperature of the top of the sample will decrease and a temperature gradient will develop. In this case the heat flow and hence the moisture transport is no longer a one-dimensional problem. To investigate the magnitude of the temperature gradients, the temperature profile was measured using thermocouples. Since these will disturb the NMR-experiment, these measurements were done separately during a second, similar drying experiment in the same experimental set-up. Two typical temperature distributions as measured for fired-clay brick and sand-lime brick are plotted in figure 4.9. (During neutron scanning radiography the temperature and moisture distribution could be measured simultaneously [PEL93]; the results were largely the same as those obtained with the NMR set-up).

Just after the onset of drying the largest temperature difference is measured. Since heat will start to flow towards the sample, after about one hour a kind of quasi-stationary situation develops, in which the heat flows to and from the sample are almost equal. When the receding drying front enters the material, the drying is internally limited by vapour transport. Hence the drying rate and thus the heat extracted from the sample is strongly decreased; consequently the maximum temperature difference decreases rapidly. Especially for fired-clay brick, where there is a distinct receding drying front, this transition is seen clearly. About two hours later, i.e., about 8 hours after the start, the experiment can be regarded as isothermal.
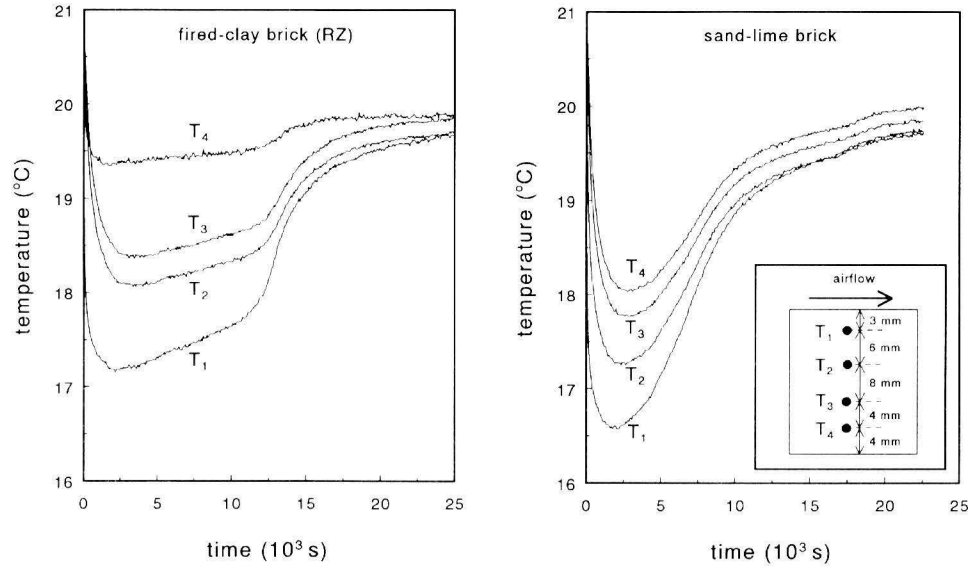
Figure 4.9 Measured temperatures during drying for fired-clay brick (RZ) and sand-lime brick. In the inset the positions of the thermocouples are shown.

To derive D_θ from the experimental moisture profiles, equation 4.1 is integrated with respect to x, yielding:

$$D_\theta = \frac{\int_l^{x'} \left(\frac{\partial \theta}{\partial t}\right) dx}{\left(\frac{\partial \theta}{\partial x}\right)_{x'}} \tag{4.10}$$

In this equation, use is made of the fact that the partial derivative of θ with respect to x is zero at the vapour tight bottom $(x = l)$. The resulting numerically calculated moisture diffusivities of the materials given in figure 4.7 are plotted against the corresponding moisture content in figure 4.10, except for mortar. In this figure only results are included for those regions of the material where the effects of inhomogeneities are relatively small and the situation can be regarded as isothermal. For the calculations of the derivative $\partial\theta/\partial x$

69

local averages of the experimental data were taken, to reduce the effect of fluctuations. (The numerical procedure to calculate D_θ from measured profiles is given in more detail in appendix A.3). It is obvious that the data in the figure have a significant scatter, which is rather pronounced at both high and low moisture contents. This is directly related to the accuracy by which the derivative of the moisture content with respect to position can be determined. Despite these uncertainties, the data clearly reveal a well defined variation of the moisture diffusivity with moisture content, indicating that the moisture diffusivity is not dependent upon the position. This indicates that also the moisture transport during drying in these materials can be modeled by a diffusion equation.

In the observed behaviour of the moisture diffusivity three regimes can be distinguished, which each can be related to a certain regions of the moisture profiles (see Fig. 4.7). At high moisture contents the moisture transport is dominated by liquid transport: the almost horizontal profiles correspond to a high moisture diffusivity. With decreasing moisture content the large pores will be drained and will therefore no longer contribute to liquid transport. Subsequently the moisture diffusivity will decrease. Below a so-called critical moisture content, the water in the sample no longer forms a continuous phase. Hence the moisture has to be transported by vapour and this transport will therefore be governed by the vapour pressure. For small moisture contents the moisture diffusivity starts to increase again, resulting in a minimum in the moisture diffusivity. This can be explained by noting that the contribution of the vapour transport to the moisture transport can be related to the slope $\partial\theta/\partial RH$ of the hygroscopic curve (see Fig. 4.8). Starting at 100 % relative humidity the slope decreases rapidly; a small gradient of the moisture content will involve a gradient of the vapour pressure which increases with decreasing moisture content. This will result in an increasing moisture diffusivity at low moisture contents, which regime corresponds to the almost horizontal profiles at these moisture contents. The minimum in the moisture diffusivity therefore indicates the transition from moisture transport dominated by liquid transport to moisture transport dominated by vapour transport. This transition from liquid to vapour transport corresponds to the drying front in the moisture profiles.

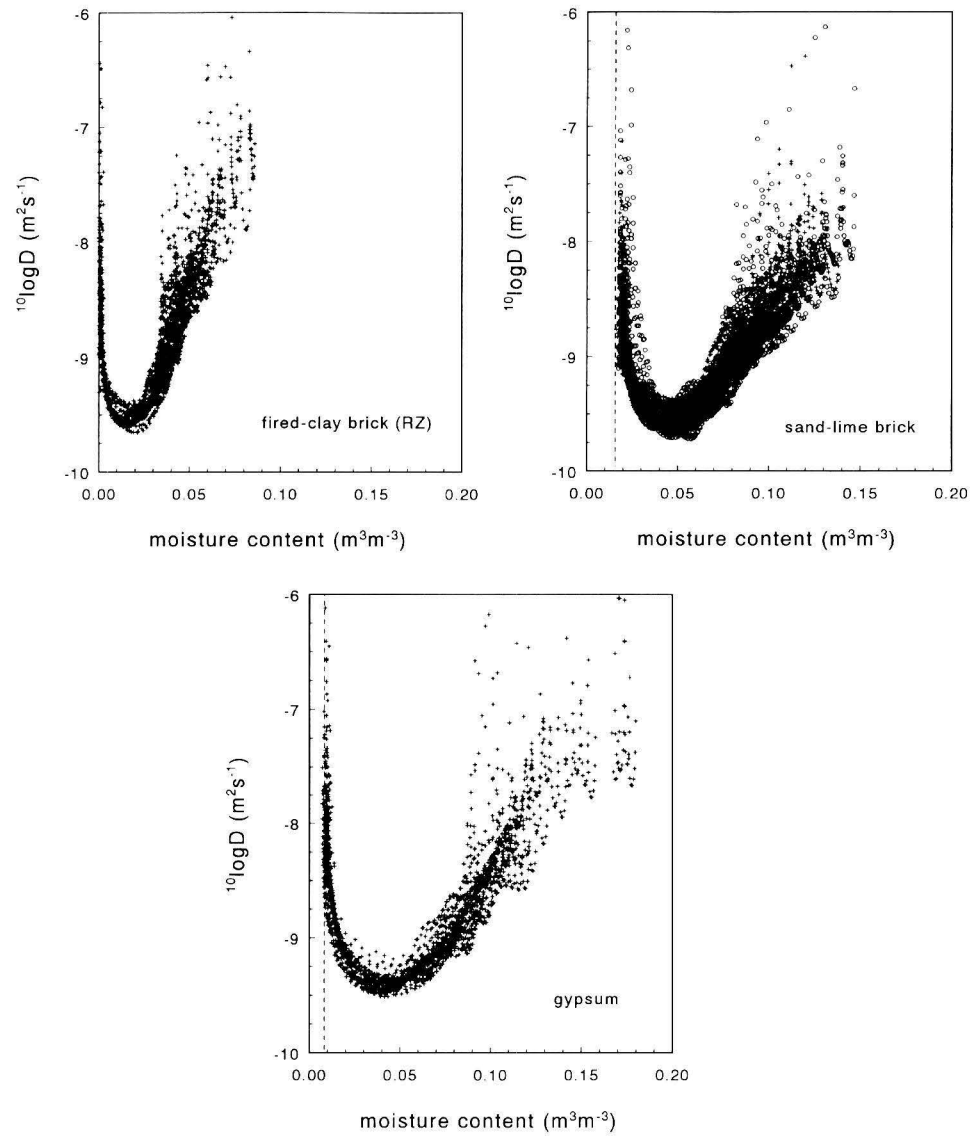*Figure 4.10 Moisture diffusivity determined from the measured moisture profiles (see Fig. 4.7) plotted against the corresponding moisture content. (+) experimental data, (○) second experiment on a different sample of the same type of material under identical conditions. The dashed line indicates the residual moisture content observed at 45% relative humidity in these drying experiments. Each figure contains over 2000 data points.*

For mortar, where the moisture profiles are rather flat and have no distinct drying front, only a rough estimate can be made of the moisture diffusivity at the minimum: $\approx 3 \times 10^{-9}$ m^{2}s^{-1}. (For mortar a moisture diffusivity was constructed which approximates the observed drying behaviour; this diffusivity is given in appendix A.5).

4.3.2 ERROR ANALYSIS

In the determination of the moisture diffusivity for drying from the measured moisture profiles, three main causes of errors can be identified: 1) the grid for scanning, 2) the one-dimensional resolution, and 3) the noise in the moisture content measurement. To investigate the effects of these errors and to check the method that was used to calculate the moisture diffusivity from the moisture profiles, computer simulations were done. First, the drying was simulated for an ideal sample, using a moisture diffusivity similar to the experimental result obtained for a brick (type RZ). These moisture profiles were computed using standard procedures from the NAG-library [NAG91]. As previously shown [PEL93], the grid for scanning the moisture profile should be as fine as possible, to enable a correct determination of the moisture diffusivity. Moisture profiles with an equally spaced grid of 0.15 mm were generated from computed ideal profiles. This grid corresponds to the one used in the NMR measurements. Using these simulated discrete moisture profiles, the moisture diffusivity was recalculated using the method discussed in the previous section. The recalculated moisture diffusivity was found to reproduce the original behaviour within 1% over the full moisture content range.

Secondly, the one-dimensional resolution was investigated. If this resolution is too low, the measured profiles will be smoothed and the extrema of the derivative of the moisture content with respect to position will be underestimated. The results of a combined error simulation involving both a 0.15 mm grid for scanning and a one-dimensional resolution of 1.0 mm (see chapter 3) are shown in figure 4.11a. The moisture diffusivity is reproduced well over the full range: only the minimum moisture diffusivity is slightly overestimated.
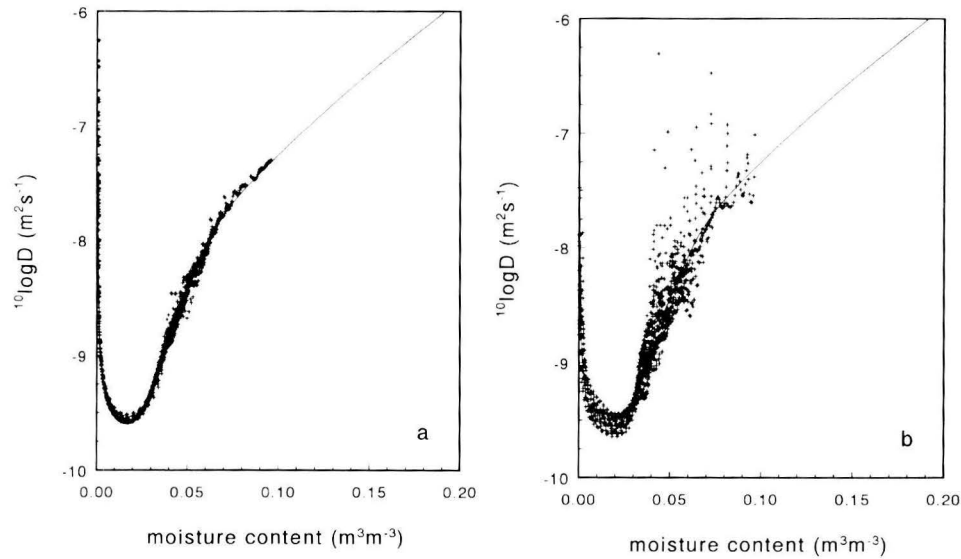
Figure 4.11 Moisture diffusivities calculated from simulated moisture profiles plotted against the corresponding moisture content; (a) for an equally spaced grid of 0.15 mm for scanning and a one-dimensional resolution of 1 mm, (b) with 2% random noise added to the simulated moisture profiles. (————) original moisture diffusivity used in the simulations, (+) moisture diffusivity calculated from the simulated profiles.

To check for the influence of noise, 2% random noise was added to the simulated moisture profiles. The results are given in figure 4.11b. The original moisture diffusivity is still rather well reproduced. Moreover, as can be seen from comparison of figure 4.11b and 4.10a, the characteristics of the experimental results are reproduced very nicely. From these simulations it can be concluded that the grid for scanning and the one-dimensional resolution in the NMR experiments had only a minor influence on the determination of the moisture diffusivity.

4.3.3 RECEDING DRYING FRONT METHOD

In order to simulate the drying of the materials under investigation, it is very important to know the moisture diffusivity at low moisture contents. As already mentioned in the previous section, in this regime the moisture transport is dominated by vapour transport, which limits the overall drying rate. However, the experimental and simulated results in figure 4.10 and 4.11, respectively, reveal that the moisture diffusivity in this range cannot be determined from measured profiles with sufficient accuracy. Therefore a new method of analysis was developed, based on the receding drying front. The velocity at which this front enters the material can be used to approximate the moisture diffusivity at low moisture contents: this diffusivity is approximated such that the receding drying front of the simulation has the same front velocity as the experimentally determined one.

To determine the velocity of the drying front, the position of this front has to be identified as a function of time. The moisture content at the minimum of the moisture diffusivity (roughly corresponding to the maximum of $\partial\theta/\partial x$, cf. Eq. 4.10) was chosen as a marker for the receding front position. In figure 4.12 the position of the front is plotted against the corresponding time for the series of data on fired-clay brick, sand-lime brick, and gypsum, given in figure 4.7. In all cases, the variation of the position with time can be approximated by a linear relation, indicating that the receding front has an almost constant velocity. In table 4.4 the front velocity for the various building materials is given. (Note that in simplified models of moisture transport, in which vapour and liquid transport are assumed to be separate processes, the position of the front is predicted to be proportional to $\sqrt{t}$ [TAM84]).
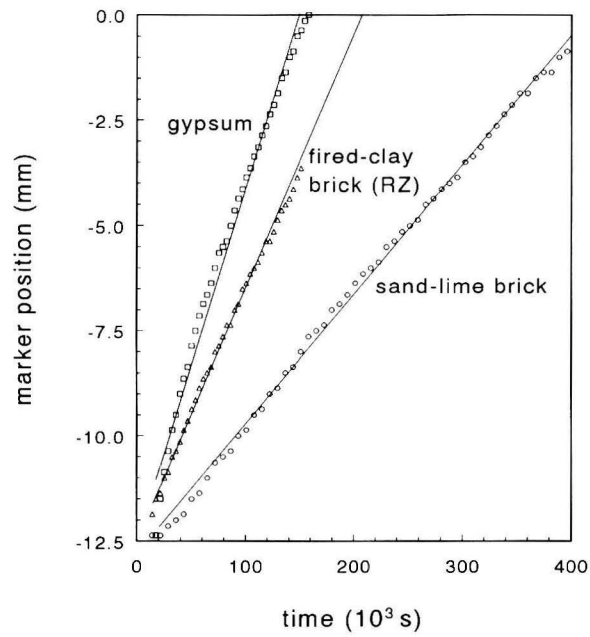
Figure 4.12 Position of the marker indicating the receding drying front plotted against the corresponding time for various materials.

type of material	front velocity (10^{-5} mm s^{-1})
fired-clay brick RZ	6.0 ± 0.4
RH	7.0 ± 0.5
GZ	7.1 ± 0.5
GH	5.1 ± 0.4
VE	5.3 ± 0.3
sand-lime brick	3.1 ± 0.4
gypsum	7.3 ± 0.4

Table 4.4 The receding front velocity in a sample of 25 mm for various building materials.

75

The velocity determined in this way is then used to approximate the moisture diffusivity at low moisture contents. To this end the moisture diffusivity in the region between the moisture content corresponding to 45% relative humidity and the point where the moisture diffusivity has roughly two times its minimum value is approximated by a straight line (see inset of Fig. 4.13). In computer simulations of the drying process the moisture diffusivity at 45% relative humidity is changed until the simulated receding front velocity is identical to the experimentally determined velocity. In addition to the diffusivity determined from drying experiments, the moisture diffusivity found from water absorption experiments was used in these simulations to model the behaviour at high moisture contents (see section 4.2), under the assumption that hysteresis can be neglected. In this respect one should note that the behaviour of the moisture diffusivity at higher moisture contents has only a minor effect on the drying rate, as already indicated above.

In figure 4.13 this procedure is illustrated. The front velocity obtained from the simulations is plotted for the three materials under investigation as a function of the value of the moisture diffusivity at 45% RH. The solid curves represent the results for the simulated front for a sample length of 25 mm, reflecting the experimental situation. (Simulations of the moisture profiles during drying for various values of the moisture diffusivity at 45% RH are also available in the form of movies; see appendix A.4 + disk). The point where such a curve intersects the corresponding experimentally determined front velocity is indicated by a black circle. The dashed curve represents the simulated front velocity for a sample of fired-clay brick with a length of 50 mm. To a fair approximation it is found that for a twice as long sample the front velocity is twice as slow (see Fig. 4.13). The open circle denotes the intersection of this curve with the observed front velocity for such a sample. The figure reveals a very nice agreement between the moisture diffusivities at 45% RH inferred from the 25 mm and 50 mm samples of fired-clay brick, suggesting that the receding drying front method is appropriate.
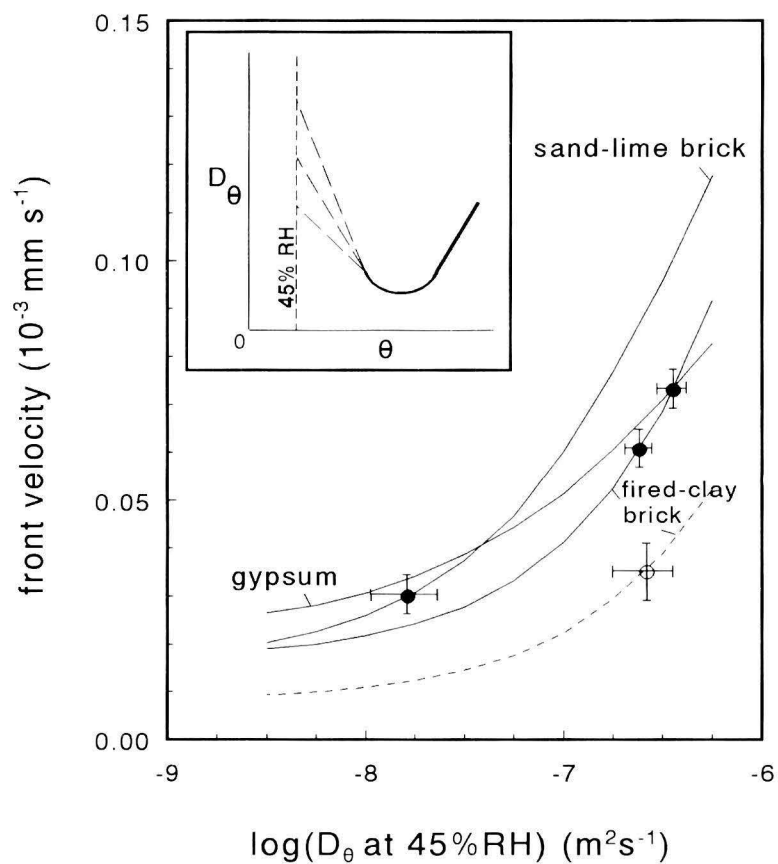
Figure 4.13 (———) calculated front velocity for various materials as a function of the moisture diffusivity assumed at 45% relative humidity (see also Fig. 4.8), for samples with a length of 25 mm. (------) calculated front velocity for a sample of fired-clay brick (RZ) with a length of 50 mm. (●, ○) front velocities determined from the experiments. The inset shows the linear approximation that was used in the computer simulations.

The moisture diffusivity for drying over the full moisture content range for the materials under investigation can be obtained by combining the moisture diffusivities found from the moisture profiles during drying (sec. 4.3.1) and during water absorption (sec. 4.2) with those obtained from the receding front method (sec. 4.3.3). The results of such an approximation are presented in figure 4.14.
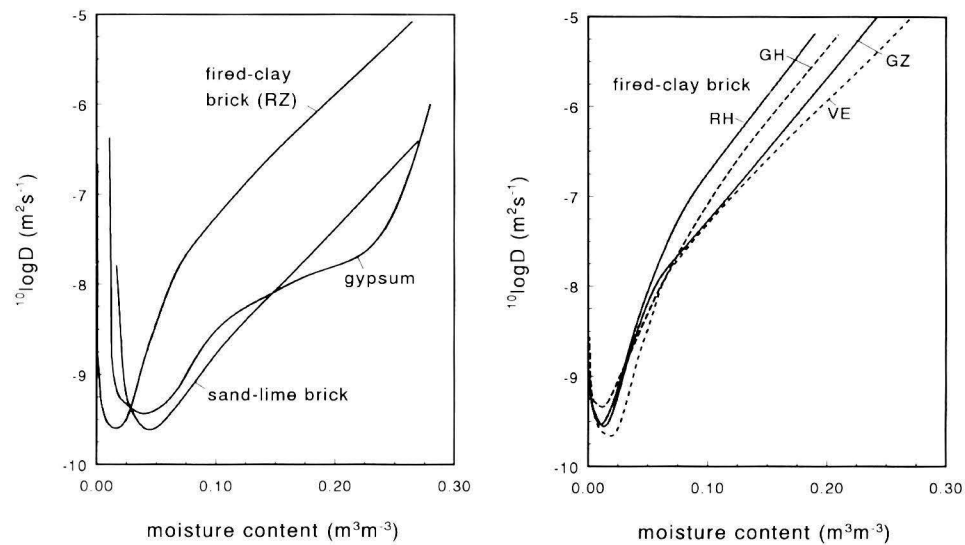
Figure 4.14 Moisture diffusivity for drying over the full moisture content range obtained by combining the moisture diffusivities determined from, successively, moisture profiles during absorption (section 4.2), during drying (section 4.3.1), and the receding front method (section 4.3.3).

Finally, in figure 4.15 illustrates a computer simulation of the drying experiment for fired-clay brick, using the behaviour of the moisture diffusivity given in figure 4.14. As expected, the simulated moisture profiles reproduce the experimental profiles given in figure 4.7a very well, except for the first few profiles, indicating that the initial drying rate is underestimated. This may be related to temperature effects.

78
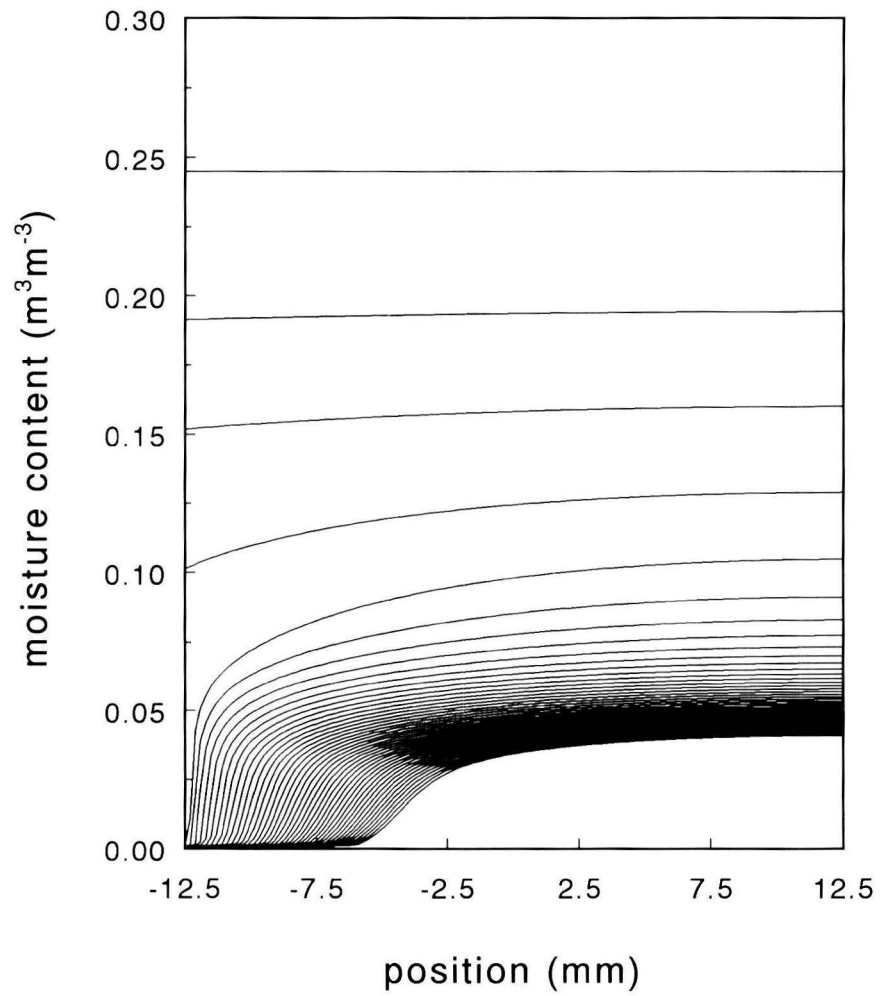
Figure 4.15. A computer simulation of the moisture profiles during drying of fired-clay brick (RZ) using the moisture diffusivity plotted in figure 4.14. The time between subsequent profiles is 1 hour and the profiles are given for a period of 48 hours.

4.4. CONCLUSIONS

The one-dimensional isothermal moisture transport observed in various porous building materials during absorption and drying can be described by a non-linear diffusion equation. The moisture diffusivity can be determined directly from measured transient moisture profiles. Nuclear magnetic resonance has been shown to be an accurate and reliable method to determine these moisture profiles. For both water absorption and drying it is found that, within the experimental accuracy, a single unambiguous relation exists between the moisture diffusivity and the moisture content, which is dependent on the type of material.

- Water absorption

It was shown that, except for gypsum, the moisture diffusivity for absorption can be approximated by a single exponential function of the moisture content (Eq. 4.7). For gypsum the moisture diffusivity can be approximated by two exponential functions, each describing the moisture diffusivity in a certain moisture content range (Eq. 4.9). Writing the moisture diffusivity in a normalized form (Eq. 4.8), it is found that for many inorganic building materials $\beta \, \theta_{cap} \approx 7.5$.

- Drying

Using the developed NMR equipment with high spatial resolution, measurements could be performed on smaller samples than those that are generally used. Hence a strong reduction in the time needed to determine the moisture diffusivity could be achieved. (In the literature experiments are reported on samples of over 100 mm, with subsequent longer measurement times, i.e., in the order of 8 to 72 days [KOO71, CRA83]).

From error analysis it was shown the grid for scanning and the one-dimensional resolution had only a minor influence on the determination of the moisture diffusivity for drying. The error in the calculation of the moisture diffusivity was dominated by experimental noise and inhomogeneities in the porosity of the material.

The velocity of the receding drying front was found to be constant. Using the experimentally observed velocity of this receding front, the moisture diffusivity can be approximated in such a way that it correctly models the moisture profiles during drying.

5 | MOISTURE TRANSPORT AT THE BRICK/MORTAR INTERFACE

5.1 INTRODUCTION

In the previous chapter attention was given to the moisture transport in various building materials separately. In masonry, however, brick and mortar are bonded. This bonding is essential to its structural behaviour. Much research has been focused on the bonding process and the parameters influencing the mechanical behaviour of this bonding. An extensive literature review can be found in GRO93. On the other hand, almost no research has been reported on moisture transport across the brick/mortar interface. Often it is assumed that a perfect hydraulic contact exists between mortar and brick (e.g., GAR92), so the suction is constant over the boundary (Eq. 2.34). In order to verify this assumption, preliminary absorption experiments were performed on brick/mortar samples. The samples were cylindrical bars with a diameter of 20 mm and were made up of fired-clay brick, in length ranging between 70 and 110 mm, and 45 mm of mortar. The samples therefore do not reflect the mortar joints in practice, which have a thickness of the order of 20 mm. A larger mortar 'joint' was chosen because of experimental limitations and to enable the observation of a possible change of the mortar due to the bonding process. The samples were made of the same type of fired-clay brick and mortar as used in the previous chapter. For each type of brick two samples were made, using mortar with (MM) and without (MZ) air-entraining agent. More details of the sample preparation are given in appendix A.2.

5.2 WATER ABSORPTION

The water absorption experiments were performed using the same experimental set-up and procedure as outlined in section 4.2: Each wetting moisture profile consists of small partial profiles, each measured at a different position and time. After an entire moisture profile is

scanned, a next profile is scanned, and so on.

The water absorption of each sample was measured from brick to mortar and the opposite, from mortar to brick. No significant differences were observed in the transport near the interface for the various types of fired-clay brick. Therefore in figure 5.1 and 5.2 some typical profiles for water absorption from brick to mortar and from mortar to brick are presented for the two types of mortar, i.e., mortar with and without air-entraining agent. (These measured profiles are also available in the form of movies; see appendix A.4 + disk)

These figures reveal that the water absorption of the two types of bonded mortar is largely different from water absorption of mortar samples hardened separately (see section 4.2), especially for the mortar with air-entraining agent. For both types of mortar it is found that the profiles no longer collapse on a single curve after Boltzmann transformation, indicating that the moisture diffusivity is dependent upon the position. It was estimated from the experimental data, that for both types of mortar the water penetration coefficient decreases towards the mortar/brick interface by a factor of 2 to 4. This variation of the hygric properties with position is probably caused by suction of water out of the mortar into the brick during the bonding process. As a result, particles will be transported to the mortar/brick interface and the mortar becomes more compact near the interface [GRO93, AND42].

However, for the mortar with air-entraining agent it is observed that both for water absorption from brick to mortar and from mortar to brick, almost no water is transported across the interface. It seems that near the interface either an almost impermeable layer is formed or that the hydraulic contact is bad, resulting in a large jump in suction.

In the case of mortar without air-entraining agent moisture transport across the interface is observed. Because of the relatively large moisture diffusivity of the brick in comparison to that of the mortar, two situations can be distinguished. In the case of absorption from brick to mortar, moisture profiles start to develop in the mortar when the water reaches the interface. Since the mortar absorbs water rather slowly, the brick is quickly saturated up to its capillary moisture content. In the case of absorption from mortar to brick, the water is quickly absorbed by the brick when it reaches the interface, and after a few hours an

82

Figure 5.1 Moisture profiles measured during the absorption of water in a sample of fired-clay brick (GH) and mortar without air-entraining agent (MZ). The profiles are composed of partial profiles each measured at different position and time. The experiment lasted 6 hours in the case of absorption from brick to mortar (a) and 24 hours in the case of absorption from mortar to brick (b). The shaded box indicates the interface area and the dashed line indicates the end of the sample. In figure a 22 profiles are plotted; after the first 10 profiles the time between subsequent profiles is in the order of 20 min. In figure b 34 profiles are plotted; after the first 10 profiles the time between subsequent profiles is in the order of 45 min.

83

Figure 5.2 Moisture profiles measured during the absorption of water in a sample of fired-clay brick (GZ) and mortar with air-entraining agent (MM). The experiment lasted 14 hours in the case of absorption from brick to mortar (a) and 20 hours in the case of absorption from mortar to brick (b). The shaded box indicates the interface area and the dashed line indicates the end of the sample. In figure a 59 profiles are plotted; after the first 10 profiles the time between subsequent profiles is in the order of 15 min. In figure b 56 profiles are plotted; after the first 15 profiles the time between subsequent profiles is in the order of 20 min

almost stationary moisture profile develops in the mortar. (Both phenomena can also be seen in computer simulations of an idealized situation, as given in appendix A.6).

If, as suggested, a perfect hydraulic contact would exists between brick and mortar, each of the materials should also absorb moisture up to its capillary moisture content, if the other material was saturated up to its capillary moisture content. However, in the case of brick/mortar it appears that the moisture content of the mortar near the boundary does not reach its capillary moisture content, i.e., ≈ 0.20 m^{3}m^{-3} (see the water absorption experiment from mortar to brick). Similar to the case of mortar with air-entraining agent, it is not clear whether this is due to a jump in suction or to a small layer at the brick-mortar surface which has become less permeable to moisture flow. Hence additional experiments were performed on the same samples with a reduced amount of mortar, i.e., half of the mortar was cut off. In figure 5.3 a typical result is given. (These measured profiles are also available in the form of movies; see appendix A.4 + disk).
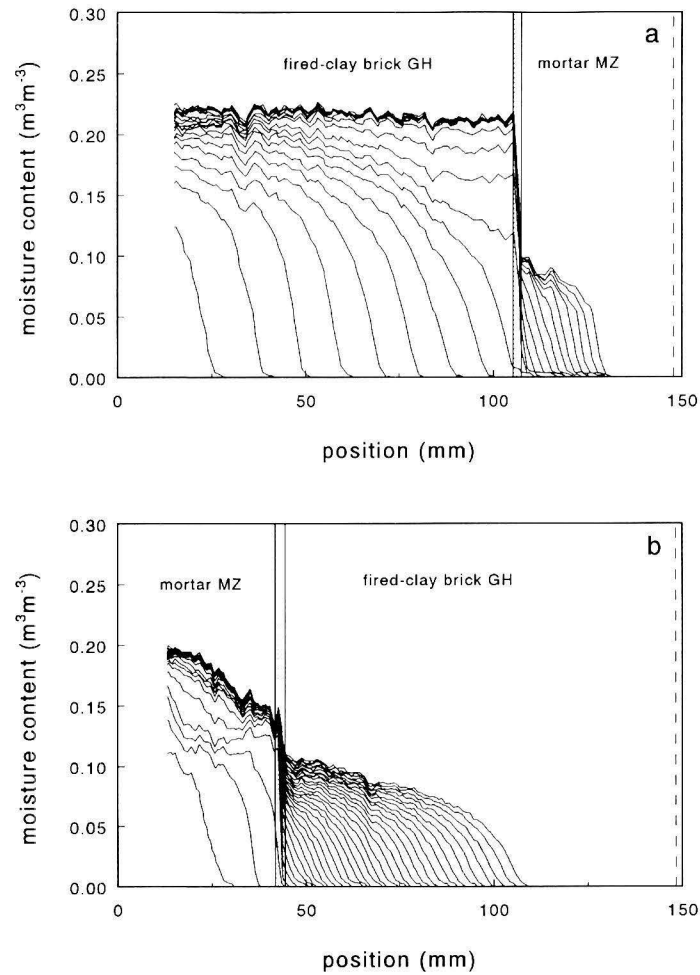

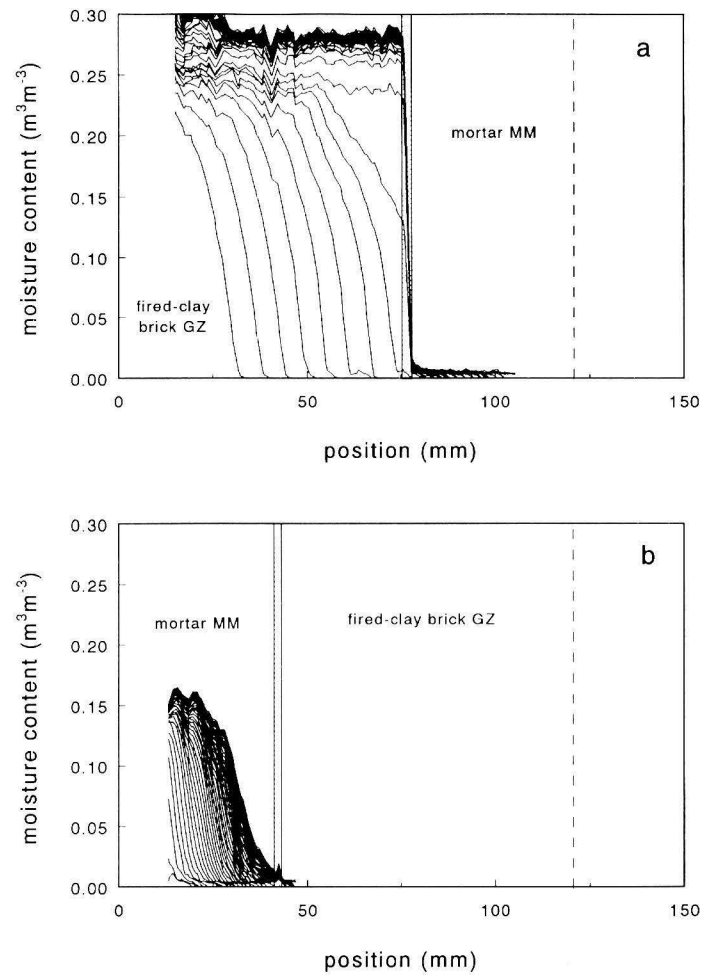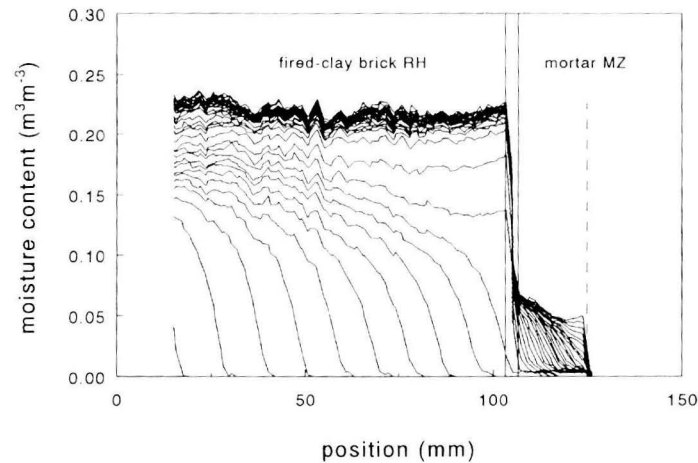*Figure 5.3 Moisture profiles measured during the absorption of water in a sample of fired-clay brick (RH) and mortar without air-entraining agent (MZ). The experiment lasted 22 hours. The shaded box indicates the interface area and the dashed line indicates the end of the sample. 37 profiles are plotted; after the first 15 profiles the time between subsequent profiles is in the order of 40 min.*

85

In this case, it is observed that, when the moisture reaches the end of the mortar the moisture profiles become flat. However, the mortar does still not saturate up to its capillary moisture content. These results suggest that there is no perfect hydraulic contact between the two components brick and mortar, and suggest a jump in suction over the brick/mortar interface. Of course, experiments over a more extended period of time have to be performed to verify this point.

Additional information might be achieved from the suction curves of the individual materials. However, due to experimental problems, the mortar suctions were not obtained. The suction curves for the bricks are given in appendix A.1.

5.3 CONCLUSIONS

During the bonding process with brick, the hygric properties of mortar change significantly compared to mortar samples hardened separately, especially in the case of mortar with air-entraining agent. Preliminary measurements indicate that there is no perfect hydraulic contact between mortar and brick, and suggest a jump in suction across the brick/mortar interface. Due to the limited number of experiments, no satisfactory explanation can be given for the observed phenomena and more research on this subject is needed.

6 | CONCLUSIONS AND SUGGESTIONS

In this chapter the main conclusions of each chapter will be summarized and some suggestions for future research will be given.

- Chapter 2: Theory

The isothermal moisture transport in porous media can be described fairly well by a non-linear diffusion equation. Here all mechanisms for moisture transport, i.e., liquid flow and vapour diffusion (with associated enhancement mechanisms) are combined into a single moisture diffusivity which is dependent on the actual moisture content.

More theoretical investigations are needed to establish a relation between the microstructure (e.g., pore distribution) and the macroscopic diffusion coefficients for liquid and vapour transport. This could give more insight into the variation of the moisture diffusivity for various types of building material.

- Chapter 3: Moisture measurement

With both NMR and neutron radiography the moisture content can be determined quantitatively, one-dimensionally, and in a non-destructive way. Unlike neutron transmission, the signal obtained by NMR is directly related to the amount of hydrogen nuclei in the selected region of a sample.

In the NMR equipment, developed for the measurements presented in this thesis, the signal is obtained by straightforward Hahn sequences $(90_x - \tau - 180_{\pm x})$. If Carr-Purcell-Meiboom-Gill sequences $(90_x - \tau - 180_x - 2\tau - 180_x - \ldots)$ are used, the moisture content and the spin-spin relaxation time (T_2) can be measured simultaneously. So apart from a moisture profile, also the corresponding T_2 distribution may be obtained.

In principle, the variation of T_2 can be related to various pore sizes in which the liquid water is present. This additional information may be used to verify the vapour enhancement mechanisms: liquid islands and surface diffusion. It may also be used to study the

change of the structure of the mortar due to particle transport during the initial bonding process. This additional information can, however, only be obtained for materials with a low concentration of magnetic impurities.

Extension of the NMR equipment with additional gradient coils will offer the possibility to determine two dimensional moisture distributions and thereby the possibility to verify two dimensional models of moisture transport (e.g., moisture distribution in brick/mortar samples during water absorption and drying).

- Chapter 4: Determination of the moisture diffusivity

It was shown that, the moisture diffusivity can be determined directly from transient moisture profiles during absorption and drying. For both water absorption and drying it is found that within the experimental accuracy, a single unambiguous relation exists between the moisture diffusivity and the actual moisture content, which is dependent on the type of material.

- Water absorption

The moisture diffusivity for absorption can be approximated by a single exponential function of moisture content for the building materials considered in this thesis, except for gypsum.

Writing the moisture diffusivity in a normalized form it appears that for many inorganic building materials $\beta \theta_{cap} \approx 7.5$. This relation has to be checked for more inorganic building materials, and also a more theoretical basis is needed to establish its validity (e.g., under which conditions).

Assuming $\beta \theta_{cap} = 7.5$ for an inorganic porous material, the moisture diffusivity is then given by:

$$D_\theta = D_o \exp\left[7.5 \left(\frac{\theta}{\theta_{cap}} \right) \right]$$
(6.1)

If the capillary moisture content and either the water absorption coefficient, A, or the water penetration coefficient, B, of a material are known, D_o can be calculated [BRU79]. Hence, based on coefficients which can be determined by simple experiments, a first

88

approximation can be made of the moisture diffusivity, which may be very useful for engineering applications.

- Drying

The error in the calculation of the moisture diffusivity was dominated by experimental noise and inhomogeneities in the porosity of the materials. The velocity of the receding drying front was found to depend on the length of the sample, but appeared to be constant within the experimental accuracy. Using this observed velocity the moisture diffusivity can be approximated in such a way that it correctly models the profiles during drying.

It is surprising that, also in the region where the moisture transport is assumed to be dominated by vapour transport, the experimental results can be modeled by a non-linear diffusion equation, since in chapter 2 this modeling was obtained by assuming $\theta_l > 10^{-3}$.

In the experiments reported in this thesis the samples where dried at a fixed relative humidity of 45%. If the same sample is dried at different fixed relative humidities, more information can be obtained about the behaviour of the moisture diffusivity at low moisture contents. In addition, more experiments have to be performed on samples of different length to verify, the relation between the length of a sample and the receding drying front velocity.

The drying experiments can be performed at different temperatures. Comparison of these moisture diffusivities may give insight into the contribution of the various transport mechanisms, since these mechanisms have a different temperature dependency.

Using independent vapour permeability measurements in combination with the hygroscopic curve, the moisture diffusivity at low moisture contents can be determined. These results can be used to validate or modify the linear approximation of the moisture diffusivity at low moisture contents as assumed in the receding front method.

- Chapter 5: Moisture transport at the brick/mortar interface

During the bonding process with brick, the hygric properties of mortar change significantly compared to mortar hardened separately. Preliminary absorption measurements on brick/mortar samples indicate that there is no perfect hydraulic contact between mortar and

89

brick and suggest a jump in suction.

As indicated above, NMR can be used to provide information on the change of the mortar due to particle transport during the bonding process. Microscopy of hardened samples can also give insight into this particle transport. Moreover, it can give information on the contact between mortar and brick.

As already indicated in chapter 5, the absorption experiments have to performed over more extended periods of time (of the order of weeks to months). The drying process of saturated brick/mortar samples has to be studied also, to see whether the moisture transport across the interface shows the same phenomena as during absorption.

- General remarks

The results of the present study can be used to describe and simulate the water absorption and drying of individual inorganic porous building materials. For simulation of masonry and associated problems in practice at least a two dimensional model of the moisture transport is needed. It is therefore necessary to model the moisture transport across the interface. As already indicated above, more research will be needed for this purpose.

In the present study effects of hysteresis, temperature, and contaminants were not taken into account. The influence of these factors has to be considered, before a realistic model of moisture transport in practice can be obtained. In addition, the present study was limited to isotropic materials. In practice, however, many durability problems are related to anisotropic materials, e.g., extruded fired-clay brick, in which the modeling of the moisture transport is much more complicated. These materials may be the subject of future studies.

REFERENCES

[ADA67]   A.W. Adamson, *Physical chemistry of surfaces*, Wiley, New York, USA (1967).

[ANA91]   Analog Devices, One Technology Way, P.O Box 9106, Norwood, MA 02062, USA (1991).

[AND42]   F.O. Anderegg, The effect of brick absorption characteristics upon mortar properties, *ASTM-Proc.* **42**, 821-836 (1942).

[AND61]   W.A. Anderson, Electrical current shims for correcting magnetic fields, *Rev. Sci. Inst.* **32**, 241-250 (1961).

[ANZ91]   ANZAC, 80 Cambridge Street, Burlington, Mass. 01803, USA (1991).

[AVA91]   Avance et Développement Electronique (ADE), 2 bis, rue Léon Blum -Z.I.- 91120 Palaiseau, France (1991).

[BEA87]   J. Bear and Y. Bachmat, Advective and diffusive fluxes in porous media, *Advances in transport phenomena in porous media (edited by J. Bear and M. Yavuz Corapcioglu*, Martinus Nijhoff, Dordrecht, the Netherlands (1987).

[BEA90]   J. Bear and Y. Bachmat, *Introduction to modeling of transport phenomena in porous media*, Vol. 4, Kluwer, Dordrecht, the Netherlands (1990).

[BEK92]   P.C.F. Bekker, Durability engineering methodology based on stress cycles and hazard characteristics, *Int. workshop Durability of Masonry (edited by L. Binda and P.C.F Bekker), Milan, Italy,* 55-144 (1992).

[BER73]   D. Berger and D.C.T. Pei, Drying of hygroscopic capillary porous solids, *Int. J. Heat Mass Transfer* **16**, 293-302 (1973).

[BRO79]   K.R. Brownstein and C.E. Tarr, Importance of classical diffusion in NMR studies of water in biological cells, *Phys. Rev. A* **19**, 2446-2453 (1979).

[BRU79]   W. Brutsaert, Universal constants for scaling the exponential soil water diffusivity?, *Water Resources Res.* **15**, 481-483 (1979).

[CAR93]   T.A. Carpenter, E.S. Davies, C. Hall, L.D. Hall, W.D. Hoff and M.A.Wilson, Capillary water migration in rock: process and material properties examined by NMR imaging, *Materials and Structures* **26**, 286-292 (1993).

91

[[CHE89] Peischi Chen and D.C.T. Pei, A mathematical model of drying processes, *Int. J. Heat Mass Transfer* **32**, 297-310 (1989).

[CLA87] T. Claiborne, J.T. Cheng, A.R. Garber, and P.D. Ellis, Wide-band solids, rapid recovery, multinuclear transceiver/digitizer for high-resolution NMR spectrometer, *Rev. Sci. Instr.* **58**, 742 (1987).

[CRA83] P. Crausse, *Etude fondamentale des transferts couplés de chaleur et d'humidité en milieu poreux non saturé*, Ph.D. thesis, L'institut national polytechnique de Toulouse, France (1983).

[CUR93] *Duurzaamheid van baksteenmetselwerk*, rapport 165, CUR, the Netherlands, (1993).

[DAR56] H.P.G. Darcy, *Les fontaines publiques de la ville du Dijon*, Delmont, Paris, France (1856).

[DAV63] J.M. Davidson, J.W. Biggar and D.R. Nielsen, Gamma ray attenuation for measuring bulk density and transient water flow in porous materials, *J. Geophys. Res.* **68**, 4777 (1963).

[DIX82] R.L. Dixon and K.E. Ekstrand, The physics of proton NMR, *Med. Phys.* **9**, 807-818 (1982).

[EDF43] N.E. Edlefsen and A.B.C Anderson, The thermodynamics of soil moisture, *Hilgardia* **15**, 31-299 (1943).

[FOR91] E.J. Fordham, T.P.L. Roberts, T.A. Carpenter and L.D. Hall, Nuclear magnetic resonance imaging of simulated voids in cement slurries, *AIChE Journal* **37**, 1895-1899 (1991).

[GAR58] W.R. Gardner and M.S. Mayhugh, Solutions and tests of the diffusion equation for the movement of water in soil, *Soil. Sci. Soc. Am. Proc.* **22**, 197-201 (1958).

[GRO93] C. Groot, *Effect of water on mortar-brick bond*, Ph.D. thesis, Delft University of Technology, the Netherlands (1993).

[GUI89] G. Guillot, A. Trokiner, L. Darrasse and H. Saint-Jalmes, Drying of a porous rock monitored by NMR imaging, *J. Phys. D* **22**, 1646-1649 (1989).

[GUM79] R.J. Gummerson, C. Hall, W.D. Hoff, R. Hawkes, G.N. Holland and W.S. Moore, Unsaturated water flow within porous materials observed by NMR imaging, *Nature* **281**, 56-57 (1979).

[HAH50] E.L. Hahn, Spin echoes, *Phys. Rev.* **80**, 580-594 (1950).

[IEA91] *Catalogue of Material Properties*, Report Annex XIV, Vol 3, International Energy Agency (1991).

[ILL52] W. Illig, Die Größe der Wasserdampfübergangszahl bei Diffusionsvorgängen in Wänden von Wohnungen, Stallungen und Kühlräumen, *Gesundheits Ingenieur* **7/8**, 124-127 (1952).

[KAL81] A.N. Kalimeris, *Water flow processes in porous building materials*, Ph.D. thesis, University of Manchester, U.K. (1984).

[KET92] A.A.J. Ketelaars, *Drying deformable media*, Ph.D. thesis, Eindhoven University of Technology, the Netherlands (1992).

[KLE90] R.L. Kleinberg and M.A. Horsfield, Transverse relaxation processes in porous sedimentary rock, *J. Magn. Reson.* **88**, 9-19 (1990).

[KLE93] R.L. Kleinberg and S.A. Farooqui, T_1/T_2 ratio and frequency dependence of NMR relaxation in porous sedimentary rocks, *J. Colloid Interface Sci.* **158**, 195-198 (1993).

[KOO71] J. van der Kooi, *Moisture transport in cellular concrete roofs*, Ph.D. thesis, Eindhoven University of Technology, the Netherlands (1971).

[KRU89] M. Krus and K. Kießl, Kapillartransportkoeffizienten von Baustoffen aus NMR-Messungen, *IBP Mitteilung Fraunhofer-Institut für Bauphysik* **16**, Germany (1989).

[LAN88] V. McLane, C.L. Dunford and P.F. Rose, *Neutron cross sections*, Vol. 4, Academic Press London, U.K. (1988).

[LUI66] A.V. Luikov, *Heat and mass transfer in capillary porous bodies*, Pergamon Press, Oxford, U.K. (1966).

[MAC91] M/A-COM Silicon Products, inc, One South Avenue, Burlington, MA 01803, USA (1991).

[MIN91] Mini-Circuits, P.O. Box 350166, Brooklyn, New York 11235, USA (1991).

[MUA73] Y. Mualem, Modified approach to capillary hysteresis based on a similarity hypothesis. *Water Resources Res.* **9**, 1324-1331 (1973).

[MUA74] Y. Mualem, A conceptual model of hysteresis, *Water Resources Res.* **10**, 514-520 (1974).

[NAG91] The NAG Numerical Fortran Library, Mark 15, NAG Ltd, Wilkinson House, Jordan Hill Road, Oxford, U.K. (1991).

[OKA81] M. Okazaki, H. Tamon and R. Toei, Interpretation of surface flow phenomenon of adsorbed gases by hopping model, *AIChE Journal* **27**, 262-270 (1981).

[OSM90] P.A. Osment, K.J. Packer, M.J. Taylor, J.J. Attard, T.A. Carpenter, L.D. Hall, N.J. Herrod and S.J. Doran, NMR imaging of fluids in porous solids, *Phil. Trans. R. Soc. Lond. A* **333**, 441-452 (1990).

[PEL93] L. Pel, A.A.J. Ketelaars, O.C.G. Adan and A.A. van Well, Determination of moisture diffusivity in porous media using scanning neutron radiography, *Int. J. Heat Mass Transfer* **36**, 1261-1267 (1993).

[PHI57] J.R. Philip and D.A. de Vries, Moisture movement in porous materials under temperature gradients, *Trans. Am. Geophys. Un.* **38**, 222-232 (1957).

[PHI91] Philips Components Division, Strategic Accounts and International Sales, P.O. Box 218, 5600 MD Eindhoven, the Netherlands (1991).

[ROW71] R.L. Rowell, S.A. Carrano, A.J. de Bethune and A.P. Malinauskas, Gas and vapor permeability: surface flow through porous media, *J. of Colloid Interface Sci.* **37**, 242-246 (1971).

[SLA81] J.C. Slattery, *Momentum, energy and mass transfer in continua*, Krieger, New York, USA (1981).

[SMU94] H. Smulders, L. Pel, P. van de Ende and A.W.B Theuws, Het meten van het vochttransport door baksteen en mortel met neutronenradiografie, *Materialen* **5**, 41-44 (1994).

[STA86] M.A. Stanisch, G.S. Schajer and F. Kayihan, A mathematical model for drying of hygroscopic porous media, *AIChE Journal* **32**, 1301-1311 (1986).

[SYN91] Synergy Microwave Corporation, 483 Mc Lean Boulevard, Paterson, New Jersey 07504, USA (1991).

[TAM84] E. Tammes and B.H. Vos, *Warmte en vochttransport in bouwconstructies*, Kluwer, Deventer, the Netherlands (1984).

[VRI58] D.A. de Vries, Simultaneous transfer of heat and moisture in porous media, *Trans. Am. Geophys. Un.* **39**, 909-916 (1957).

[WHI77] S. Whitaker, Simultaneous heat, mass and momentum transfer in porous media: A theory of drying porous media, *Adv. Heat Transfer* **13**, 119-200 (1977).

LIST OF SYMBOLS

A	water absorption coefficient	$(kg\ m^{-2}\ s^{-1/2})$
B	water penetration coefficient	$(m\ s^{-1/2})$
B	magnetic flux density	(T)
B_0	externally applied magnetic flux density	(T)
C	capacity	(F)
D_0	constant	$(m^2\ s^{-1})$
D_v	water vapour diffusivity in air	$(m^2\ s^{-1})$
D_0	isothermal moisture diffusivity	$(m^2\ s^{-1})$
$D_{0,l}$	isothermal liquid diffusivity	$(m^2\ s^{-1})$
$D_{0,v}$	isothermal vapour diffusivity	$(m^2\ s^{-1})$
$D_{0,v}^F$	isothermal vapour diffusivity (only diffusion)	$(m^2\ s^{-1})$
d	thickness of sample	(m)
$E_{l \to v}$	evaporation rate	(s^{-1})
$E_{v \to l}$	condensation rate	(s^{-1})
F	noise figure	(dB)
f	frequency	(Hz)
f_c	RF center frequency	(Hz)
f_0	NMR resonance frequency in a static field	(Hz)
g	acceleration due to gravity	$(m\ s^{-2})$
h	relative humidity	$(\%)$
h_a	relative humidity of the air	$(\%)$
h_m	macroscopic relative humidity of the material	$(\%)$
H	magnetic field strength	$(A\ m^{-1})$
I	intensity of neutron beam	$(m^{-2}\ s^{-1})$
I_0	initial intensity of neutron beam	$(m^{-2}\ s^{-1})$
K	hydraulic conductivity	$(m\ s^{-1})$
k_l	permeability of liquid water (saturated)	(m^2)

$k_l(\theta)$	effective permeability of liquid water	(m^2)
L	inductance	(H)
l	height of the sample	(m)
M	molar mass of water	$(kg\ mol^{-1})$
M	magnetization	$(emu\ gram^{-1})$
n	unit vector	(-)
n	porosity	$(m^3\ m^{-3})$
n_{eff}	effective porosity	$(m^3\ m^{-3})$
p	macroscopic pressure	$(N\ m^{-2})$
p_a	macroscopic air pressure	$(N\ m^{-2})$
$p_c{}'$	microscopic capillary pressure	$(N\ m^{-2})$
p_c	macroscopic capillary pressure	$(N\ m^{-2})$
$p_v{}'$	microscopic vapour pressure	$(N\ m^{-2})$
p_v	macroscopic vapour pressure	$(N\ m^{-2})$
p_{vs}	saturated vapour pressure	$(N\ m^{-2})$
p_w	macroscopic water pressure	$(N\ m^{-2})$
q_l	volumetric liquid water flux	$(m\ s^{-1})$
q_v	volumetric vapour flux	$(m\ s^{-1})$
R	gas constant	$(J\ mol^{-1}\ K^{-1})$
S	signal	(-)
r	resistance	(Ω)
r	microscopic radius of curved water/air surface	(m)
T	temperature	(K)
T_1	spin-lattice relaxation time	(s)
T_2	spin-spin relaxation time	(s)
T_2^*	FID relaxation time in a homogeneous field	(s)
T^*	tortuosity	(-)
T_{90^o}	duration 90° pulse of Hahn sequence	(μs)
TE	spin-echo time	(s)
TR	repetition time of the spin-echo experiments	(s)

t	time	(s)
V_r	volume of REV	(m³)
$V_{r,m}$	volume of multiple interconnected pores within REV	(m³)
$V_{r,d}$	volume of dead-end pores within REV	(m³)
$V_{r,\alpha}$	volume of component α within REV	(m³)
x	spatial coordinate	(m)
z	vertical spatial coordinate	(m)

Greek symbols

α_{LI}	vapour diffusion enhancement factor by liquid islands	(-)
α_{SD}	vapour diffusion enhancement factor by surface diffusion	(-)
β	mass transfer coefficient	(s m⁻¹)
β	constant	(-)
$\gamma/2\pi$	gyromagnetic ratio	(MHz T⁻¹)
$\gamma_{w,a}$	interfacial tension between water and air	(N m⁻¹)
θ	moisture content	(m³ m⁻³)
θ_a	air content	(m³ m⁻³)
θ_b	bound water content	(m³ m⁻³)
θ_{cap}	capillary moisture content	(m³ m⁻³)
θ_l	liquid water content	(m³ m⁻³)
θ_o	initial moisture content	(m³ m⁻³)
θ_v	water vapour content	(m³ m⁻³)
θ_α	volumetric content of phase α	(m³ m⁻³)
λ	= x t⁻¹ᐟ² ; Boltzmann transformation	(m s⁻¹ᐟ²)
μ_i	macroscopic attenuation coefficient of component i	(m⁻¹)
μ_l	dynamic viscosity of liquid water	(kg m⁻¹ s⁻¹)
μ_{mat}	macroscopic attenuation coefficient of dry material	(m⁻¹)
μ_w	macroscopic attenuation coefficient of water	(m⁻¹)

97

ρ	proton density	(m^{-3})
ρ	mass density	$(kg\ m^{-3})$
ρ_l	mass density of liquid water	$(kg\ m^{-3})$
ρ_v	mass density of water vapour	$(kg\ m^{-3})$
τ	time between pulses of Hahn sequence	(s)
χ	magnetic susceptibility	$(emu\ Gs^{-1}gram^{-1})$
Ψ	suction	(m)

SUMMARY

Moisture plays a dominant role in various deterioration mechanisms of building materials, e.g., frost damage or salt crystallization. In the case of masonry, this deterioration may reveal itself in various forms, e.g., decolouring of the surface, cracking and chipping, or disintegration of brick and/or mortar. A detailed knowledge of the moisture transport is essential for understanding the durability, which in this respect may be regarded as the resistance of a material or construction against deterioration caused by attacks from its environment. In this thesis the isothermal moisture transport in various porous building materials, i.e., fired-clay brick, sand-lime brick, mortar, and gypsum plaster, is discussed.

The isothermal macroscopic moisture transport in porous materials can be described fairly well by a non-linear diffusion equation. In this diffusion model, all mechanisms for moisture transport, i.e., liquid flow and vapour diffusion (with the associated enhancement mechanisms), are combined into a single moisture diffusivity which is dependent on the actual moisture content.

In principle, the moisture diffusivity can be determined directly from measured transient moisture profiles. With Nuclear Magnetic Resonance (NMR) techniques, which yield an output signal, that is proportional to the amount of hydrogen nuclei in a certain selected region of the material, the moisture profiles can be determined non-destructively. Because of the large amount of paramagnetic ions present in many porous building materials, the hydrogen nuclei in these materials exhibit very short transverse relaxation times and a broad resonance linewidth. Therefore specialized NMR equipment was developed, which enables the measurement of the moisture profiles in these types of materials with a one-dimensional resolution of 1 mm and an absolute accuracy of a few percent.

Using this NMR equipment the moisture profiles are determined during water absorption and drying. For both of these processes it is found that, within the experimental accuracy, a single unambiguous relation exists between the moisture diffusivity and the actual moisture content, which is dependent on the type of material.

For the porous building materials discussed in this thesis, except for gypsum, it is found

that the moisture diffusivity for absorption can be approximated by a single exponential function of the moisture content.

It is shown that the limited number of discrete positions at which the moisture profiles are scanned and the one-dimensional resolution of the NMR equipment have only a minor influence on the determination of the moisture diffusivity for drying. The error in the calculation of the moisture diffusivity is dominated by experimental noise and inhomogeneities in the porosity of the materials under investigation. In the drying experiments, it is observed that after some time, a receding drying front develops that moves through the material with constant velocity. In this stage of the drying process the moisture transport is dominated by vapour transport, which limits the overall drying rate. A new so-called receding front method is developed that uses the constant velocity of the drying front to model the isothermal moisture transport at low moisture constants.

In masonry brick and mortar are bonded, and these will therefore interact. Hence attention is given to the moisture transport across the brick/mortar interface. It is found that during the bonding process the hygric properties of the mortar change significantly compared to mortar hardened independently. Preliminary absorption experiments using brick/mortar samples indicate that there is no perfect hydraulic contact, and suggest a jump in suction across the interface. Due to the limited number of experiments in the latter study no satisfactory explanation can be given yet for the moisture transport phenomena observed near the brick/mortar interface.

SAMENVATTING

Vocht speelt een dominante rol in talrijke schademechanismen bij bouwmaterialen. Voorbeelden hiervan zijn vorstschade en schade door zoutkristallisatie. Deze schade komt bijvoorbeeld bij metselwerk tot uitdrukking in verkleuring van het oppervlak, scheurvorming en afschilfering, of desintegratie van baksteen en/of mortel.

De beschrijving van het vochttransport is van belang om een beter begrip van de duurzaamheid te kunnen krijgen. Hierbij kan de duurzaamheid worden gezien als de weerstand van een materiaal of constructie tegen aanvalsmechanismen vanuit zijn omgeving. In dit proefschrift wordt het isotherme vochttransport in verschillende poreuze bouwmaterialen, te weten baksteen, kalkzandsteen, mortel en gipspleister, besproken.

Het macroscopische isotherme vochttransport in poreuze materialen kan redelijk nauwkeurig worden beschreven met een niet-lineaire diffusie vergelijking. In dit diffusie model zijn alle transportmechanismen voor het vochttransport, zoals vloeistofstroming en dampdiffusie (met interactiemechanismen voor versnelling van transport), gecombineerd tot één vochtdiffusiecoëfficiënt welke afhankelijk is van het vochtgehalte zelf.

In principe kan de vochtdiffusiecoëfficiënt rechtstreeks bepaald worden uit gemeten tijdsafhankelijke vochtprofielen. Met behulp van kernspin-resonantietechnieken (NMR), waarbij het signaal evenredig is met de hoeveelheid waterstofkernen in een bepaald geselecteerd gebied van het materiaal, kunnen de vochtprofielen niet-destructief gemeten worden. Poreuze bouwmaterialen bezitten veel paramagnetische ionen. Hierdoor hebben de waterstofkernen in deze materialen zeer korte relaxatie tijden en een grote resonantielijnbreedte. Daarom is speciale kernspinresonantie apparatuur ontwikkeld waarmee het vochtgehalte in deze materialen kan worden bepaald met een ééndimensionale resolutie van 1 mm en een absolute nauwkeurigheid van enkele procenten.

Met behulp van deze kernspinresonantie apparatuur zijn vochtprofielen gemeten tijdens waterabsorptie en tijdens drogen. Bij beide processen is, binnen de meetnauwkeurigheid, een éénduidige relatie gevonden tussen de vochtdiffusiecoëfficiënt en het vochtgehalte welke afhankelijk is van het type materiaal.

Voor de in dit proefschrift bestudeerde poreuze materialen, behalve voor gips, kan de vochtdiffusiecoëfficiënt voor waterabsorptie benaderd worden met een enkelvoudige exponentiële functie van het vochtgehalte.

Aangetoond is dat het aantal roosterpunten waarop gemeten wordt en de ééndimensionale resolutie van de kernspinresonantie apparatuur de bepaling van de vochtdiffussiecoëfficiënt voor drogen nauwelijks beïnvloeden. De fout in de berekening van de vochtdiffusiecoëfficiënt wordt volledig bepaald door de meetruis en de inhomogeniteiten in de porositeit van het materiaal. In de droogexperimenten is geconstateerd dat zich na enige tijd een terugtrekkend droogfront ontwikkelt, dat zich met een constante snelheid door het materiaal beweegt. In deze fase van het droogproces wordt het vochttransport bepaald door het damptransport, dat de totale droogsnelheid begrenst. Er is een methode ontwikkeld, de zogenaamde "receding front method", om op basis van de constante snelheid van het intrekkende droogfront het isotherme vochttransport bij lage vochtgehalte te modelleren.

In metselwerk zijn baksteen en mortel aan elkaar gehecht en deze zullen dan ook een wisselwerking hebben. Daarom is er aandacht besteed aan het vochttransport over het grensvlak baksteen/mortel. Tijdens het uithardingsproces blijken de hygrische eigenschappen van mortel sterk te veranderen ten opzichte van mortel, welke individueel is uitgehard. De voorlopige absorptie experimenten laten zien dat er geen ideaal hydraulisch contact is tussen de materialen, en geven een aanwijzing dat er een sprong optreedt in de vochtpotentiaal over het grensvlak. Door de beperkte hoeveelheid experimenten kan echter nog geen afdoende verklaring worden gegeven voor de transportverschijnselen die bij het grensvlak baksteen en mortel zijn waargenomen.

APPENDIX A.1 MATERIAL PROPERTIES

In the present study the moisture transport was studied in various kinds of inorganic porous building materials, i.e.;

- 5 types of soft mud machine moulded fired-clay brick;

    VE   : red coloured brick, manufactured by de Vijf Eiken (Gilze Rijen).

    RH / RZ   : red coloured brick, manufactured by Boral Nedusa (Lobith).

    GZ / GH   : yellow coloured brick, manufactured by Boral Nedusa (Erlecom).

- 1 type of sand-lime brick (also called calcium silicate brick), manufacturer unknown.

- mortar (1 : 4.5) in two variations: with, MM, and without air-entraining agent, MZ. More details on the composition of the mortars and the preparation can be found in appendix A.2.

- 1 type of gypsum plaster: MP75SL, manufactured by Knauff.

In the tables and figures the following properties will be given of these building materials:

- mass density, ρ.

- the porosity as determined from vacuum saturation, n.

- capillary moisture content, θ_{cap}.

- relaxation times T_1, T_2 of the hydrogen nuclei in NMR experiments.

- magnetic susceptibility, χ.

- Fe content of the material as determined chemically.

- coefficients, D_0 and β, of the exponential function describing the moisture diffusivity for absorption.

- water absorption coefficient, A.

- water penetration coefficient, B.

- receding drying front velocity for a sample of 25 mm.

- moisture diffusivity for drying.

- hygroscopic curves and capillary pressure curves.

- pore size distribution as determined by mercury porosimetry.

type of material	mass density ρ (kg m⁻³) moisture contents n , θ_cap (m³ m⁻³)			relaxation times T_1 (ms), T_2 (μs) magnetic susceptibility χ (10^{-6} emu Gs⁻¹ gram⁻¹) Fe content (% M/M)			
	ρ	n	θ_{cap}	T_1	T_2	Fe	χ
brick RH	1730	0.31	0.19	230	210	3.5	2.71
RZ	1630	0.36	0.265	190	300		2.50
GH	1660	0.37	0.21	250	360	3.3	4.16
GZ	1550	0.36	0.27	120	240		3.61
VE	1570	0.41	0.28	300	180	4.0	3.43
sand-lime brick	1617	0.34	0.27	45	850	-	0.53
mortar MZ	1900	0.23	0.18	35	1000	-	0.13
MM	1800	0.23	0.15	30	950	-	0.18
gypsum	1050	0.42	0.28	50	4100	<0.1	- 0.26

Table A.1 In this tables the following properties are given

- *mass density, ρ.*
- *the porosity as determined from vacuum saturation, n.*
- *capillary moisture content, θ_{cap}.*
- *relaxation times T_1, T_2 of the hydrogen nuclei in NMR experiments.*
- *magnetic susceptibility, χ.*
- *Fe content of the material as determined chemically.*

type of material	water absorption moisture diffusivity $D_0 = D_0 \exp(\beta\theta)$ (m^2s^{-1}) absorption/penetration coef. A (kg m^{-2} $s^{-1/2}$), B (m $s^{-1/2}$)				drying front velocity for sample of 25 mm (10^{-5} mm s^{-1})
	D_0	β	A	B	
brick RH	3.25×10^{-9}	40.0	0.25	1.51	7.0
RZ	3.15×10^{-9}	30.0	0.43	1.70	6.0
GH	2.55×10^{-9}	37.0	0.26	1.42	5.1
GZ	3.50×10^{-9}	27.0	0.37	1.37	7.1
VE	2.35×10^{-9}	31.0	0.55	2.00	5.3
sand-lime brick[1]	7.90×10^{-11}	31.0	-	0.32	3.1
mortar MZ	2.35×10^{-10}	40.0	-	1.09	-
MM	2.15×10^{-9}	46.0	-	0.92	-
gypsum[1]	1.90×10^{-12}	49.0	-	0.58	7.3

[1] determined from one sample

Table A.1 (second part)

- *coefficients, D_0 and β, of the exponential function describing the moisture diffusivity for absorption.*
- *water absorption coefficient, A.*
- *water penetration coefficient, B.*
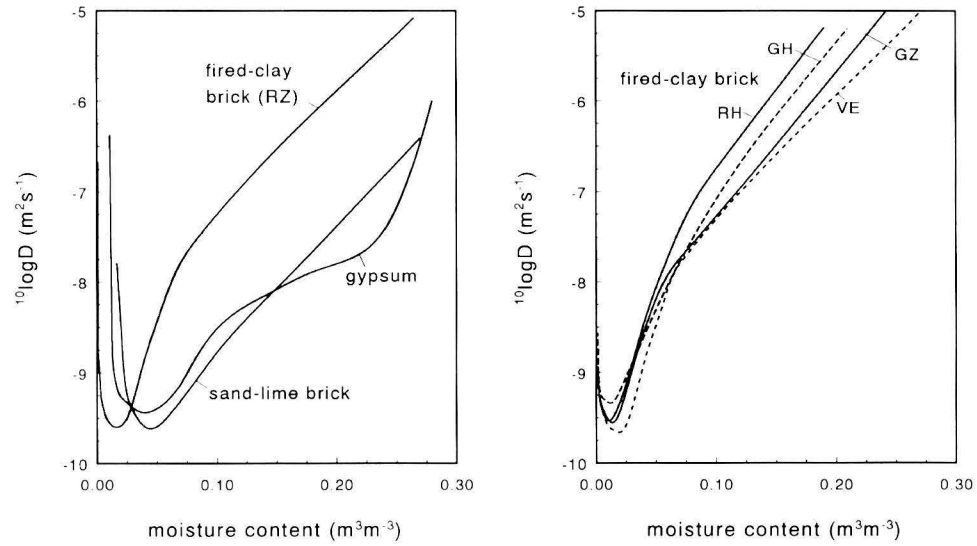- *receding drying front velocity for a sample of 25 mm.*

Figure A.1 Moisture diffusivity for drying over the full moisture content range obtained by combining the moisture diffusivities determined from, successively, moisture concentration profiles during absorption (section 4.2), during drying (section 4.3.1), and the receding drying front method (section 4.3.3). (For mortar no moisture diffusivity could be obtained. An approximation of the moisture diffusivity for mortar MZ is given in appendix A.3).
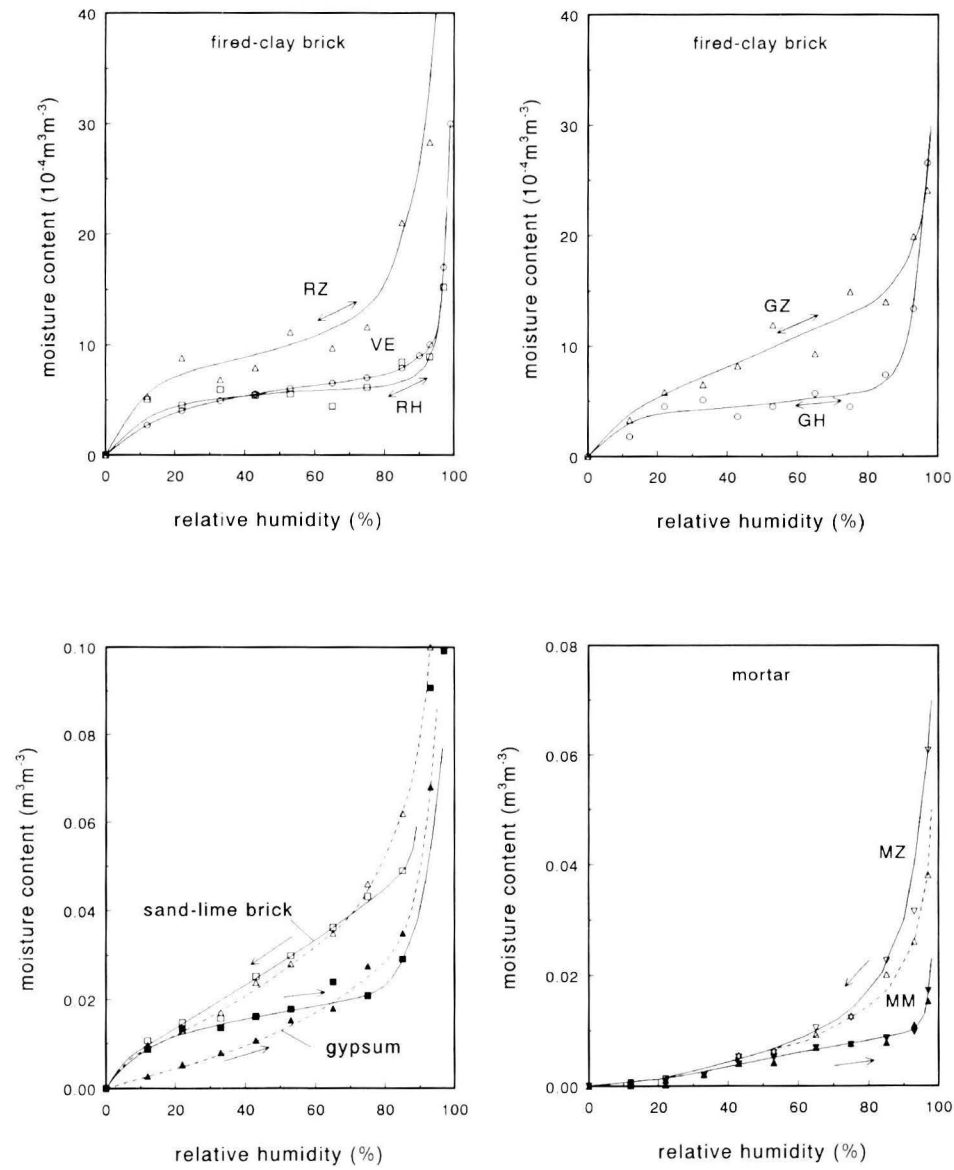
Figure A.2 The hygroscopic curves of the various building materials.
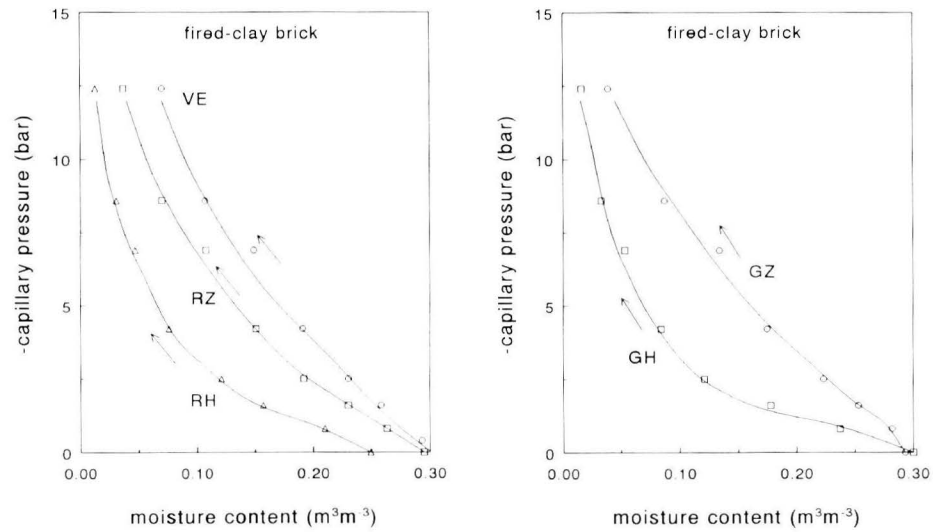
107

Figure A.3 The capillary pressure curves of the various types of fired-clay brick. Only the drying curve for one capillary saturated sample was measured. (For mortar, gypsum, and sand-lime brick no capillary curve was obtained).
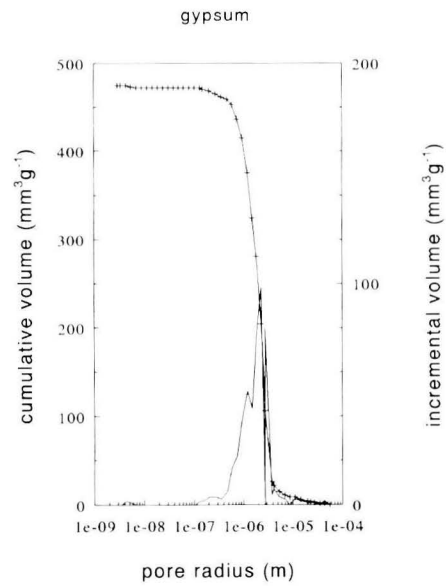

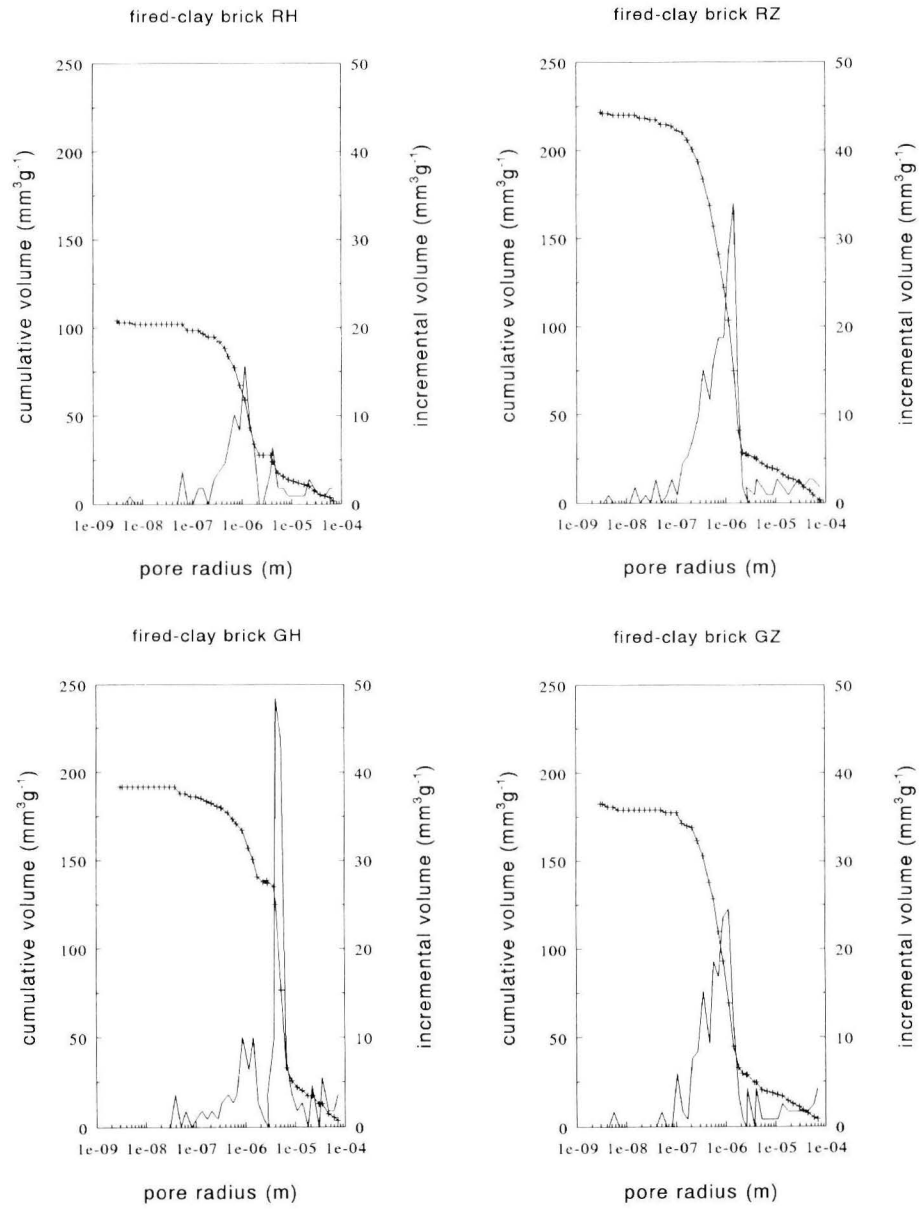*Figure A.4a The pore size distribution of the gypsum plaster.*

Figure A.4b The pore size distribution of the various types of fired-clay brick.
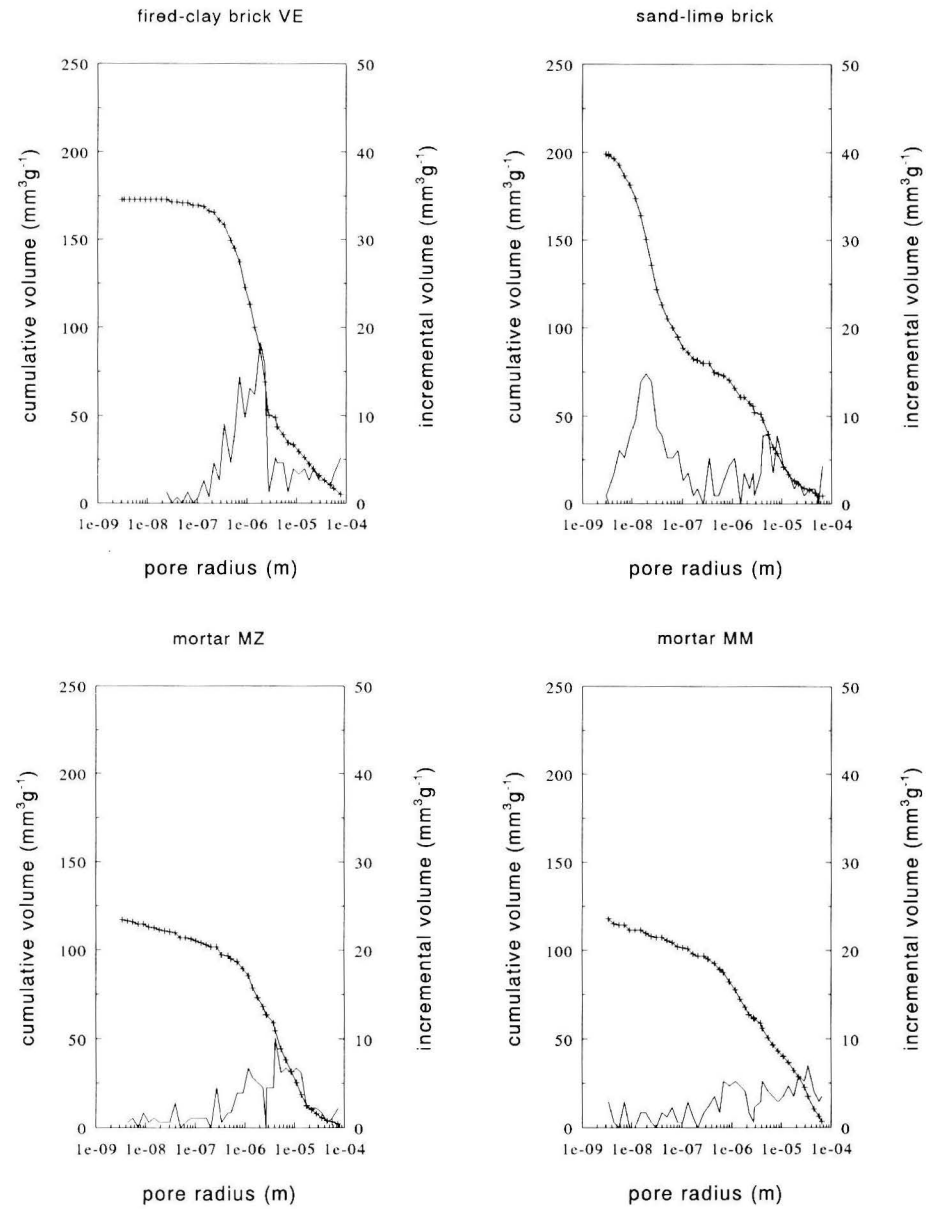
Figure A.4c The pore size distribution of various kinds of porous building material.

110

APPENDIX A.2 MORTAR SAMPLE PREPARATION

This appendix describes the preparation of the mortar samples used in the present study. In order to get reproducible mortar, the sand used for the preparation of these mortars was made out of fractions. These were sifted according to NEN 2560 and NEN 5916 out of ordinary masonry sand (metselzand 0-3 mm, de Boo, Eindhoven). The grading characteristic of the sand used, is given in table A2.1, and falls within the limits given by NEN 3835.

grain size	fraction (mass %)
1-2 mm	10
0.5-1 mm	30
250-500 µm	30
125-500 µm	30
<125 µm	-
total	100

Table A2.1 The grading characteristic of the sand used for the mortar.

Portland cement A (ENCI, Dutch Cement Industry) was used as a binding agent. It was chosen to use a cement : sand ratio of $1 : 4.5$ (V/V) = $1 : 5.6$ (M/M). The mass density of the sand and mortar were measured conform NEN 5927: $\rho_{sand} = 1500$ kg m^{-3} and $\rho_{cement} = 1200$ kg m^{-3}.

Two variations of mortar were used: with (MM) and without air-entraining agent (MZ). This agent is added to make the mortar easier workable. Use was made of Tillman mortar stabilizer T.M. (art Nr 1401, Tillman B.V.). The water content of each mortar was determined using NEN 3534, DIN 1060 and DIN 1164. These tests aim to add so much water to the mortar that it is workable under practical conditions.

The mortars were made according to a standard procedure, i.e., DIN 1164 (using a Hobart mixer type N-50). The air content of each mortar was then determined according to ASTM C 185. In table A2.2 the composition and air-content of the mortars are given.

The samples were made by pouring the mortar in teflon holders. After a week the samples were taken out of these holders. The samples were then allowed to harden for a total of 28 days at 293 K and 60 % RH.

mortar type	dry sand (mass %)	cement (mass %)	water (mass %)	1% solution of air-entraining agent (mass %)	air content of mortar (volume %)
MZ	70.5	12.5	17	-	2
MM	72	13	13.5	1	15

Table A2.2 Composition and air content of the two types of mortar.

APPENDIX A.3   NUMERICAL DETERMINATION OF THE MOISTURE DIFFUSIVITY FROM MOISTURE PROFILES

In this appendix the various steps in the numerical determination of the moisture diffusivity from measured moisture profiles during water absorption and drying will be given in more detail.

A.3.1 WATER ABSORPTION

1- Determination of the moisture profiles during water absorption with NMR. During these measurements a time stamp is added to each data point.

2- Boltzmann transformation $\lambda = x\, t^{-\frac{1}{2}}$ of each data point. Because of the presence of the electrical sensor and the water reservoir the data for $x < 10$ mm can not be used. These transformed profiles are given in figure 4.3.

3- From these transformed experimental moisture profiles, $\lambda = f(\theta)$, the moisture diffusivity can be determined by equation 4.6:

$$D_\theta = -\frac{1}{2}\frac{1}{\left(\dfrac{d\theta}{d\lambda}\right)_\theta}\int_{\theta_0}^{\theta}\lambda\,d\theta'$$

4- Starting at the intersection of the data with the horizontal λ-axis (λ_o, θ_o), the data are integrated numerically down to the moisture content of interest θ.

5- To determine $(d\theta/d\lambda)$ at the moisture content of interest, a spline approximation of the data is performed. Since the transformed data contain a very steep front, it is difficult to fit a spline directly to these data. Therefore the moisture content was squared, giving a more smoothly varying function. To the resulting data (λ, θ^2) a cubic-spline was fitted with 4 to 5 knots, minimizing the squares sum of relative deviations. The resulting spline is used to calculate $(d\theta/d\lambda)$ at the moisture content of interest.

6- The integral obtained at step 4 is divided by the local derivative obtained at step 5 to give the moisture diffusivity at the moisture content of interest. This procedure ($4 \rightarrow 6$) is repeated over the full moisture content range to give the moisture diffusivity D_0 as a function of the moisture content θ. The resulting moisture diffusivities are given in

figure 4.4.

A.3.2 DRYING

1- Determination of the moisture profiles during drying with NMR. During these measurements a time stamp is added to each data point.

2- A least-squares fit using cubic spline is performed to the data representing the moisture content as a function of time for each position of the grid for scanning. For each fit a number of knots equal to one quarter of total measuring time in hours is used (e.g., for 40 hours 10 knots). The moisture profile at a specific time, i.e., each hour (in the case of sand-lime brick each 2 hours), is calculated by interpolation using these cubic splines. The resulting moisture profiles are given in figure 4.7.

3- The moisture diffusivity can be calculated from these interpolated moisture profiles by equation 4.10:

$$D_\theta = \frac{\int_l^{x'} \left(\frac{\partial \theta}{\partial t}\right) dx}{\left(\frac{\partial \theta}{\partial x}\right)_{x'}}$$

In this equation use is made of the fact that the partial derivative of θ with respect to x is zero at the vapour tight bottom (x = l).

4- For the calculation of ($\partial \theta/\partial t$) at each position the splines obtained at step 2 are used. These derivatives are numerically integrated down to the position of interest, x'.

5- To calculate ($\partial \theta/\partial x$) at the position of interest a least-squares cubic spline approximation of each moisture profiles is made. For each profile, typically consisting of 165 data points, 25 to 30 knots are used. ($\partial \theta/\partial x$) is numerically calculated from these cubic splines.

6- Using the integral obtained at step 4 and the derivative obtained at step 5 the moisture diffusivity is calculated for the position of interest, corresponding to a moisture content θ. This procedure (4→6) is repeated for all profiles to give the moisture diffusivity as a

function of the moisture content. The resulting moisture diffusivities are given in figure 4.10. Only those regions of the moisture profiles are used, where the effects of inhomogeneities are relatively small and the situation can be regarded as isothermal. (For instance, negative values of the moisture diffusivity, which are merely a result of the inhomogeneities, are not taken into account).

APPENDIX A.4 PROGRAM MOVIES

With this thesis comes a disk (3.5", 1.44 Mb) containing the program MOVIES. Using this program you can see short movies showing the experimental results and simulations given in chapter 4 and 5. This program will run on any IBM compatible PC with VGA, from 286 upwards.

Installation options:

a)- you can run the program directly from disk (execution of the program is rather slow).

b)- copy the contents of the disk to any directory on your hard disk.

c)- go to the disk A:\ and type INSTALL.

   The program will be installed on your hard disk in the directory C:\PHDPEL

Getting started

- step 1 : type MOVIES

- step 2 : You will now see an introduction screen.

   press ENTER or click on OK with the mouse.

- step 3 : Now you will see a file index of the available movies. Choose the movie you want to see by either:

   - using the cursor keys and then pressing ENTER.

   - clicking on the movie with the mouse.

   - by pressing TAB, typing in the name of the movie, and pressing ENTER.

   More information on the various movies can be found under: File Information.

- step 4 : Now you will see measured or simulated moisture profiles as a function of the time. While the movie is playing, the following options are available:

   E = end the movie and go back to the file index menu

   S = stop the movie

   F = go forward one time-step

   B = go backward one time-step

   C = continue

- step 5 : You can end the program by clicking on EXIT with the mouse or by typing ALT-E.

The following movies (*.MOV) are available:

- Computer simulations of the moisture profiles during absorption:

  ABSBRIVE   : ABSorption fired-clay BRIck VE

  ABSBRIRZ   : ABSorption fired-clay BRIck RZ

  ABSMORMZ   : ABSorption MORtar MZ

  ABSGYPSU   : ABSorption GYPSUm

  ABSSANLI   : ABSorption SANd-LIme brick

- Moisture profiles as measured during drying:

  DRYBRIRZ   : DRYing fired-clay BRIck RZ

  DRYSANLI   : DRYing SANnd-LIme brick

  DRYGYPSU   : DRYing GYPSUm

  DRYMORMZ   : DRYing MORtar MZ

- Moisture profiles during drying as simulated for a sample of 25mm for various
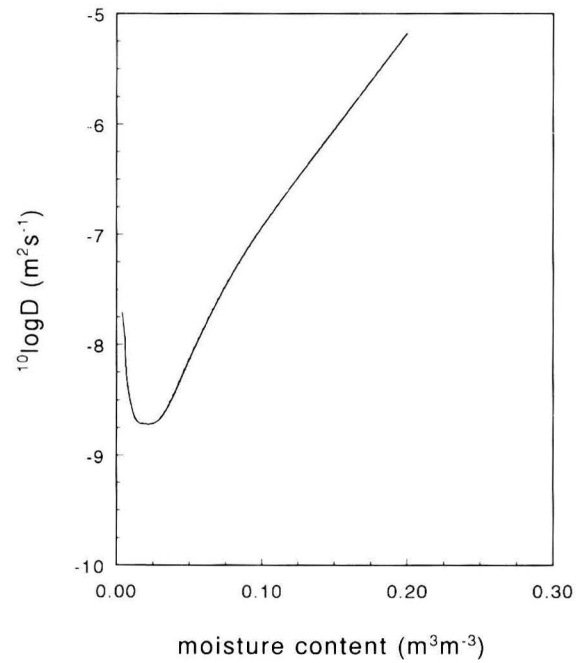 values of the moisture diffusivity at 45% RH:

  SIMRZ650   : SIMulation fired-clay brick RZ logD(45% RH)= -6.50

  SIMRZ700   : SIMulation fired-clay brick RZ logD(45% RH)= -7.00

  SIMRZ750   : SIMulation fired-clay brick RZ logD(45% RH)= -7.50

  SIMSL675   : SIMulation Sand-Lime brick logD(45% RH)= -6.75

  SIMSL725   : SIMulation Sand-Lime brick logD(45% RH)= -7.25

  SIMSL775   : SIMulation Sand-Lime brick logD(45% RH)= -7.75

- Moisture profiles as measured during water absorption from brick to mortar or
 from mortar to brick:

  CABSGHMZ   : ABSorption sample fired-clay brick GH / mortar MZ

  CABSMZGH   : ABSorption sample mortar MZ / fired-clay brick GH

  CABSGZMM   : ABSorption sample fired-clay brick GZ / mortar MM

  CABSMMGZ   : ABSorption sample mortar MM / fired-clay brick GZ

  CABSRHMZ   : ABSorption sample fired-clay brick RH / mortar MZ

APPENDIX A.5 MORTAR DIFFUSIVITY

For mortar without air-entraining agent (MZ) a moisture diffusivity, which approximately models the measured drying behaviour given in figure 4.7d, was constructed by trial and error. This moisture diffusivity is plotted in figure A5.1. A computer simulation of the moisture profiles using this moisture diffusivity is plotted in figure A5.2.

Figure A5.1 The moisture diffusivity for drying constructed for mortar (MZ), which approximately models the measured drying behaviour (see Fig. 4.7d).
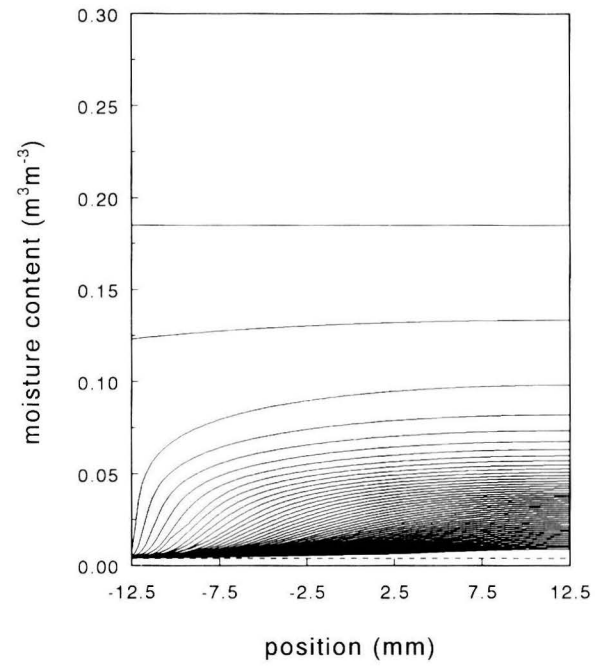
Figure A5.2 A computer simulation of the drying of mortar (MZ) using the moisture diffusivity plotted in figure A5.1. The time between subsequent profiles is 1 hour and the profiles are given for a period 48 hours.

APPENDIX A.6 BRICK/MORTAR WATER ABSORPTION SIMULATION

In this appendix computer simulations of the absorption by an idealized brick/mortar sample will be presented. These simulations are only meant as an illustration of the phenomena observed in the experiments described in chapter 5. Computer simulations were performed of the moisture profiles during water absorption by a sample of 105 mm fired-clay brick (GH) and 45 mm mortar (MZ). It is assumed that the mortar is homogeneous. Since it was found in the experiments that the mortar absorption decreases with almost a factor 3 towards the brick/mortar interface a diffusion coefficient was constructed accordingly. The coefficients of the exponential function describing the moisture diffusivity for absorption and the capillary moisture content at the boundary used in the simulations are given in table A6.1.

	D_0 (m^2s^{-1})	β (-)	θ_{cap} (m^3m^{-3})
brick (GH)	2.58×10^{-9}	37.2	0.208
mortar (MZ)	5.62×10^{-10}	32.2	0.170

Table A6.1 The coefficients of the exponential function, $D_\theta = D_0 exp(\beta\theta)$, describing the moisture diffusivity for absorption and the capillary moisture content, θ_{cap}, at the boundary, x=0, used in the computer simulations.

In the simulations a linear relationship is assumed between the moisture content of the fired-clay brick and the mortar at the brick/mortar boundary. To simulate a jump in the suction, it is assumed in addition that in the brick (in case of absorption from mortar to brick) or in the mortar (in case of absorption from brick to mortar) water absorption will only occur up to 70% of their respective capillary moisture contents near the interface. The results of these simulations are given in figure A6.1.
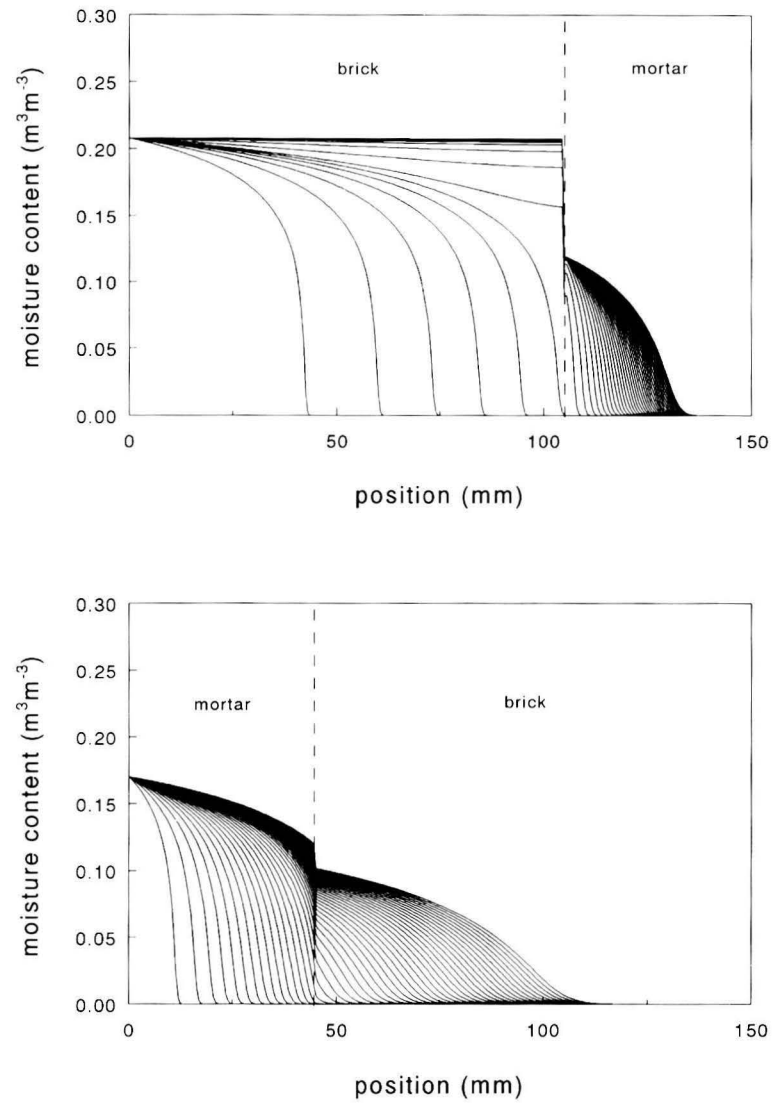
Figure A6.1 Computer simulations of moisture profiles during water absorption in a sample of fired-clay brick (GH) and mortar (MZ). The time between subsequent profiles is 900 s for absorption from brick to mortar and 1800 s for absorption from mortar to brick. The profiles are given for a period of 6 hours and 12 hours, respectively.

PUBLICATIONS

L. Pel, A.A.J. Ketelaars, O.C.G. Adan and A.A. van Well, Determination of moisture diffusivity in porous media using scanning neutron radiography, *Int. J. Heat Mass Transfer* **36**, 1261-1267 (1993).

K. Kopinga and L. Pel, One dimensional scanning of moisture in porous materials with NMR, *accepted for publication in Rev. Sci. Instr. Dec. (1994).*

A.A.J. Ketelaars, L. Pel, W.J. Coumans and P.J.A.M. Kerkhof, Drying kinetics; a comparison of diffusion coefficients from moisture concentration profiles and drying curves, *accepted for publication Chem. Eng. Sci. (1995).*

L. Pel, K. Kopinga, G. Bertram and G. Lang, Water absorption in fired-clay brick observed by NMR scanning, *accepted for publication in J. Phys. D: Appl. Phys. (1995).*

L. Pel, H. Brocken and K. Kopinga, Determination of moisture diffusivity in porous media using moisture concentration profiles, *to be published in Int. J. Heat Mass Transfer.*

E.J. La Heij, K. Kopinga, L. Pel and P.J.A.M Kerkhof, Determination of porosity profiles during filtration and expression of sewage sludge by use of NMR imaging, *to be published in AIChE Journal.*

L. Pel, Dynamic moisture transport in porous materials, *Int. workshop Durability of Masonry (edited by L. Binda and P.C.F Bekker), Milan, Italy,* 41-53 (1992).

L. Pel, Moisture transport through masonry, *Proc. 10th Int. Brick/Block Masonry Conf. Calgary, Canada,* 803- 810 (1994).

L. Pel, A.A.J. Ketelaars, O.C.G. Adan en A.A. van Well, Bepaling van de vochtvereffings-coefficient in poreuze media door middel van scanning neutronen radiografie, *Bouwfysica* **4**, 11-17 (1993).

H. Smulders, L. Pel, P. van de Ende en A.W.B. Theuws, Het meten van het vochttransport door baksteen en mortel met neutronenradiografie, *Materialen* **5**, 41-44 (1994).

H.J. Brocken, L. Pel en O.C.G Adan, Vereenvoudigde modellen voor het vochttransport versus metingen, *Bouwfysica* **5**, 18-25 (1994).

DANKWOORD

Het in dit proefschrift beschreven onderzoek is mede tot stand gekomen dankzij de bijdrage van verschillende mensen. Hiervan wil ik enkele met name bedanken:

- Professor Bekker voor krachtig stimuleren van de start van dit onderzoek, het zorgen voor de noodzakelijke financiële ondersteuning en zijn kritische maar tevens enthousiaste begeleiding.

- Jaap Wisse en Martin de Wit voor het in mij gestelde vertrouwen en de grote mate van vrijheid en verantwoordelijkheid die ik heb gekregen tijdens dit onderzoek.

- Klaas Kopinga voor zijn enthousiaste begeleiding die hij mij, in het verlengde van mijn studie, weer 3 jaar heeft willen geven en het kritisch doorlezen van het proefschrift. In samenwerking met hem zijn de artikelen ontstaan waarop dit proefschrift is gebaseerd.

- De technici Harrie Smulders, Guus Theuws en Jef Noijen zonder wie de in dit proefschrift beschreven experimenten en opstellingen niet zouden zijn gerealiseerd.

- De studenten Gillian Lang, Harold Brocken, Gabi Bertram en Helen Wielders die ieder een belangrijke bijdrage hebben geleverd aan dit onderzoek.

- De bouwers (hard en software) van de NMR opstelling: Henry Otten, Berrie Sanders, Alexander de Boer, Ronald van Splunter en de medewerkers van de Bedrijfsgroep Laboratoriumautomatisering.

- Mijn mede-promovendi Olaf Adan en Jos Vijgen, met wie ik menige discussie heb gevoerd over onderzoek, maar ook over de organisatie daar omheen.

- Ad van Well en Piet van de Ende van het Interfaculteit Reactor Instituut te Delft voor hun enthousiaste ondersteuning van het onderzoek

- De kerncommissie leden Piet Kerkhof en Thijs Michels voor hun waardevolle discussies bij het tot stand komen van dit proefschrift

Verder wil ik nog bedanken (in willekeurige volgorde):
Toine Ketelaars met wie ik samen de eerste aanzetten heb gegeven tot de ontwikkelingen van

niet destructieve meetmethoden. Wim de Jonge voor de gastvrijheid en ondersteuning die hij heeft willen bieden. David Smeulders met wie ik samen het boek van Bear heb doorgenomen. De medewerkers van BKO en de maquette-werkplaats voor al hun hulp. Casper Groot voor de discussie over het vochttransport bij de overgang baksteen/mortel en het geven van de aanzet tot neutronen-radiografie. Loek van der Klugt voor het aandragen van vele jaren van praktijk-kennis (die iemand nooit kan bereiken in vier jaar). Erik La Heij met wie ik nog een toepassingsgebied van de NMR heb ontdekt. Professor de Vries voor de belangstelling die hij deze vier jaar heeft getoond voor het onderzoek. De studenten die het FAGO-hok in de middagpauze tot een gezellige boel maakten. Ben Elfrink voor het maken de foto's van de NMR- en de neutronen opstelling.

Een multidisciplinair onderzoek als dit is gebaat bij discussies en de uitwisseling van ideeën. In deze vier jaar heb ik gesproken met de medewerkers van vele faculteiten. Ik wil hun allen bedanken voor de bijdrage die zij, gevraagd en ongevraagd, hebben geleverd aan dit onderzoek.

Tot slot wil ik mijn ouders, broer en "schoonzus" bedanken voor de noodzakelijke morele ondersteuning gedurende deze vier jaar.

Leo Pel, december 1994

CURRICULUM VITAE

23 September 1962 - Geboren te Epse (gemeente Gorssel)

zoon van M. Pel en A. Pel - van Berkel en broertje van Jan

1975 - 1981   - Eindhovens Protestants Lyceum

31 Juni 1981 : eindexamen Atheneum B

1981 - 1988   - Student Technische Universiteit Eindhoven

faculteit Technische Natuurkunde

Afstudeerwerk onder begeleiding van dr.ir. K. Kopinga in de groep

Magnetische Ordeningsverschijnselen van prof.dr.ir. W.J.M. de Jonge

31 Augustus 1988 : Ingenieursexamen (met lof)

titel: Ontwikkeling van een fluxgate magnetometer

1988 - 1989   - Militaire dienst

1990 - 1993   - lid commissie B51 `Duurzaamheid van Metselwerk` van het

Civieltechnisch Centrum Uitvoering Research en Regelgeving (CUR)

1990 - 1994   - Promovendus Technische Universiteit Eindhoven

vakgroep Fysische Aspecten van de Gebouwde Omgeving

Onder begeleiding van prof.dr.ir. P.C.F. Bekker, prof.dr.ir. K. Kopinga,

prof.ir. J.A. Wisse en dr.ir. M.H. de Wit

MOISTURE TRANSPORT

IN

POROUS BUILDING MATERIALS
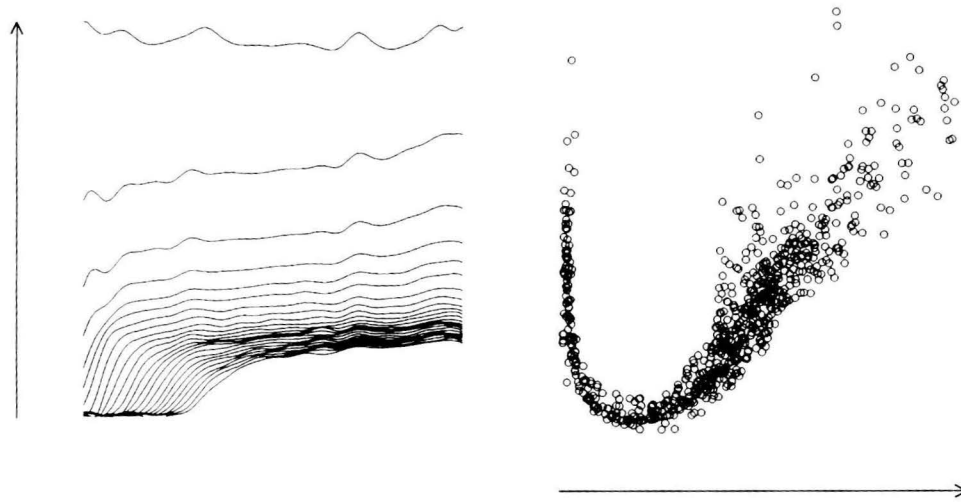
Stellingen

behorende bij het proefschrift

van

Leo Pel

1. Bij de publikatie van gemeten ééndimensionale vochtprofielen dient de resolutie van de gebruikte meetmethode vermeld te worden.

2. De constante snelheid van het intrekkend droogfront kan worden gebruikt om de vochtdiffusiecoëfficiënt van poreuze materialen bij lage vochtgehalten te modelleren.

   Dit proefschrift, hoofdstuk 4.

3. Carpenter *et al.* calibreren ten onrechte de vochtprofielen, gemeten met kernspin-resonantie bij opzuiging onder atmosferische condities, met behulp van een onder vacuüm verzadigd preparaat.

   *T.A. Carpenter, E.S. Davies, C. Hall, L.D. Hall, W.D. Hoff and M.A. Wilson, Materials and Structures **26**, 286-292 (1993).*

4. De aanname dat een gecomprimeerde filterkoek een lineair porositeitsprofiel heeft, maakt de berekening van de plaatsafhankelijkheid van de elasticiteitsmodulus eenvoudiger, maar is niet realistisch.

   *C. Buttersack, Chem. Eng. Sci. **49**, 1145-1160 (1994).*

5. De resultaten van de opzuigexperimenten van Prazak *et al.*, met name de herverdeling van het water, kunnen verklaard worden door rekening te houden met hysterese-effecten.

   *J. Pražák, J. Tywoniak, F. Peterka and T. Šlonc, Gesundheits-Ingenieur **110**, 308-312 (1989).*

6. Dat Adebayo *et al.* en Luard en Griffin geen relatie vinden tussen de turgordruk in het mycelium en de groeisnelheid van de schimmel, wordt mede veroorzaakt doordat de waterpotentiaal van de celvloeistof in het mycelium niet in evenwicht is met de water-potentiaal van het substraat.

    A.A. Adebayo, R.F. Harris and W.R. Gardner, Trans. Br. Mycol. Soc. 57, 145-151 (1971).
    E.J. Luard and D.M. Griffin, Trans. Br. Mycol. Soc. 76, 33-40 (1971).

7. Het door Platten gevonden minimum in de vochtdiffusiecoëfficiënt voor waterabsorptie wordt geïntroduceerd door de lage resolutie van de gebruikte meetmethode.

    A.K. Platten, Ph.D. thesis, University of Manchester, U.K. (1985).

8. De in artikel 19 van het promotieregelement gevraagde leesbaarheid en vermeningvul-digbaarheid van de dissertatie kan ook worden bereikt met moderne informatiedragers. Deze informatiedragers hebben als bijkomend voordeel dat computer-animaties van complexe processen kunnen worden opgenomen.

9. De overheid zal in de nabije toekomst tot regelgeving moeten overgaan om misbruik van "real-time" beeldmanipulatie te voorkomen.

10. In tegenstelling tot het gebruik ervan bij wedstrijdkano's, is de mogelijke toepassing van cement en beton in de zweefvliegerij nog opmerkelijk weinig onderzocht.